Production of a cryogenic beam and prospects for traveling-wave Stark deceleration of BaOH

Master Thesis

February 14, 2020

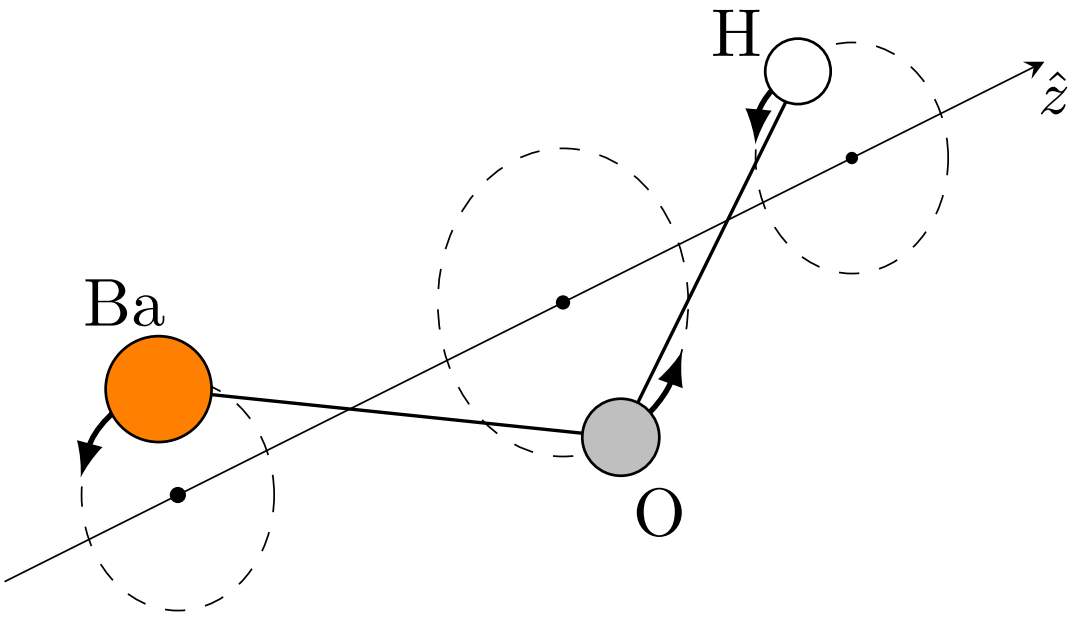

Author: Kees Steinebach

Supervisor: Prof. dr. S. Hoekstra

university of groningen / faculty of science and engineering

Abstract

The electron electric dipole moment (eEDM) is an important probe for physics beyond the standard model. Currently diatomic molecules such as BaF, YbF or ThO are used for eEDM measurements. It was recently shown that polyatomic molecules isoelectronic to laser-coolable diatomic molecules such as BaF can also be used in an eEDM measurement. These molecules are potentially laser-coolable and because of more vibrational and rotational degrees of freedom important systematic effects can be suppressed.

In this thesis it is investigated if the triatomic molecule BaOH can be decelerated in a traveling-wave Stark decelerator and if this molecule can be made in a cryogenic source. This combination can potentially bring the molecules to rest in the laboratory frame or create a slow molecular beam and increase the coherence time of these precision measurements. By first calculating the Stark effect and then performing simulations of the deceleration process it is found that efficient traveling-wave Stark deceleration in the first excited bending vibration is possible and because of the different Stark effect and rotational structure nonadiabatic transitions should be suppressed. By laser ablation of a pressed $Ba(OH)_2$ target in a cryogenic source a beam of BaOH was made and observed through absorption spectroscopy. Upon optimization of the target similar yields as for the isoelectronic diatomic molecule BaF should be possible.

Contents

Chapter 1

Introduction

Over the last decades there have been several advances in techniques to slow and cool molecules. Some of these techniques are extensions of atomic physics techniques, such as laser cooling [1], but also new techniques have been developed, such as Stark deceleration [2]. Cold molecules have many interesting applications, such as quantum computing [3] and fundamental physics.

One of the fundamental physics applications of cold and slow molecules is the search for the electron electric dipole moment (eEDM). The eEDM moment is a probe for physics beyond the standard model. The predicted value for the eEDM in the standard model is very small. Finding a larger value than predicted would mean that there are additional mechanisms that must make this possible. An eEDM of a fundamental particle violates time-reversal symmetry, which means that charge-parity (CP) symmetry is also violated for charge-parity-time-reversal symmetry (CPT) to hold. The eEDM is especially interesting because it is related to the matter-antimatter asymmetry. The matter-antimatter asymmetry is one of the outstanding problems in physics. A mechanism that allows for more CP-violation is also responsible for a larger value of the eEDM.

The NL-eEDM experiment plans to do a measurement of the eEDM with barium (mono)fluoride molecules (BaF).

1.1 Electron EDM and Molecules

It might seem strange to use molecules to measure a property of the electron. To measure the eEDM the electron needs to be placed in an electric field, since an EDM has a potential energy in an electric field given by:

$$V = \vec{E} \cdot \vec{d} \tag{1.1}$$

However, an electron is charged and would experience a force in an electric field, making such a measurement not very feasible. Furthermore, the EDM of the electron is expected to be very small, it is therefore necessary to apply a very large electric field. Neutral polar

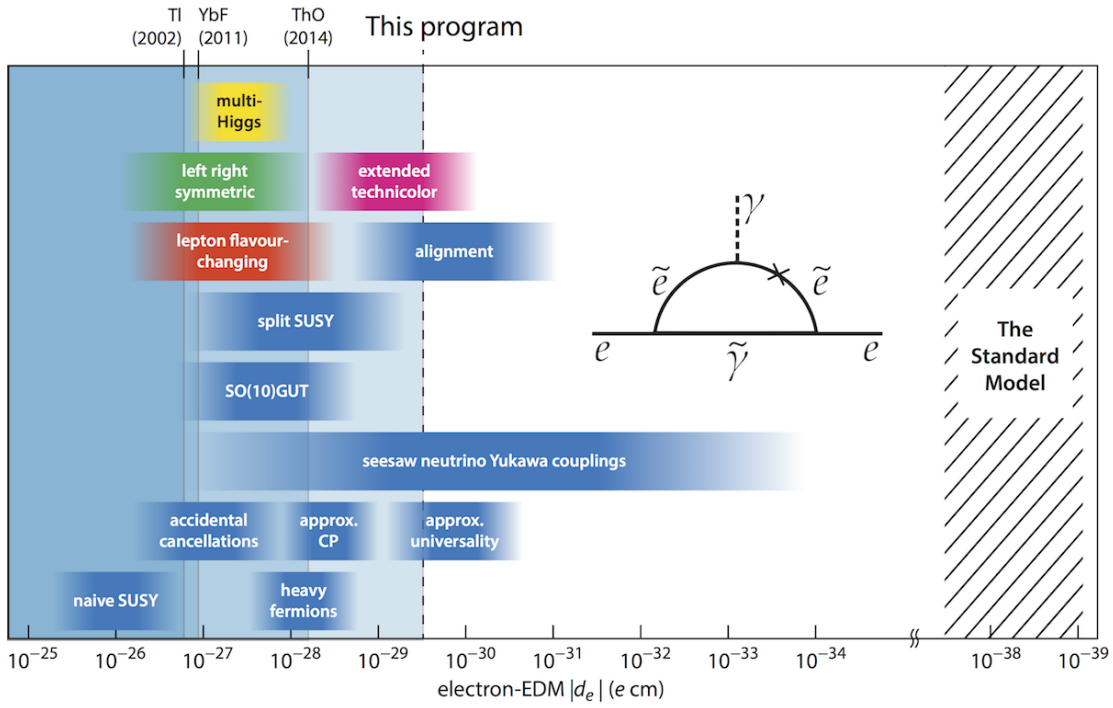

Figure 1.1: Predicted electron EDM values compared to experimental upper limits [4].

diatomic molecules offer several advantages for an eEDM measurement. Firstly, these molecules are neutral and do not experience a force in a static electric field. Secondly, the effective electric field that the electrons experience inside these polar molecules is much larger than can be created in a laboratory. Because of this effective electric field the effect of the eEDM is significantly enhanced. This effective electric field is a relativistic effect [5]. The enhancement factor Q can be written as [6]:

$$Q = E_{\text{eff}} P(E_{\text{ext}}), \tag{1.2}$$

where E_{eff} is the effective electric field which depends on the molecular structure and P is the polarization factor, which depends on the applied external field. This effective electric field cannot be measured and must be calculated. The molecule must be polarized in the laboratory frame, because the enhancement factor lies along the internuclear axis, because of the cylindrical symmetry of diatomic molecules. Since a molecule rotates the molecule has no fixed orientation and the enhancement factor will average out [6]. An electric field will mix states of opposite parity and this will orient the molecule in the laboratory frame. The degree of orientation is the polarization factor $P(E_{\text{ext}})$.

A non-zero eEDM will shift the energy levels (sensitive to the eEDM) of a molecule when an external electric field is applied. Since the electron eEDM lies along the spin of the electron and the effective electric field along the internuclear axis($\hat{n}$), a state sensitive to the eEDM must have a nonzero expectation value for $< \hat{S} \cdot \hat{n} >$. A magnetic field will shift

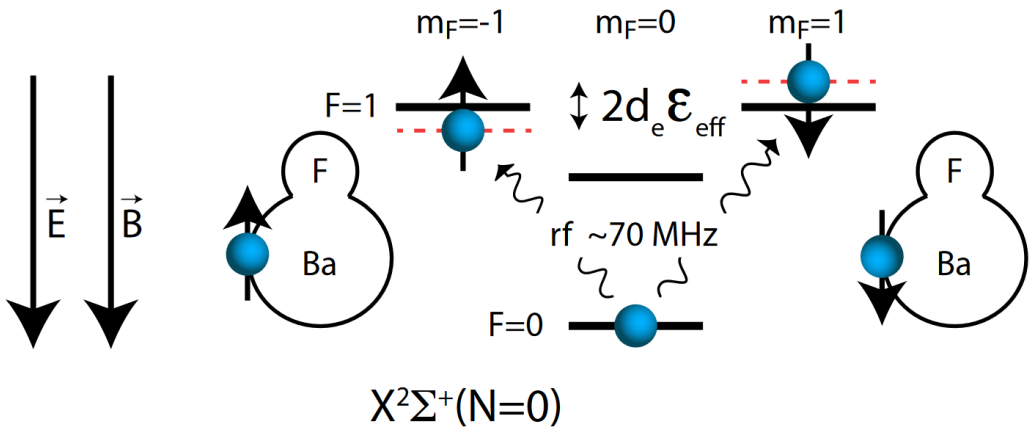

Figure 1.2: Overview of the eEDM measurement states in BaF [9].

the energy levels because of the Zeeman effect. The relative sign of this shift for the same energy level depends on the relative orientation of the magnetic and electric fields. Hence, the general approach to an eEDM measurement is to measure a difference in energy/phase between two different configurations of the electric and magnetic fields.

Most experiments use a similar Ramsey-type measurement scheme [7][8][9][10], but other approaches have also been suggested [11]. The following explanation is most valid for a ${}^2\Sigma_{\frac{1}{2}}$ molecule such as BaF or YbF, but similar for other electronic states of other molecules.

This explanation is based on [12]. The relevant energy scheme is shown in figure 1.2. Initially the molecules are prepared in the $|F, M\rangle = |0, 0\rangle$ state. A π pulse transfers the molecules into the $|\psi\rangle = |c\rangle = \frac{1}{\sqrt{2}}\big(|1, 1\rangle + |1, -1\rangle\big)$ state. We define $|u\rangle = \frac{1}{\sqrt{2}}\big(|1, 1\rangle - |1, -1\rangle\big)$. The molecules next fly through a region with parallel magnetic and electric fields and acquire a phase $\phi = (g\mu_b B + d_e E_{\text{eff}}|P|)\tau/\hbar$, because of the energy difference between the $|1, \pm 1\rangle$ states. The wavefunction now is $|\psi\rangle = \frac{1}{\sqrt{2}}\big(e^{i\phi}|1, 1\rangle + e^{-i\phi}|1, -1\rangle\big) = \cos\phi\,|c\rangle + i\sin\phi\,|u\rangle$. After the parallel magnetic and electric fields $|c\rangle$ is projected back on to the $|0, 0\rangle$ state with probability $P_r = \cos^2\phi$. Thus, from the population in the $|0, 0\rangle$ state the accumulated phase can be determined. The quantity $d_e E_{\text{eff}}|P|\tau/\hbar$ can be determined by changing the relative orientation of the electric and magnetic fields to anti-parallel. This changes the relative sign of the eEDM interaction and Zeeman shift. Thus $d_e E_{\text{eff}}|P|\tau/\hbar$ is determined by the difference in accumulated phase of the 2 configurations of the electric and magnetic fields.

The statistical uncertainty of such a measurement is given by:

$$\sigma_d = \frac{\hbar}{e}\frac{1}{2|P|E_{\text{eff}}\sqrt{\dot{N}T\tau}}, \tag{1.3}$$

where τ is the coherence time, $\dot{N}$ is the number of molecules per second and T is the measurement time. Therefore, to decrease the statistical uncertainty the coherence time must be increased or/and the total number of molecules must be increased. The NL-eEDM collaboration will use a traveling-wave Stark decelerator to slow down the molecules from a cryogenic source to increase the coherence time followed by a period of transverse laser cooling to increase the number of molecules that fly through the interaction zone.

However, decreasing the statistical uncertainty also requires that the systematic errors are reduced. An eEDM measurement is very complex, with a lot of potential systematic errors. Especially dangerous are systematic errors that also change sign or change in magnitude when reversing the magnetic and electric fields, since these cannot be differentiated from a real eEDM. For example, any change in B-field or E-field between the two configurations can cause a difference in accumulated phase $g\mu_b B$. Furthermore, any spatial inhomogeneities can lead to a geometric phase which can be dependent on the orientation of magnetic and electric fields [6]. In principle these systematic can be well controlled by a careful design of the interaction zone and control of the electric and magnetic fields [9].

The experiment that has the current best limit on the eEDM uses a beam of thorium oxide molecules [7]. This molecule has a parity doublet structure in the eEDM sensitive electronic state. This gives several benefits over BaF and YbF. Firstly, this molecule can be fully polarized in a small electric field ($|P| = 1$). Secondly, these two close lying states of opposite parity have the same, but opposite shift in an electric field. These states are both fully oriented in an electric field, but oppositely. Therefore, in these two different states the molecules have the same but opposite eEDM interaction and the electric and magnetic fields in this experiment do no need to be reversed for this molecule. This suppresses many of the above systematic errors. Unfortunately this molecule cannot be laser cooled and has a short lifetime in the eEDM sensitive state, making it difficult to increase the statistical uncertainty.

1.2 Polyatomic Molecules

The 'ultimate' future eEDM experiment would use a large number of optically trapped molecules. To do this the molecule needs to be cooled substantially, which can be done by laser cooling. An eEDM measurement with these optically trapped molecules will significantly increase the statistical uncertainty. This also requires that the systematic errors are reduced, which can be done with internal co-magnetometer states. Unfortunately, there are no diatomic molecules with the combination of laser cooling and internal co-magnetometer states[13]. However, it was pointed out by Kozyryev and Hutzler [13] that polyatomic molecules isoelectronic to laser-coolable diatomic molecules with sensitivity for the eEDM could also be used in an eEDM experiment. Effectively the fluoride atom in molecules such as BaF or YbF is replaced by a more complicated functional group such as OH or OCH_3. These polyatomic molecules have the same electronic structure as their diatomic

counterparts and are thus potentially laser-coolable, but since these polyatomic molecules consist of more nuclei, they have more vibrational degrees of freedom (and symmetric top molecules also have more rotational degrees of freedom). This leads to parity doublet states (or co-magnetometer states) independent of electronic structure that do not interfere with laser cooling properties. Thus, these molecules combine laser cooling and co-magnetometer states.

In recent years there has been a lot of progress in laser cooling of polyatomic molecules. Two triatomic molecules SrOH and YbOH have already been laser cooled in 1D by means of magnetically assisted Sisyphus cooling [14][15] and CaOH has been trapped in a 1D magneto-optical trap [16]. Recently, also a number of asymmetric top molecules have been proposed for laser cooling [17]. Laser-coolable molecules with linear Stark shifts have also other applications such as quantum computing [18]. These types of molecules have also been investigated in context with ultra cold collisions [19].

In this thesis the use of barium monohydroxide (BaOH) for an eEDM experiment is investigated. BaOH is isoelectronic to BaF, the molecule for which currently an eEDM measurement is underway. These molecules have approximately the same mass and because the molecule has the same electronic structure the wavelengths of the transitions are very similar. Calculations have shown that the internal electric fields of BaOH and YbOH are the same as for their diatomic counterparts [20] [21]. Since BaOH has advantages over BaF related to systematic errors it will be interesting to see if BaOH can be used with the current experimental setup, for perhaps a future experiment. We will in particular focus on the production of BaOH in a cryogenic source and on the traveling-wave Stark deceleration. Such a combination could bring the molecules to rest in the laboratory frame for a next cooling step such as loading into a MOT or it allows to create a slow molecular beam. Furthermore, some properties of the Stark effect related to the eEDM measurement will be investigated. Lastly, in appendix A we give an estimate of the Franck-Condon factors for this molecule, to show that this molecule indeed has promise for laser cooling.

Chapter 2

Background

2.1 Theory

2.1.1 Molecular Structure

Compared to atoms, which only have electronic states, diatomic molecules are far more complicated with many electronic, vibrational and rotational states. Polyatomic molecules such as BaOH are even more complicated. In this section the main difference between a triatomic molecule such as BaOH and a diatomic molecule such as BaF will be explained [22].

The electronic structure of a linear polyatomic molecule such as BaOH is exactly analogous to the structure of a diatomic molecule such as BaF. The electronic structure contributes the most to the energy of the molecule. Since a linear polyatomic molecule also has cylindrical symmetry the projection of electron angular momentum on the symmetry axis is conserved and the electronic states are labeled in the same way as diatomic molecules: ${}^{2S+1}\Lambda_{\Omega}$, where Λ is the sum of the angular momenta of the unpaired electrons of the molecule. S is the total spin and Ω is the projection of the total electron angular momentum on the internuclear axis. In diatomic molecules the ground state is given the letter X and the next excited states A, B, C etc. This is also done for polyatomic molecules but a tilde is added to the letter: $\tilde{X}$, $\tilde{A}$, $\tilde{B}$, $\tilde{C}$ to indicate a difference from diatomic molecules. The only exception is an excited bending vibration in an electronic state with $\Lambda \neq 0$, which will be discussed below.

The nuclei in a molecule can move with respect to each other in a potential which is dependent on the distance between the nuclei: the vibrational motion. The main different between a diatomic molecule and a linear polyatomic molecule is that there are multiple vibrational modes. Clearly a diatomic molecule only has one vibrational mode, but in a linear polyatomic molecule the nuclei can move in different ways with respect to each other. To see how many vibrational modes a molecule has it is necessary to look at the degrees of freedom of the molecule [23]. To describe a molecule consisting of N atoms, we need 3N coordinates (3 coordinates to describe the position of every atom). This describes

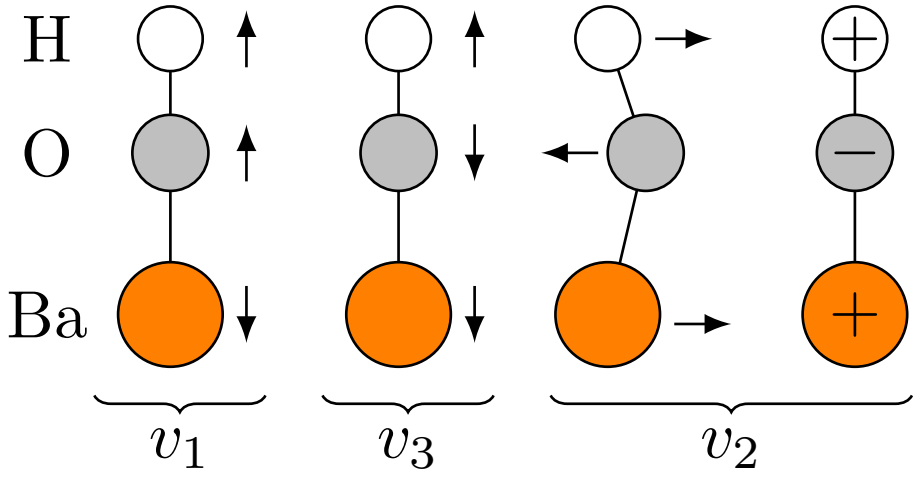

Figure 2.1: Vibrational normal modes of a triatomic ABC molecule such as BaOH. v_1 is the metal-oxygen stretching mode, v_2 is the degenerate bending vibration and v_3 is the oxygen-hydrogen stretching.

the translation, rotation and vibration of the molecule. Three coordinates are necessary to describe the translation of the molecule. The rotation of a linear molecule in space can be described by 2 angles. Since a rotation about its axis will leave the molecule invariant it cannot be described by this rotation. However, nonlinear polyatomic can be described by 3 angles. Therefore, linear polyatomic molecules have 3N - 5 vibrational modes and nonlinear polyatomic molecules have 3N - 6 vibrational modes.

A linear triatomic molecule has 4 modes of vibration. The potential between the nuclei is in good approximation harmonic. The vibrations are described by the normal modes of vibration. This is the motion in which all nuclei move with constant phase and frequency. With each normal mode a normal coordinate Q_k is associated which is completely independent. The normal modes of vibration can be described in first approximation by 3N - 5 one-dimensional independent quantum harmonic oscillators with a frequency w_k and energy eigenvalue [24]:

$$E_n = (n + \frac{1}{2})w_k \tag{2.1}$$

A real molecule is not a perfect harmonic oscillator, but is anharmonic and this can lead to a coupling of normal modes.

The normal modes for a linear ABC triatomic molecule, such as BaOH, are given in figure 2.1. These are the A-B stretching mode, B-C stretching mode and two degenerate bending modes, orthogonal to each other [25]. For the alkaline earth hydroxides the vibrations are denoted by $(v_1, v_2^{|l|}, v_3)$ with v_i denoting the quanta in a particular vibrational mode where

v_1 is the metal-oxygen stretch, v_2 the degenerate bending vibration and v_3 the oxygen-hydrogen stretch. $|l|$ denotes the vibrational angular momentum, which will be explained later.

Again similar to a diatomic molecule the rotational structure of a linear molecule can be described by a linear rigid rotor, with energy eigenvalues given by:

$$\hat{H}_{rot}\psi_{rot} = N(N+1)B\psi_{rot}, \tag{2.2}$$

where B is the rotational constant and N is the rotational quantum number. The wavefunction $\psi_{rot} = |N, M_N\rangle$ can be described by the two quantum numbers N and M_N where M_N is the projection of N on the space-fixed quantization axis. The wavefunctions are described by the spherical harmonics [22]:

$$|N, M_N\rangle = {}^{N}_{M_N}\, Y(\theta, \phi) \tag{2.3}$$

The rotational structure of the electronic and vibration ground state of BaOH is the same as BaF. It can be described by a Hund's case (b) coupling scheme. BaOH and BaF both have a hyperfine splitting from the nuclear spin on the hydrogen and fluorine atom respectively. The main difference is that the hyperfine splitting of BaOH is much smaller than of the hyperfine splitting BaF, because of the larger distance between the electron spin and nuclear spin. For BaOH the hyperfine splitting has never been measured [26]. Figure 2.2 (left) shows the rotational structure of the electronic and vibrational ground state of BaOH. The rotational structure similarity continues for BaOH and BaF for excited electronic and excited vibrational states. The exception is the rotational structure of the excited bending vibrations of BaOH, which are discussed below and are complicated by l-type doubling and Renner-Teller interaction.

2.1.2 l-type Doubling

In this section the mechanism responsible for l-type doubling will be discussed. Because of this l-type doubling each rotational level of a particular vibrational state is split into two states of opposite parity. This makes these states and therefore these molecules very interesting for an electron EDM experiment. These l-type doublets are not present in diatomic molecules. l-type doublets arise because polyatomic molecules can have vibrational angular momentum. Herzberg was the first who demonstrated the existence of these l-type doublets [27]. Here l-type doubling will be demonstrated for a triatomic molecule, but it is also present in more complicated molecules.

It is easiest to see how such a twofold degenerate bending vibration leads to angular momentum around the symmetry axis using a classical argument [22]. These bending vibrations have the same energy and are orthogonal to one another: one bending occurs in the y-z plane and another bending occurs in the x-z plane. If these two bending vibrations are excited simultaneously with a phase difference of 90°, the resulting motion will be a

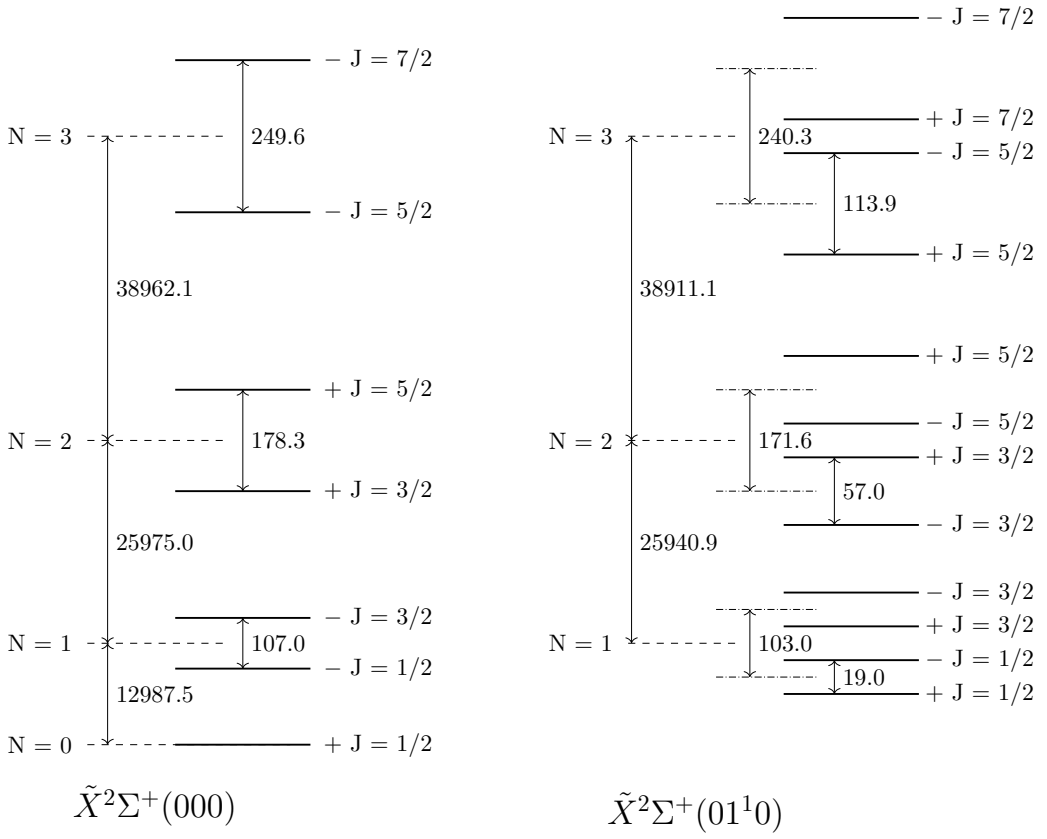

Figure 2.2: Rotational level structure of the vibrational ground state (left) and first excited bending mode (right) of the electronic ground state. Energy splitting units are in MHz. Hyperfine splitting not shown. Not to scale.

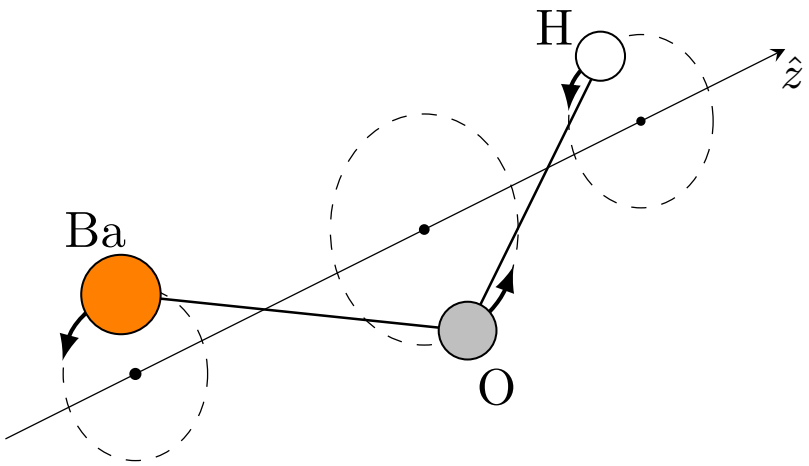

Figure 2.3: Classical description how a degenerate bending vibration of a triatomic molecule leads to a rotation around the symmetry axis. Adapted from [22].

circular motion around the symmetry axis. This is visible in figure 2.3. Since this is a rotation it has a certain angular momentum.

This classical picture is very insightful, but it is not the whole story. For a correct treatment quantum mechanics must be used. The following explanation is based on [24]. This two-dimensional bending vibration can be modelled by a two-dimensional quantum harmonic oscillator for which the Hamiltonian in Cartesian coordinates is given by:

$$\hat{H} = \frac{-\hbar}{2\mu}\left(\frac{\partial^2}{\partial x^2} + \frac{\partial^2}{\partial y^2}\right) + \frac{1}{2}k(x^2 + y^2), \tag{2.4}$$

where μ and k are the reduced mass and force constant respectively. Since x and y are separable, the solution can be written as:

$$\Psi(x, y) = \psi(x)\psi(y), \tag{2.5}$$

where ψ is the harmonic oscillator wave function. The energy eigenvalues of the Schrodinger equation are given by:

$$E = h\omega(v_x + \frac{1}{2}) + h\omega(v_y + \frac{1}{2}) = h\omega(v + 1), \tag{2.6}$$

where $v = 0, 1, 2..$ and ω is the vibrational frequency. To see how this leads to vibrational angular momentum we write equation 2.4 into plane polar coordinates:

$$\hat{H} = \frac{-\hbar}{2\mu}\left[\frac{1}{\rho}\frac{\partial}{\partial\rho}\left(\rho\frac{\partial}{\partial\rho}\right) + \frac{1}{\rho^2}\frac{\partial^2}{\partial\phi^2}\right] + k\rho^2 \tag{2.7}$$

The solution to this equation is given by:

$$\Psi(\phi, \rho) = R_{vl}(\rho)e^{il\phi} \tag{2.8}$$

Where l is a quantum number with $-v, -v+2..., v-2, v$ and R_{vl} are the generalized Laguerre polynomials. Applying the operator for angular momentum around the z-axis $L_z = -i\hbar\frac{\partial}{\partial\phi}$ returns l. l is the quantum number describing the vibrational angular momentum. For $v = 1$ the possible values for l are $l = \pm 1$. Corresponding to the classical clockwise and counterclockwise rotations around the symmetry axis. Similar to the designation of electronic states, Greek letters are used to designate the vibrational angular momentum of a vibrational state: Σ, Π, Δ for $|l| = 0, 1, 2$. For the two-dimensional harmonic oscillator the different values of $|l|$ in a specific vibrational states are degenerate. However, a vibration is never a true harmonic oscillator and these states are not degenerate, but are split.

In principle all molecules and atoms should obey parity symmetry. The parity operation is defined as the inversion of all spatial coordinates in the space-fixed frame. Thus, the parity operation should leave the molecular wave function Ψ_{mol} invariant:

$$\hat{P}\Psi_{mol} = \hat{P}\psi_{el}\psi_{vib}\psi_{rot} = \pm\Psi_{mol} \tag{2.9}$$

Since a lot of molecular properties are defined in the molecular frame, it is crucial to know the effect of the parity operation in the molecular frame. For a diatomic molecule the parity operation in the space-fixed frame is equivalent to a reflection in the molecular frame in a plane containing the internuclear axis [24]. From this it is clear that any angular momentum around the symmetry axis will violate parity symmetry. Consider Λ, the projection of electron orbital angular momentum on the internuclear axis, the parity operation on a state with $\Lambda \neq 0$ gives:

$$\hat{P}\,|\Lambda\rangle = |-\Lambda\rangle \tag{2.10}$$

Clearly this not the same state, hence it is not an eigenstate of parity. The parity eigenstates are symmetric and anti-symmetric combinations of these 2 states. This is completely analogously to the vibrational angular momentum states $||l|\rangle$. A parity operation on the $|\pm l\rangle$ state will return the $|\mp l\rangle$ state, this is thus not a parity eigenstate. The parity eigenstates are symmetric and anti-symmetric combinations of the $|\pm l\rangle$ states:

$$|\pm\rangle = \frac{1}{\sqrt{2}}\big(\,|l\rangle \pm |-l\rangle\,\big) \tag{2.11}$$

Thus, from this we see that every rotational state in a particular electronic and vibrational state with vibrational angular momentum $|l| \neq 0$ must be consist of 2 states of opposite parity.

In the molecular frame $|l|$ values are degenerate, however a molecule rotates. Coriolis

interaction [28] induces a splitting between the states of opposite parity. For $|l| = 1$ the splitting is given by [22]:

$$\Delta E = N(N+1)q_{l-type}, \tag{2.12}$$

where q_{l-type} is the l-type doubling constant, which can be experimentally determined.

The electronic and vibrational ground state can be described as a Hund's (b). However, the first excited bending vibration has vibrational angular momentum $|l| = 1$, which needs to be considered. Since the the vibrational angular momentum l does not produce a large magnetic moment in the molecular axis and the spin remains coupled to the rotation of the molecule, this state can still be treated as a Hund's case (b) [29]. An overview of the rotational level structure of BaOH is shown in figure 2.2.

It is also necessary to consider what happens if a molecule is in a state with electronic angular momentum and vibrational angular momentum. This is the case in the $\tilde{A}\Pi(v_1 1^1 v_3)$ state of BaOH. This leads to a coupling of electronic and nuclear motion and is therefore a breakdown of the Born-Oppenheimer approximation. The coupling of the electronic and nuclear motion is described by the Renner-Teller parameter ϵ. The Renner-Teller coupling splits each electronic-vibrational level into several sublevels [22]. The $\tilde{A}\Pi(v_1 1^1 v_3)$ state of BaOH with $|\Lambda| = 1$ and $|l| = 1$ is split into four levels with quantum number $K = |\Lambda + l|$: a degenerate state Δ with $K = 2$ and two Σ states with $K = 0$. The Δ is split by spin-orbit interaction into 2 states: $\Delta_{\frac{3}{2}}$ and $\Delta_{\frac{5}{2}}$. Because of the Renner-Teller effect it will become possibly to efficiently populate the first excited bending vibration from the ground state through the $\tilde{A}\Pi(01^10)$ state. This transition is normally forbidden, but becomes allowed through mixing of the spin-orbit and Renner-Teller couplings: $H_{RT} \times H_{SO}$ [13][30]. This mixes the $\tilde{B}\Sigma(000)$ and $\tilde{A}\Pi(01^10)$ vibronic states. Expressions for energy levels in ${}^2\Pi(v_2 = 1)$ states are given by [31]. An overview can also be found in Hirota [32]. These bending vibrations of excited electronic states have been investigated for CaOH [33] and SrOH [30]. For BaOH the forbidden transition $\tilde{X}^2\Sigma(01^10) - \tilde{B}^2\Sigma(000)$ has been observed [34].

2.1.3 Stark Effect

In this section the Stark effect will be discussed. The Stark effect is important in many parts of an electron EDM experiment. Of course the Stark effect is important for the Stark decelerator, but it is also responsible for the polarization of the molecule in the interaction zone. Furthermore, by understanding the Stark effect certain benefits of polyatomic molecules over diatomic molecules can be better understood.

The Stark effect is the splitting of energy levels in an electric field. It is the electrical analogue of the Zeeman effect: the splitting of energy levels in a magnetic field.

The Stark effect occurs in both atoms and molecules. In the context of this thesis we will focus on the Stark effect for molecules. A polar molecule has a dipole moment. This dipole moment has an energy in an electric field, which we need to add to the Hamiltonian of the system. The energy of a dipole in an electric field is given by:

$$V = \vec{E} \cdot \vec{d} \tag{2.13}$$

In this equation $\vec{E}$ is the electric field vector and $\vec{d}$ is the dipole moment vector, which is given by:

$$\vec{d} = q\vec{r}, \tag{2.14}$$

$\vec{r}$ is the displacement vector between the 2 particles and q is the charge of the particle. It is convenient to let the electric field point along the z-axis in our coordinate system. The expression for the energy of a dipole from the Stark interaction that we need to add to the Hamiltonian of our system is [35]:

$$\hat{H}_s = \vec{E} \cdot \vec{d} = E d_{mol} \cos\theta, \tag{2.15}$$

E is the electric field magnitude, $\vec{d}$ is dipole operator and θ is the angle between the molecular dipole moment d_{mol} and the electric field. This interaction is normally treated as a perturbation to the zero-field Hamiltonian H_0.

Lets first investigate the dipole operator $\vec{d}$ [36]. The dipole moment operator is a vector operator. This means that this operator has odd parity:

$$\hat{P}\vec{d} = -\vec{d} \tag{2.16}$$

Consider a molecular state $|\psi_a\rangle$ with parity ϵ_a and a state $|\psi_b\rangle$ with parity ϵ_b. ϵ_a and ϵ_b can be either ± 1. The expectation value of the dipole operator in this state is $\langle\psi_a|\,\vec{d}\,|\psi_b\rangle$. Since $\hat{P}^\dagger\hat{P} = 1$ and $\hat{P}^\dagger\vec{d}\hat{P} = -\vec{d}$:

$$\langle\psi_a|\,\vec{d}\,|\psi_b\rangle = \langle\psi_a|\,\hat{P}^\dagger\hat{P}\vec{d}\hat{P}^\dagger\hat{P}\,|\psi_b\rangle = -\epsilon_a\epsilon_b\,\langle\psi|\,\vec{d}\,|\psi\rangle \tag{2.17}$$

$\langle\psi_a|\,\vec{d}\,|\psi_b\rangle \neq 0$ can only be true if $\epsilon_a \neq \epsilon_b$. Since:

$$\langle\psi_a|\,\hat{H}_s\,|\psi_b\rangle = \langle\psi_a|\,\vec{E}\cdot\vec{d}\,|\psi_b\rangle = \vec{E}\cdot\langle\psi_a|\,\vec{d}\,|\psi_b\rangle \tag{2.18}$$

Therefore, the Stark Hamiltonian is only nonzero for states of opposite parity.

Since the Stark effect couples states of opposite parity the zero-field eigenstates are not the good eigenstates in the presence of an electric field. The Stark effect mixes states of opposite parity. Initially the Stark shift is quadratic, but once the states are fully mixed the Stark shift becomes linear. This mixing effectively induces a dipole moment in the laboratory frame by orienting the molecule with respect to the electric field. Once the molecule is fully oriented and the Stark shift becomes linear the molecule is considered fully polarized.

The following example of the Stark effect is based on [36] and [37]. This example will be used to illustrate some of the general features of the Stark effect.

Consider a two-level system. The two states have opposite parity. Level $|e\rangle$ has energy Δ and level $|g\rangle$ has energy $-\Delta$. The zero-field Hamiltonian H_0 is therefore equal to:

$$H_0 = \begin{pmatrix} \Delta & 0 \\ 0 & -\Delta \end{pmatrix} \tag{2.19}$$

If an electric field is introduced the Stark effect induces a coupling between these two states of opposite parity. The matrix elements that couple these states are given by $-\langle e|\, \vec{d}\cdot\vec{E}\, |g\rangle = -\langle g|\, \vec{d}\cdot\vec{E}\, |e\rangle = -dE$. The Hamiltonian of this system in the zero-field basis is then given by:

$$H_0 = \begin{pmatrix} \Delta & -dE \\ -dE & -\Delta \end{pmatrix} \tag{2.20}$$

In order to find the new eigenvalues in the presence of an electric field we must diagonalize this Hamiltonian. If we do this we find:

$$H_0 = \begin{pmatrix} +\sqrt{\Delta^2 + (dE)^2} & 0 \\ 0 & -\sqrt{\Delta^2 + (dE)^2} \end{pmatrix} \tag{2.21}$$

Hence, the new eigenvalues are $\pm\sqrt{\Delta + (dE)^2}$. If $Ed << \Delta$ we can approximate the stark energies as $\approx \pm\Delta + (dE)^2$. Therefore, the Stark shift is initially quadratic. If $Ed >> \Delta$ we can approximate the stark energies as $\approx \pm(dE)$ and the Stark effect becomes linear. From these equations it is visible that the electric field where the transition from a quadratic to a linear Stark shift happens depends on the splitting between these 2 states of opposite parity. The Stark effect for this simple 2-level system is plotted in figure 2.4. When the Stark shift becomes linear the eigenstates are equal to $\approx \frac{1}{\sqrt{2}}(|e\rangle \pm |g\rangle)$ in other words the states are fully mixed.

In general states of atoms and molecules can be labeled by their angular momentum J and the projection of J on a space-fixed quantization axis M_J. In an electric field different states will mix and J is not a good quantum number anymore. Only the projection on the space-fixed quantization axis M_J is conserved (the electric field).

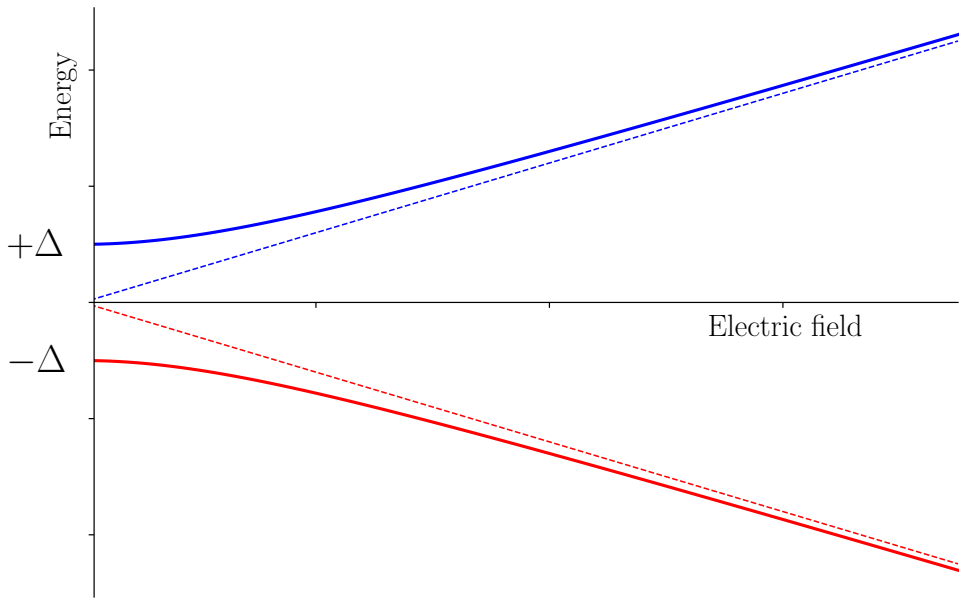

Figure 2.4: Stark shift of a simple two-level system. $|e\rangle$ is represented by the blue line. $|g\rangle$ is represented by the red line. The dotted line represents a linear trend for the corresponding level.

2.2 Traveling-Wave Stark Decelerator

An important part of the NL-eEDM experiment that sets it apart from other eEDM experiments is the traveling-wave Stark decelerator. Combined with a cryogenic source it is possible to create a slow molecular beam and it is possible to reach long interaction times.

A traveling-wave Stark decelerator is a variant of the traditional Stark decelerator. A traveling-wave Stark decelerator works by creating macroscopic traveling traps [38]. Initially the traps move at the same speed as the molecules. Once the molecules are trapped the speed of the traps is reduced and the molecules are decelerated.

A detailed description of the decelerator can be found in [39]. The decelerator consists of a periodic array of ring shaped electrodes. By applying a sinusoidal high-voltage with a phase difference of $\frac{\pi}{4}$ between each successive electrode the macroscopic electrostatic traps are created. The amplitude of the high-voltage waveform determines the maximum electric field inside the decelerator. The expression for the voltage applied to the electrodes is given by:

$$V_n(t) = V_0 \sin\left(ft + n\frac{\pi}{4}\right) \tag{2.22}$$

V_0 is the amplitude of the high-voltage waveform, f is the frequency and t is the time. This is implemented by connecting every eighth electrode to the same high-voltage amplifier. The traps are decelerated by reducing the frequency of the high-voltage waveforms.

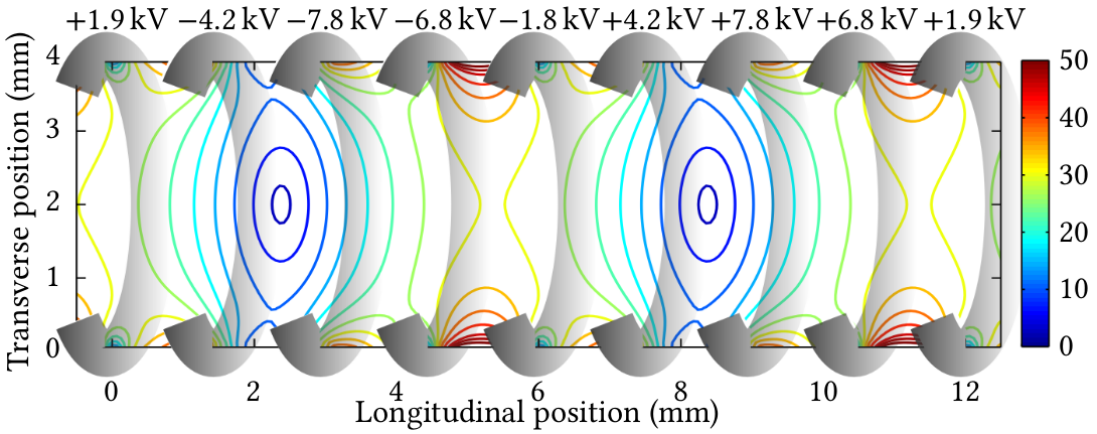

Figure 2.5: Electric field inside a traveling-wave Stark decelerator [39].

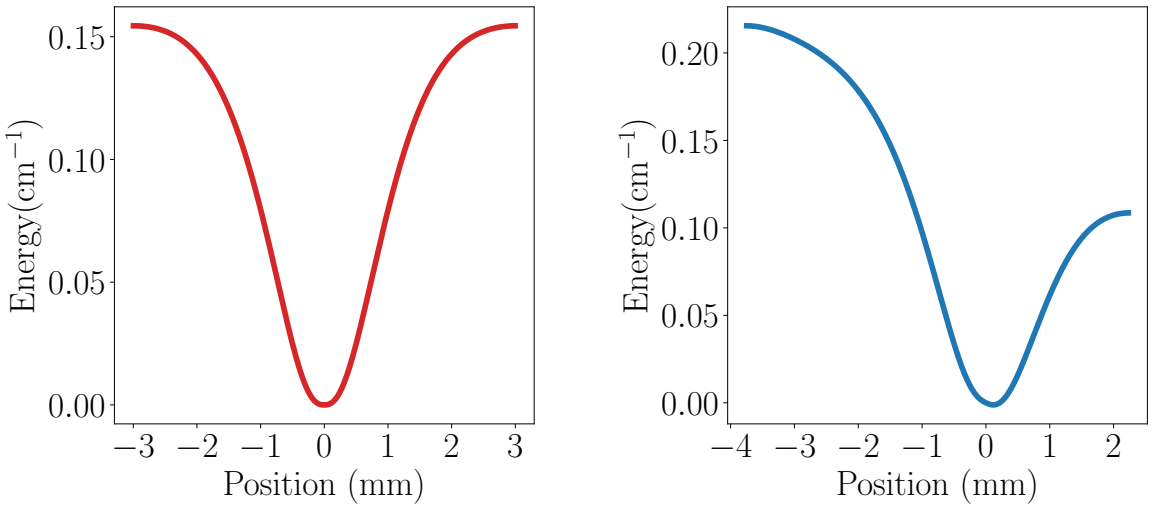

Figure 2.6: Effective electric potential for a SrF $|1,0\rangle$ molecule in a TWSD in the longitudinal direction. Left figure shows guiding, right figure shows deceleration with 2 km/s^2.

Neutral polar molecules can be trapped in electric traps because of the Stark effect, which was explained in the previous section. The moving electric traps have zero electric field at their center. Molecules in states which have their minimum energy at zero-field can be decelerated in a traveling-wave Stark decelerator. These states are called low-field seeking states. States for which the energy decreases with increasing electric field are called high-field seeking. Since the electric field is inhomogeneous the molecules feel a force towards the lowest electric field: the center of the trap. The force is given by:

$$F = -\nabla E_{Stark}(\varepsilon) \tag{2.23}$$

As an example the Stark effect of SrF is plotted in figure 2.7. Eventually at an high enough electric field all Stark curves will become high-field seeking. This turning point of the Stark curve determines the maximum depth of the trap. Therefore, for each rotational state there is an optimal voltage that should be applied to the electrodes. The depth of the potential determines the maximum deceleration and the spatial and velocity acceptance of the decelerator. The effective potential of SrF in a Stark decelerator is plotted in figure 2.6.

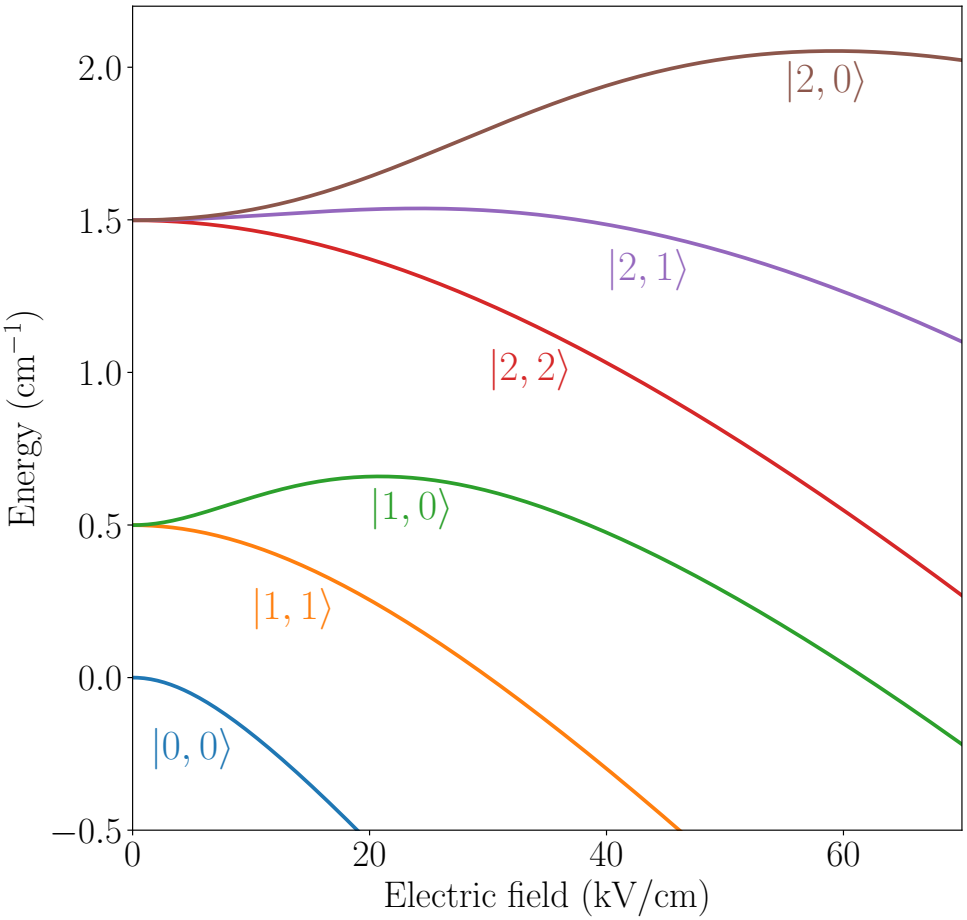

Figure 2.7: Stark effect for SrF. The states are labeled by their zero-field quantum numbers $|N, M_N\rangle$. The $|1,0\rangle$ and $|2,0\rangle$ are initially low-field seeking, but become high-field seeking at 25kV/cm and 60kV/cm respectively.

2.3 BaOH Spectroscopic Data

There has been done some spectroscopy on BaOH in the past. In table 2.1 molecular constants of BaOH used throughout this thesis are summarized. Some remarks about these constants:

The dipole moment μ_D of the excited bending vibration of the electronic ground state is assumed to be the same as the absolute ground state. The Fermi contact constant b is not known for any state of BaOH and is taken from [13]. The dipole moment μ_D of the $\tilde{A}$ state is of the $\Pi_{\frac{3}{2}}$ state. Other spectroscopy done is [34][44][45][46][47][48].

	$X^2\tilde{\Sigma}_{\frac{1}{2}}(000)$	$X^2\tilde{\Sigma}_{\frac{1}{2}}(01^10)$	$\tilde{A}(000)$
B	6493.775 [26] MHz	6485.264 MHz [40]	5777.513 MHz [41]
D	0.004924 MHz [26]	0.005010 MHz [40]	0.00367 MHz [41]
A	-	-	605.83684 cm^{-1} [41]
γ	71.325MHz [26]	68.65MHz[40]	-
μ_D	1.43D [42]	1.43D [42]	0.477D [42]
b	-	2 MHz	-
ω_i	-	342 cm^{-1} [43]	-
p	-	-	-5377.6171 MHz [41]
q	-	-	0.432 MHz [41]
$q_{l_{type}}$	-	-9.4932 MHz[40]	-

Table 2.1: Molecular constants of BaOH used throughout this thesis.

Chapter 3

Stark Effect of BaOH

3.1 Method

In this chapter the Stark effect of BaOH will be calculated. To find the Stark effect of a molecule in a particular electronic and vibrational state it is necessary to solve the time-independent Schrödinger equation at a finite number of electric field points. The time-independent Schrödinger equation is given by:

$$\hat{H} |\psi\rangle = E |\psi\rangle \tag{3.1}$$

Our Hamiltonian $\hat{H}$ consist of a zero-field part $\hat{H}_0$ and an electric field dependent part $\hat{H}_{Stark}$. The Stark shift at a particular electric field strength can be found by writing down the Hamiltonian in the zero-field basis and diagonalizing it.

The matrix is truncated after including a finite number of rotational states. Enough states are included such that the Stark shift converges. This is checked by increasing the number of rotational states and looking how much the Stark shift changes. Far more rotational states are included than needed (typically N = 15).

The calculation of the Stark effect is done using a program written in Python. The diagonalization is done with the numpy.linalg.eig module. Matrix diagonalization returns the eigenvalues of the matrix with the corresponding eigenvectors. The eigenvectors that are returned are used to match the eigenvalues with eigenvalues at other electric field points. This allows us to compute the effective dipole moment of the state by taking the numerical derivative of the corresponding Stark curve.

The Stark effect of BaOH is calculated for a number of states. It is calculated for the electronic and vibrational ground state (The $\tilde{X}^2\Sigma^+(000)$) and the first excited bending vibration ($\tilde{X}^2\Sigma^+(01^10)$).

Below the matrix elements to calculate these Stark shifts are given.

3.1.1 Matrix Elements

When the Stark splitting is much larger than the fine structure splitting and hyperfine splitting it is possible to use a model that only takes into account the rotational structure of the molecule. This makes the calculation of the Stark effect computationally easier, especially in a higher electric field, where there is a substantial mixing of different rotational states. This is the case in the Stark decelerator, hence to asses the suitability of this molecule for the traveling-wave Stark decelerator we will use this simpler model. The matrix elements are given in terms of the Wigner-3j(round brackets) and Wigner-6j(curly brackets) symbols respectively.

Essentially a linear molecule in an excited bending vibration is a symmetric top molecule [29]. Thus, we will use the following effective Hamiltonian, neglecting fine and hyperfine interaction.

The basis in which we evaluate this Hamiltonian is $|N, P, M\rangle$. Where N is the rotational quantum number, P the parity and M the projection of N on the space-fixed quantization axis. The parity eigenstates are the symmetric and anti-symmetric combinations of the vibrational angular momentum eigenstates $|N, \pm l, M\rangle$:

$$|N, \pm, M\rangle = \frac{1}{\sqrt{2}}\big(|N, +l, M\rangle \pm |N, -l, M\rangle \big) \tag{3.2}$$

The rotational structure of this molecule is given by:

$$\langle N', P', M'| \hat{H}_{rot} |N, P, M\rangle = \delta_{P'P}\delta_{N'N}\delta_{M'M}(N(N+1) - |l|^2)B \tag{3.3}$$

B is the rotational constant and N ≥ 1, since we have $|l| = 1$. Furthermore, the states of opposite parity are not degenerate and are split by Coriolis interaction. This splitting is given by:

$$\langle N', P', M'| \hat{H}_{Parity} |N, P, M\rangle = \pm\delta_{P'P}\delta_{N'N}\delta_{M'M}\frac{1}{2}qN(N+1) \tag{3.4}$$

Where the sign depends if the parity is positive or negative. The matrix element for the Stark interaction is given by [49]:

$$\begin{aligned}\langle N', l', M'| \hat{H}_{stark} |N, l, M\rangle = Ed(-1)^{Np-Mp}\sqrt{(2N'+1)(2N+1)} \\ \times \begin{pmatrix} N' & 1 & N \\ -M' & 0 & M \end{pmatrix} (-1)^{N'-l'} \begin{Bmatrix} N' & 1 & N \\ -l' & 0 & l \end{Bmatrix}\end{aligned} \tag{3.5}$$

The above formula is in the l-basis. In the calculation it is transformed to the zero-field(parity) basis according to equation 3.2 and added to $\hat{H}_0$.

If the stark energy splitting is of the order of the fine structure splitting and hyperfine

splitting, these interactions must be taken into account. To do this we will use the model of Kozyryev and Hutzler [13].

The effective Hamiltonian consist of the following part:

$$H_{eff} = H_0 + H_{Stark} \tag{3.6}$$

The zero-field Hamiltonian H_0 is given by:

$$H_0 = H_{sr} + H_{hf} + H_{l-doubling} \tag{3.7}$$

In this equation H_{sr} is the spin-rotation interaction, H_{hf} is the hyperfine interaction and $H_{l-doubling}$ is the interaction responsible for l-doubling.

A $^2\Sigma$ Hund's case (b) Hamiltonian is used to describe the spin-rotation structure. This Hamiltonian has been used to analyze spectroscopic results of the alkaline earth hydroxides [40] in excited bending vibrations. The matrix elements of this Hamiltonian in the $|NlSJIFM\rangle$ basis are:

$$\begin{aligned}\langle NlSJIFM|\, H_{sr}\, |NlSJIFM\rangle = \gamma\delta_{ll'}(-1)^{N+J+S} \begin{Bmatrix} S & N & J \\ N & S & 1 \end{Bmatrix} \\ \times[S(S+1)(2S+1)N(N+1)(2N+1)]^{1/2}\end{aligned} \tag{3.8}$$

To describe the hyperfine interaction the matrix elements given by Hirota [32] are used. Only the Fermi contact interaction is included since it is so much larger than the other interactions:

$$\begin{aligned}\langle N'l'SJ'IF'M'|\, H_{hf}\, |NlSJIFM\rangle = \\ b_\eta\delta_{ll'}\delta_{MM'}\delta_{FF'}\delta_{NN'}(-1)^{N+S+J'}(-1)^{J+I+F+1} \\ \times[S(S+1)(2S+1)I(I+1)(2I+1)]^{1/2} \\ \times[(2J'+1)(2J+1)]^{1/2} \begin{Bmatrix} I & J' & F \\ J & I & 1 \end{Bmatrix} \begin{Bmatrix} S & J' & N \\ J & S & 1 \end{Bmatrix}\end{aligned} \tag{3.9}$$

The zero-field eigenstates cannot be expressed in terms of l. The zero-field eigenstates are the parity eigenstates, which are given by:

$$|N,\pm,J,F,M\rangle = \frac{1}{\sqrt{2}}\big(\,|N,+l,J,F,M\rangle \pm |N,-l,J,F,M\rangle\,\big) \tag{3.10}$$

These states are not degenerate. Coriolis interaction lifts the degeneracy between these two states. Each of these states shifts $\pm\frac{1}{2}qN(N+1)$ in energy.

The expression for the Stark interaction is also given by Hirota:

$$\begin{aligned}\langle N', l', S, J', I, F', M'| H_{Stark} |N, l, S, J, I, F, M\rangle = \\ \varepsilon d(-1)^{F'-M} \begin{pmatrix} F' & 1 & F \\ -M' & 0 & M \end{pmatrix} \\ \times(-1)^{J'+I+F+1}[(2F'+1)(2F+1)]^{1/2} \begin{Bmatrix} J' & F' & I \\ F & J & 1 \end{Bmatrix} \\ \times(-1)^{N'+S+J+1}[(2J'+1)(2J+1)]^{1/2} \begin{Bmatrix} N' & J' & S \\ J & N & 1 \end{Bmatrix} \\ \times(-1)^{N'-l'}[(2N'+1)(2N+1)]^{1/2} \begin{pmatrix} N' & 1 & N \\ -l' & 0 & l \end{pmatrix}\end{aligned} \tag{3.11}$$

Note that in the article of Hutzler and Kozyryev the term $[(2N+1)(2N'+1)]^{1/2}$ is left out, but this term is present in Hirota.

To calculate the Stark shift as a function of the electric field, equation 3.11 is written in terms of the parity eigenstate using equation 3.10 and added to the zero-field Hamiltonian.

The Stark curves in this section are labeled by their zero-field quantum numbers. Note that the hyperfine interaction couples different J within a single rotational level. J is thus not a good quantum number in the presence of hyperfine interaction. However, we keep labeling these states by J, although this is not strictly correct.

If the states are labeled by their parity. They are labeled by their total parity. Which also depends on the rotational quantum number N. The effect of the parity operation on the symmetric top wavefunction is given by(we use K = l)[24]:

$$\hat{P} |N, K, M\rangle = (-1)^{N-K} |N, -K, M\rangle \tag{3.12}$$

The Stark effect for ${}^2\Sigma_{\frac{1}{2}}$ molecules with and without hyperfine structure will also be shown. These are approximately the same as above. However, since l-doubling is not present l must be set to zero.

In principle this calculation for the first excited bending vibration can also be done in the molecular spectrum simulation program PGOPHER[50]. For the calculation in a high electric field (neglecting fine and hyperfine interaction) the molecule can be treated as a symmetric top molecule with K = l = 1. For a smaller electric field, fine and hyperfine structure must be taken into account. The molecular constants can just be entered as usually. However, PGOPGER does not include vibrational angular momentum l. Instead, Λ = l must be chosen. This state can still be treated as a Hund's case (b). Thus, the spin-orbit constant A must be set to zero. This produces similar results as given below, however, the total parity assignment given in PGOPHER is wrong.

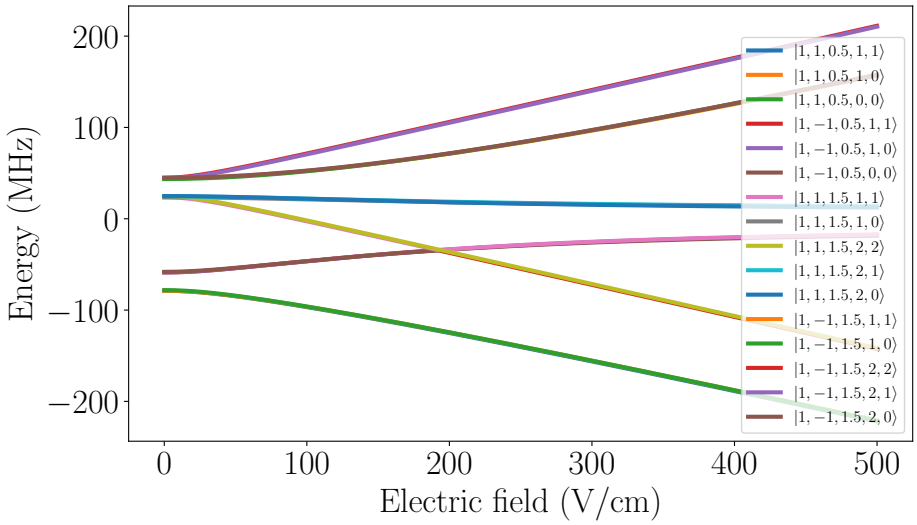

Figure 3.1: Stark shift of N = 1 state of BaOH. States are labeled by their zero-field quantum numbers in the basis $|N, P, J, F, M\rangle$.

3.2 Result and Discusion

We begin by discussing the Stark effect of the first excited bending mode in a low electric field. This regime is is of interest for an eEDM measurement. The Stark effect of BaOH obtained by diagonalizing the full Hamiltonian described above is given in figure 3.1. An overview of the zero-field states in shown in figure 3.2. As expected for a system with a small spacing between states of opposite parity the Stark shift rapidly becomes linear. From the Stark curves the effective dipole moment in the laboratory frame can be determined. The effective dipole moments for the different states of BaOH are plotted as a function of electric field in figure 3.3.

3.2.1 Polarization

The parameter of interest is the polarization factor. Molecules with close lying states of opposite parity can be fully polarized in a low electric field. To determine the necessary field to fully polarize BaOH, the effective dipole moment is divided by the dipole moment of the N = 1 state, given by [37]:

$$D_N = \frac{d}{N(N+1)}, \tag{3.13}$$

where d is the molecular dipole moment. The result is plotted in figure 3.3. From this we find that BaOH is fully polarized in a field of 1500V/cm. (All states that can be used in an eEDM experiment are fully polarized in this field). The $|1, \pm 3/2, 2, |1, 2|\rangle$ states are most easily polarized. They are fully polarized in an electric field of 300 V/cm. In this picture the co-magnetometer states are also clearly visible: these states are fully polarized

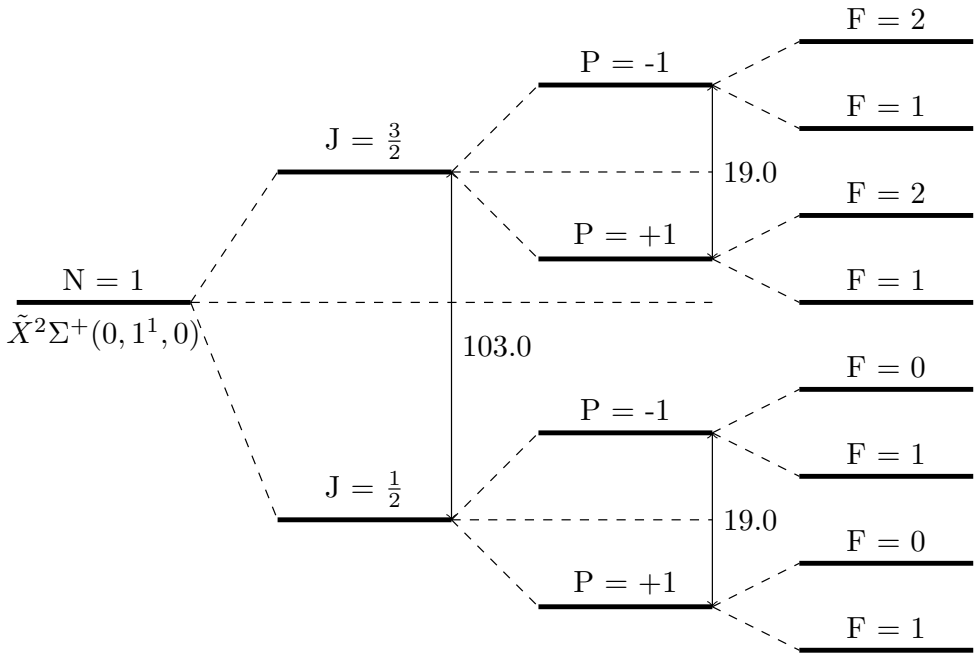

Figure 3.2: Zero-field level structure of the eEDM state of BaOH. Splittings are given in MHz. Only measured splittings are shown. Not to scale.

but have an opposite sign. A good explanation why the eEDM interaction is reversed in these state can be found in [13].

To illustrate the difference with BaF the polarization of the lowest rotational states is shown in figure 3.4. The polarization of BaF at 10kV/cm is ≈50%. For BaOH this is a factor 2 higher at a much lower electric field, which aside from the suppression of systematic effects, also means an increase in statistical uncertainty from the increased polarization factor(since these molecules have approximately the same internal electric field).

A difference with the co-magnetometer states of ThO is that the zero-field splitting for BaOH is much larger [51] (350kHz vs 20MHz) and the rotational constant is also smaller. This means that, in an electric field, there is a larger mixing of different rotational states, which can lead to an magnetic g-factor difference between co-magnetometer states and cause a different energy shift in those states [52]. However, this effect has been considered in other molecules with co-magnetometer states and can be corrected for [53][37].

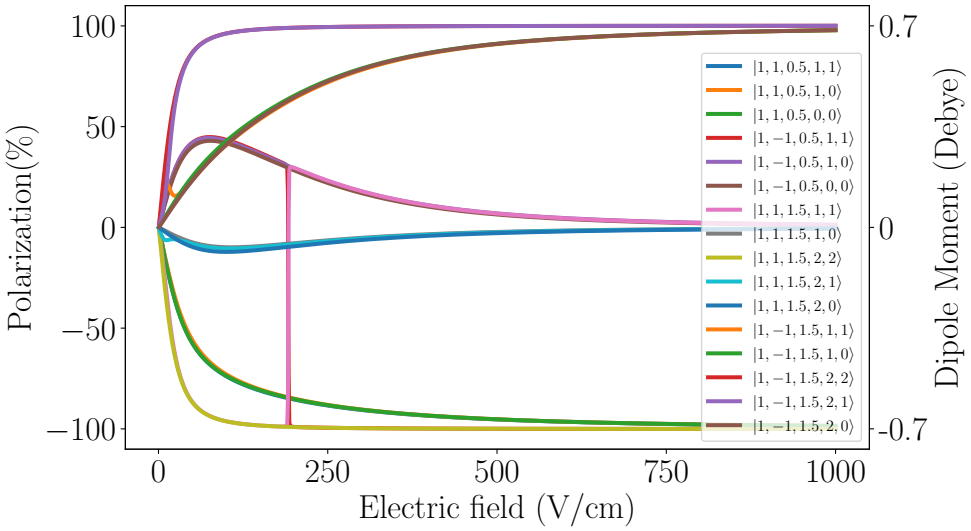

Figure 3.3: Polarization of the N = 1 state of BaOH. States are labeled by their zero-field quantum numbers in the basis $|N, P, J, F, M\rangle$.

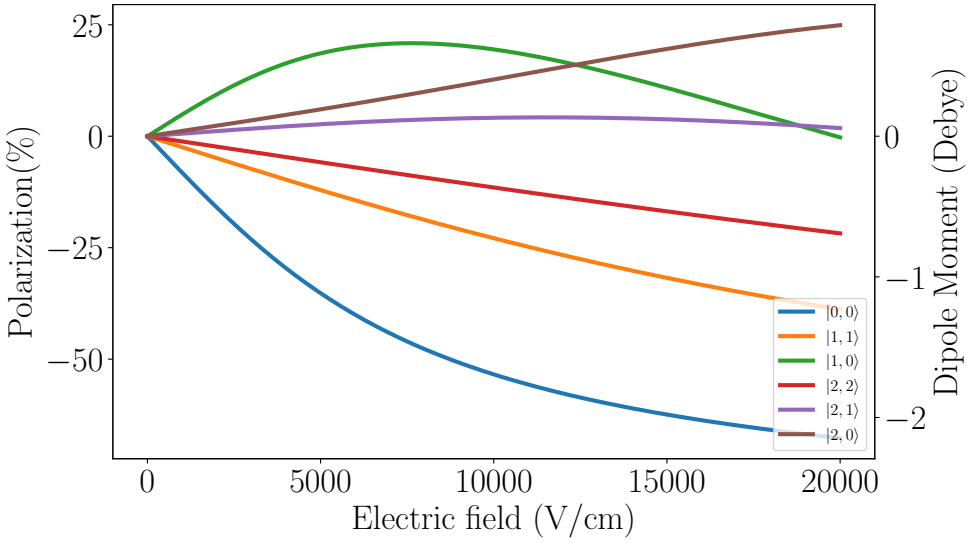

Figure 3.4: Polarization of the lowest rotational states of BaF. The $|N, M\rangle = |0, 0\rangle$ is the eEDM state. The polarization is the same for the hyperfine components.

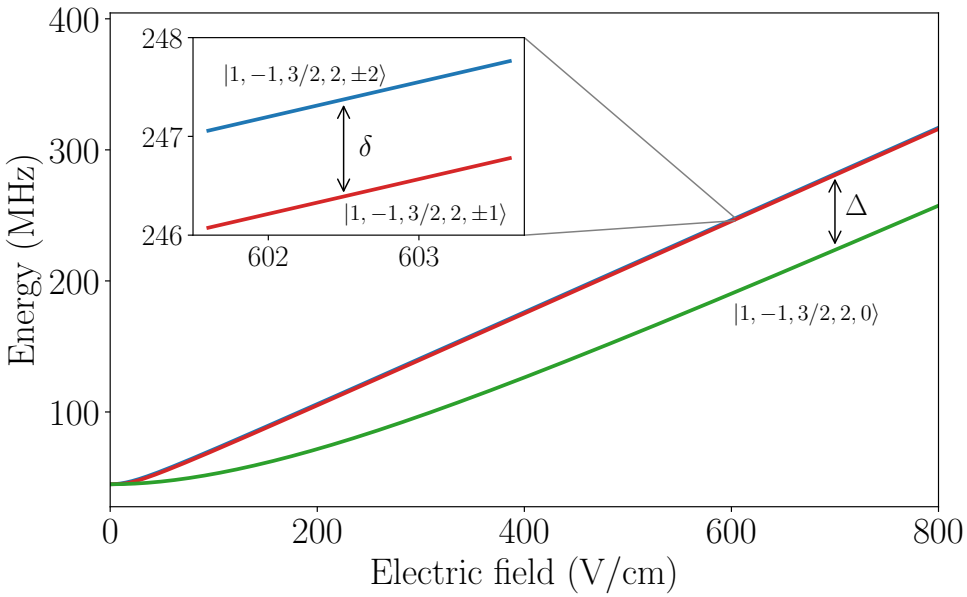

Figure 3.5: Tensor Stark splitting of the P = -1, F = 2 hyperfine level. States are labeled by their zero-field quantum numbers $|N, P, J, F, M\rangle$.

3.2.2 Tensor Stark Shift

An important feature present in molecules is the large tensor Stark shift [54]. This shift can be used to suppress systematic errors related to a radial magnetic field. The tensor Stark shift is essentially a shift between the same the M_F levels of the same hyperfine level. Here we consider the $F = 2$ hyperfine level for an eEDM measurement. This is shown in figure 3.5. As visible there is a large energy difference between $M_F = \pm1, 2$ states and the $M_F = 0$ state and a relative small difference between the $M_F = \pm2$ and $M_F = \pm1$ states. To estimate the effect of radial magnetic fields for such a type of molecule we will follow the approach of [54], but apply it to the F = 2 level(instead of the F = 1 level as is the case for a diatomic molecule like YbF or BaF). Here we consider the (zero-field) F = 2, P = -1 hyperfine level, but the results should be equally valid for the other parity doublet component F = 2, P = 1, since energy splittings are similar. (Here we treat this level as a spin-2 particle, because F = 2, and do not consider the effect of substantial mixing with other hyperfine levels, which might not be negligible. This calculation should thus be considered as a crude estimation):

The (simplified) Hamiltonian for a spin-2 particle with a magnetic field is given by equation 3.14.

$$\hat{H} = \hat{H}_0 + \vec{B} \cdot \vec{S} = \hat{H}_0 + B_z S_z + B_r S_x = \hat{H}_0 + \mu_B \sigma_z B_z + \mu_B \sigma_x B_r, \tag{3.14}$$

where μ_B is the Bohr magneton and σ_x and σ_z are the standard spin-2 matrices. Writing out this Hamiltonian in matrix form in the basis $|F, M\rangle$ with $F = 2$ and $M = -2, -1, 0, 1, 2$. The eigenvalues of the zero-field Hamiltonian are determined by the tensor Star shift. We

define Δ as the energy difference between $|2,0\rangle$ and $|2,\pm1\rangle$, δ is defined as the energy difference between $|2,\pm1\rangle$ and $|2,\pm2\rangle$. We find:

$$\hat{H} = \frac{1}{2}\mu_B \begin{pmatrix} \frac{2\Delta+2\delta}{\mu_B} + 4B_z & 2B_r & 0 & 0 & 0 \\ 2B_r & \frac{2\Delta}{\mu_B} + 2B_z & \sqrt{6}B_r & 0 & 0 \\ 0 & \sqrt{6}B_r & 0 & \sqrt{6}B_r & 0 \\ 0 & 0 & \sqrt{6}B_r & \frac{2\Delta}{\mu_B} - 2B_z & 2B_r \\ 0 & 0 & 0 & 2B_z & \frac{2\Delta+2\delta}{\mu_B} - 4B_z \end{pmatrix} \tag{3.15}$$

Since $\Delta \gg \delta > B_z > B_r$ we can treat the effect of $S_x B_r$ as a perturbation to $\hat{H}_0 + S_z B_z$. second-order perturbation theory gives us the energy of the $|2,\pm2\rangle$ state:

$$E(|2,\pm2\rangle) = \Delta + \delta \pm 2\mu_B B_z + \frac{(\mu_B B_r)^2}{\delta \pm \mu_B B_z} \tag{3.16}$$

Again similar to [54] we are interested in the difference between the states $|2,2\rangle$ and $|2,-2\rangle$:

$$|2,+2\rangle - |2,-2\rangle = 4\mu_B B_z + (\mu_B B_r)^2\big(\frac{1}{\delta + \mu_B B_z} - \frac{1}{\delta - \mu_B B_z}\big) \tag{3.17}$$

$$\approx 4\mu_B B_z - 2\frac{(\mu_B B_r)^2 \mu_B B_z}{\delta^2}$$

Hence, this result is similar to [54]. The induced splitting is a factor two higher. The suppression factor S, the relation between an radial magnetic field and the induced energy difference between the states (the derivative with respect to the axial magnetic field), is given by:

$$S = (-)4\frac{\mu_B^2 B_r B_z}{\delta^2} \tag{3.18}$$

This result shows how the tensor Stark splitting suppresses a fake eEDM signal from a radial magnetic field.

Note that because of the very large shift Δ compared to δ, the matrix element that couples the states $|2,\pm1\rangle$ and $|1,0\rangle$ is much smaller than the matrix element that couples the states $|2,\pm2\rangle$ and $|2,\pm1\rangle$, thus only this element needs to be kept. The suppression factor is therefore the same for this state.

So, for a triatomic molecule in an excited bending state like BaOH or YbOH using $|2,\pm2\rangle$ as the eEDM state suppression factor depends on the energy splitting between $|2,\pm1\rangle$ and $|2,\pm2\rangle$ not on the difference with $|2,\pm0\rangle$. Although δ is much smaller than Δ it is still sizable. We do not know the hyperfine constants for this molecule, but the assumption of a value for b = 2MHz gives a splitting of 1MHz, which is comparable to the tensor splitting in a molecule such as BaF. In [54] a number of systematic errors are given related to a radial magnetic field. However, due to the ability to fully polarize this molecule and the

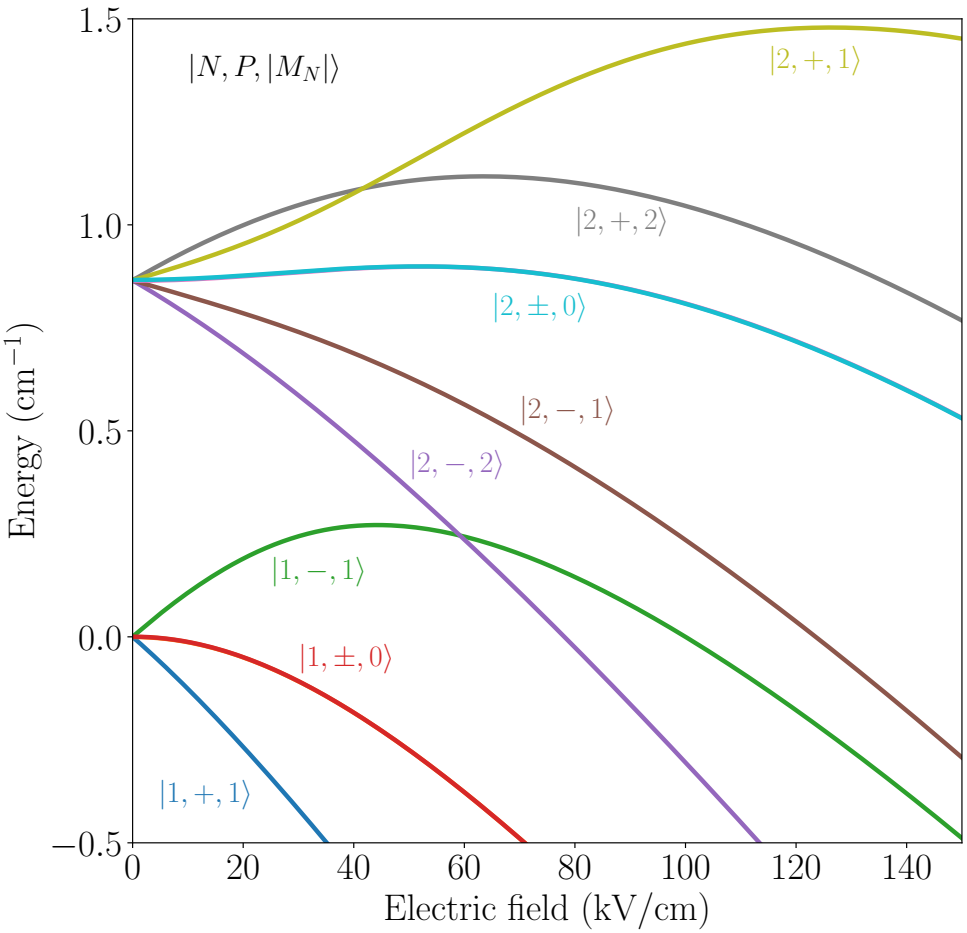

Figure 3.6: Stark shift of BaOH for the N = 1 and N = 2 rotational states in an high electric field. States are labeled in the zero-field basis $|N, P, M\rangle$.

existence of internal co-magnetometer states these effects are also suppressed. For example, it is stated that it is especially troublesome if the radial magnetic field is correlated to the orientation of the applied magnetic field with electric field, since this mimics the signal of an eEDM. However, because of the internal co-magnetometer states there is no need to reverse the electric field.

3.2.3 Traveling-Wave Stark Deceleration

To determine the suitability for traveling-wave Stark deceleration of this molecule. We are interested the Stark-effect between 0kV/cm and 50kV/cm, since this correspond to the electric field in the decelerator. With a dipole moment of 1.4D the electronic and vibrational ground state of this molecule is not very suited for Stark deceleration, this is depicted in figure 3.8. Since the rotational constants of BaF and BaOH are almost the same the turning points of the Stark curves have the same energy/height, but because of

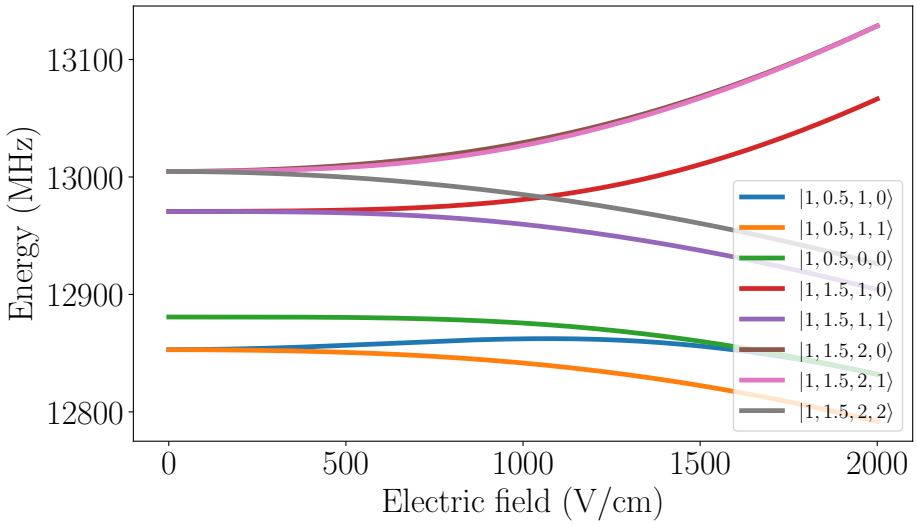

Figure 3.7: Stark shift of BaF N = 1 state in a low electric field (E < 3000V/cm). States are labeled in the zero-field basis $|N, J, F, M\rangle$. Low and high-field seeking states are degenerate at zero electric field.

the smaller dipole moment the electric field necessary to reach this turning point is larger than can be made in the decelerator. However, in the vibrational excited bending mode the Stark shift is initially linear and therefore the Stark shift could be large enough to allow for efficient traveling-wave stark deceleration. The Stark shift of the first two rotational levels of the (01^10) vibrational state is depicted in figure 3.6. From this picture we see that the $|1, -1, 1\rangle$ $|2, 1, 2\rangle$ and $|2, 1, 1\rangle$ states are most suited for Stark deceleration. The low-field seeking states of this molecule are plotted together with the low-field seeking states of the isoelectronic molecule BaF in figure 3.8.

In the next chapter we will simulate the traveling-wave Stark deceleration for this molecule, however, from the Stark effect for this molecule there are some clear observations we can make. If we look at the hyperfine structure in figure 3.1 of this molecule around a field of 0 kV/cm we see that the low-field seeking states are well separated from the high-field seeking states by about 20MHz for the N = 1 state. This splitting increases with rotational quantum number. This is different for a molecule such as SrF or BaF where the low and high-field seeking states are degenerate at zero-field. As an illustration the Stark shift of the N = 1 level of BaF is plotted in figure 3.7. In a Stark decelerator the molecules move through the electric fields of the traveling traps. It is assumed that that the molecules follow this field adiabatically. However, this assumption breaks down if the field changes rapidly compared to the energy splitting with other states. The rotation of the electric field can drive nonadiabatic transitions to other states. If these states are non-trapped the molecule is lost for the deceleration process. It was shown that at guiding there is a large loss of SrF molecules due to nonadiabatic transitions in a traveling-wave Stark decelera-

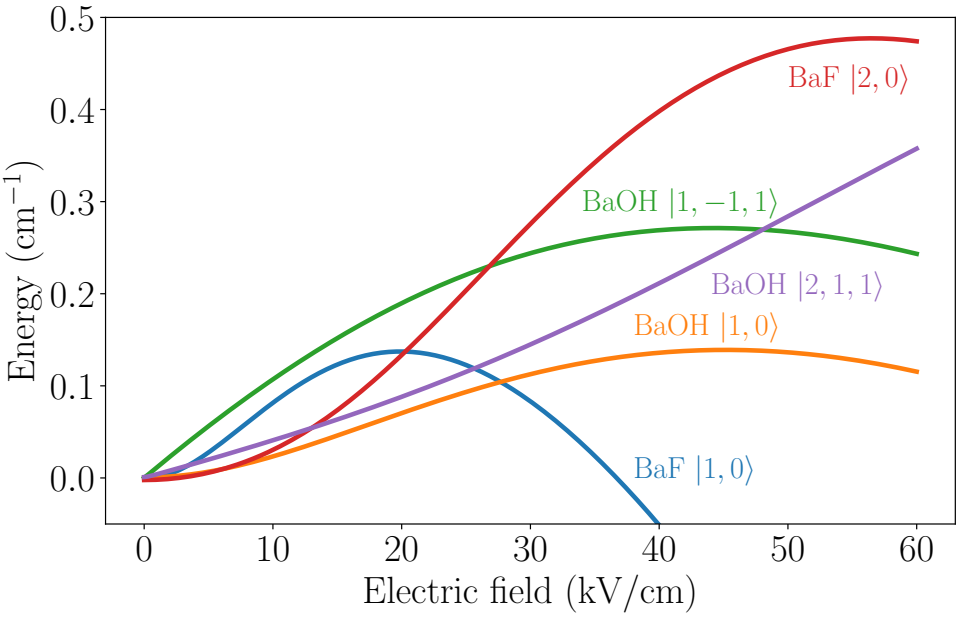

Figure 3.8: Stark shifts of BaOH and BaF for different rotational and vibrational levels. An offset is added so that all curves go through zero.

tor [55]. These types of losses have also been investigated for other decelerators or traps [56][57][58]. Here it was shown that a zero-field splitting between high-field and low-field seeking states can suppress nonadiabatic transitions. Such a feature is present in the excited bending mode of BaOH and the other alkaline earth hydroxides [40]. Furthermore, since BaOH almost has a linear Stark shift at low fields the splitting with non-trapped states becomes large very fast compared to the quadratic Stark effect of BaF. This means that the region inside the trap were nonadiabatic can occur is much smaller and it expected that nonadiabatic transitions are suppressed for BaOH. It would be interesting to make a comparison between these two isoelectronic molecules in a traveling-wave Stark decelerator. This could for example be used to identify potential loss mechanisms.

3.3 Conclusion

By diagonalizing the full Hamiltonian the Stark effect of BaOH has been investigated in the context of an eEDM experiment and traveling-wave Stark deceleration.

This molecule is fully polarized in an electric field of 1500V/cm. The suppression of radial magnetic fields due to the tensor Stark shift is similar to molecules such as BaF or YbF and the exact nature depends the hyperfine constants which are not yet known for BaOH.

Because of the smaller dipole moment the electronic and vibrational ground state is not very attractive for traveling-wave Stark deceleration. However, because of the different Stark effect the first two rotational levels in the first excited bending mode have a large enough Stark shift at a field that can be made inside the decelerator. Furthermore, because of the different Stark effect and zero-field rotational structure of this state nonadiabatic transitions are expected to be suppressed for this molecule inside a traveling-wave decelerator.

Chapter 4

Simulating Traveling-Wave Deceleration of BaOH

To quantify how efficient BaOH can be decelerated in the ${}^2\Sigma^+_{\frac{1}{2}}(01^10)$ state numerical simulations are performed. The simulation has been previously developed within the cold molecules group and produces results that are in agreement with the experimental results [55]. Where appropriate a direct comparison to the isoelectronic molecule BaF will be made. A detailed description of the simulation can be found in [55][59][60]. The input parameters for a specific molecule in the simulation are its mass and the Stark curve. In the simulation the Stark curves are approximated as an 12th order polynomial. Such a polynomial is fitted to the Stark curves of BaOH and added to the simulation. We will in particular focus on deceleration in the $|1,-1,1\rangle$ state of BaOH, since this is also the state most suited for an eEDM measurement. However, we will also calculate the efficiency for the $|2,1,1\rangle$ and $|2,1,2\rangle$ states and look at other molecules.

For BaOH and BaF the simulations are performed at a voltage amplitude of 10kV, since this is the projected voltage amplitude in the eEDM experiment [9]. In these simulations conditions of a supersonic source (initial velocities and initial distributions if necessary) are used and a decelerator length of 4.5m is assumed. The deceleration strength to decelerate a molecular beam from 180m/s to 30 m/s is 3.5km/s^2 (these are the initial conditions of a cryogenic beam). For a 'single' run (one voltage amplitude, one deceleration strength) usually $3{\cdot}10^5$ molecules are used.

4.1 Results and Discussion

4.1.1 Time of Flight Profile

The only experimental observable for the traveling-wave Stark decelerator is the time of flight profile. The time of flight profile shows the arrival times of the molecules after the decelerator with respect to the ablation pulse, which is the moment that the molecules are

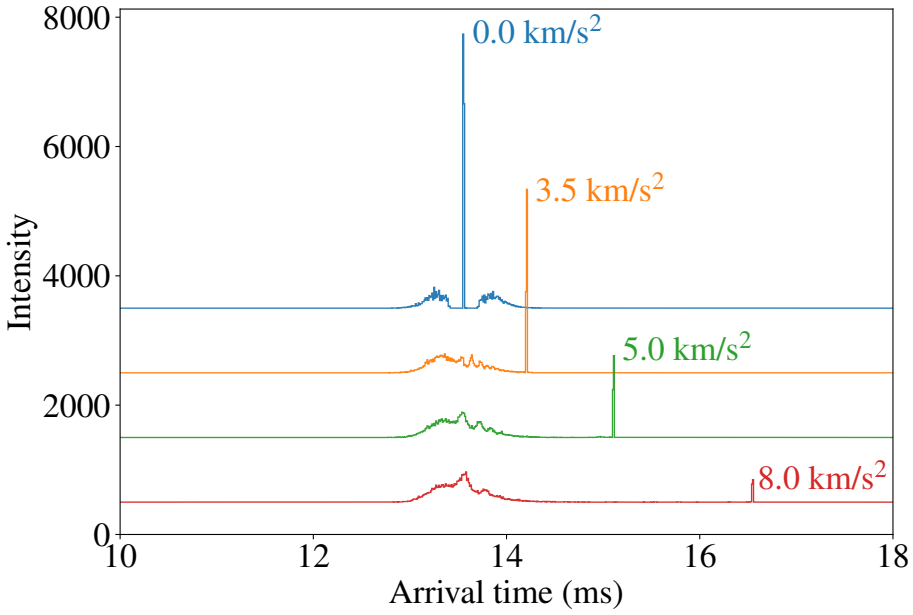

Figure 4.1: Simulated time of flight profiles for BaOH$|1,-1,1\rangle$ for different deceleration strengths at a voltage amplitude of 10kV. Initial velocity is 350 m/s.

created. These time of flight profiles can be made with the simulation. Figure 4.1 shows the time of flight profiles for BaOH$|1,-1,1\rangle$ for a number of deceleration strengths at a voltage amplitude of 10kV.

4.1.2 Acceptance

To determine how well a molecule can be decelerated in the decelerator we need to determine the acceptance. The acceptance for a particular molecule in the decelerator depends on parameters, such as the mass, the Stark curves, the applied voltages to the electrodes and the deceleration strength. The phase-space acceptance is the volume in phase-space of molecules that are accepted by the decelerator. This number describes how well molecules can be decelerated by the decelerator. Comparing this number for different molecules allows us to compare the deceleration efficiency for different molecules and states.

As a first estimate we draw the longitudinal seperatrix for BaOH $|1,-1,1\rangle$ and BaF $|2,0\rangle$ at the expected maximum voltage amplitude applied to the electrodes at 10kV [9] for different deceleration strengths. A seperatrix gives the boundary in phase-space of molecules that are accepted by the decelerator. For the longitudinal direction these are shown in figure 4.2. The area is smaller for BaOH than for BaF, which is also expected when looking at the Stark curves.

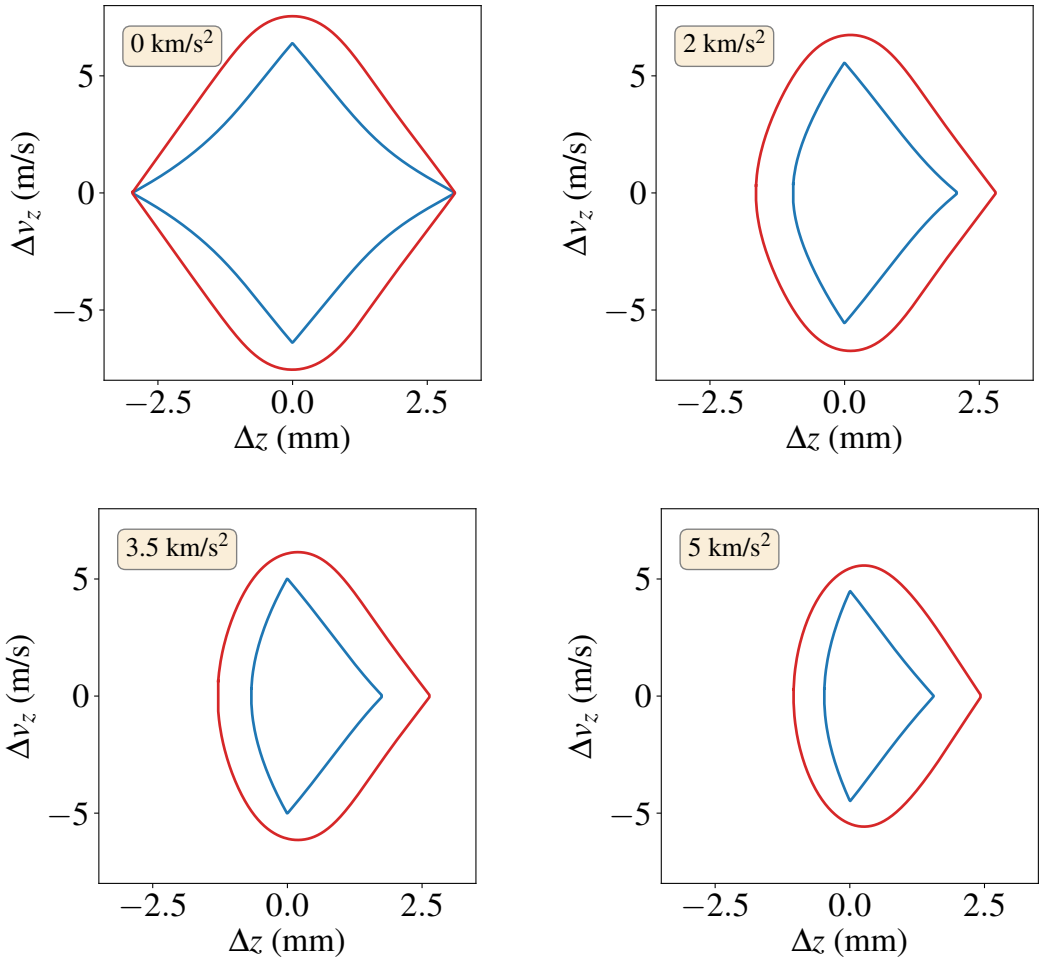

Figure 4.2: Longitudinal 1D separatrices of BaOH $|1,-1,1\rangle$ (blue) and BaF $|2,0\rangle$ (red) for different deceleration strengths at a voltage amplitude of 10KV.

These seperatrices describe an ideal case, where the longitudinal motion of the molecules is completely decoupled from the transverse motion. In reality these motions are coupled and this can lead to losses in the deceleration process. Figure 4.3 shows the distribution of BaOH molecules inside the decelerator in a full 3D simulation. During deceleration the seperatrix is almost uniformly filled. However, during guiding there seems to be a loss of molecules near the edges of the seperatrix. To account for this loss we calculate the 3D phase-space acceptance, taking into account the 3 spatial dimensions. This corresponds to a volume in 6D phase-space (3-position and 3-velocity coordinates. This is calculated using a Monte-Carlo algorithm [55]. Figure 4.5 shows the 3D phase-space acceptance as a function of deceleration strength for BaF $|2,0\rangle$ and BaOH $|1,-1,1\rangle$, BaOH $|2,1,1\rangle$ and BaOH$|2,1,2\rangle$. From this we see that the $|1,-1,1\rangle$ state of BaOH is most suited for deceleration at a voltage amplitude of 10kV. However, the low-field seeking states of N = 2 have a similar acceptance in the deceleration range 0-4km/s^2. As a comparison the phase-space acceptance for the $|1,0\rangle$ state of BaOH in the electronic and vibrational ground state is also shown. Note that the overall acceptance in the vibrational excited bending mode indeed larger is. The 3D phase-space acceptance for BaOH $|1,-1,1\rangle$ is approximately a factor 3 lower in the range 0 - 4 km/s^2 than for BaF $|2,0\rangle$. This means that approximately 3 times less BaOH molecules are accepted by the decelerator than BaF molecules if the initial distribution of molecules is larger than the acceptance of the decelerator. Although the acceptance is smaller than for BaF, it is similar to SrF which was successfully decelerated [55]. It is also important to point out that this simulation does not take all effects into account, such as nonadiabatic transitions or imperfections in the waveforms. Since the Stark effect is different for these molecules, the results of the these effects are expected to be different. It is expected that any losses because of these effects are suppressed for BaOH.

Figure 4.4 shows the 3D phase-space acceptance of BaOH for different deceleration strengths at different voltage amplitudes. The optimum voltage amplitude is indeed at 10kV. For a deceleration strength between 0 - 4 km/s^2, which is the deceleration necessary to decelerate from a cryogenic source, the acceptance remains similar for voltage amplitudes larger than 7kV. This means that BaOH can also be decelerated with similar efficiencies at lower voltage amplitudes which are experimentally easier to make.

As mentioned before, in the spectroscopic constants section, it is assumed that the dipole moment of the first excited bending vibration is the same as the dipole moment of the electronic and vibrational ground state. If we look at other triatomic molecules in bending vibrations, for example HCN, we see that the dipole moments of the electronic and vibrational ground state and first excited bending vibration are approximately the same [61]. If this dipole moment is much smaller this has consequences for Stark deceleration. The dipole moment does not determine the height of the Stark-curve which is determined by the rotational constant. However, it does determines which field is necessary to reach the turning point of the Stark curve. If the field needed to reach the turning point becomes higher than can be made in the decelerator, the acceptance for this molecule will be reduced. However, we have seen that the acceptance in the range 0 - 4 km/s^2 is the same

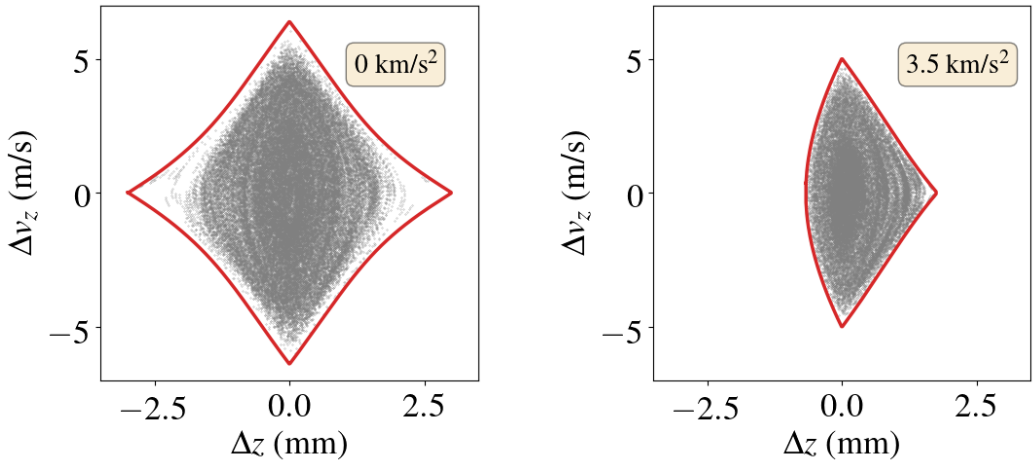

Figure 4.3: Longitudinal separatrices of BaOH and simulated phase-space distribution in the middle of the decelerator. Voltage amplitude is 10kV.

for 10kV as for 7kV. If the dipole moment turns out to be smaller, it should be possible to increase the voltage amplitude up to 10kV and obtain a similar acceptance.

4.1.3 Other Molecules

Other alkaline earth (like) hydroxides also have promise for Stark deceleration in the excited bending mode. YbOH and SrOH are examples of such molecules of which the isoelectronic SrF [62] and YbF [63] have been decelerated in a traveling-wave Stark decelerator. The results here are for the $|1, -1, 1\rangle$ rotational level.

Because of its smaller mass, larger dipole moment and rotational constant SrOH can be efficiently decelerated at a lower voltage amplitudes. Figure 4.6 shows a comparison of the phase-space acceptance for SrF and SrOH at 5kV. Note that the acceptance for SrOH is higher than for SrF.

YbOH is interesting because just as BaOH, it has a high sensitivity for physics beyond the standard model. The acceptance of these 3 molecules as a function of deceleration strength is plotted in figure 4.7 at 10kV voltage amplitude. Although YbOH is heavier than BaOH it has a larger dipole moment and larger rotational constant. Therefore, this molecule has a larger Stark shift and deceleration efficiency is similar. Notice that the overall acceptance of SrOH is much higher, because SrOH is lighter, it has a larger molecular dipole moment and larger rotational constant than BaOH.

Molecular constants are used from [64][65][40]. More details about these molecules can be found in appendix B and appendix C.

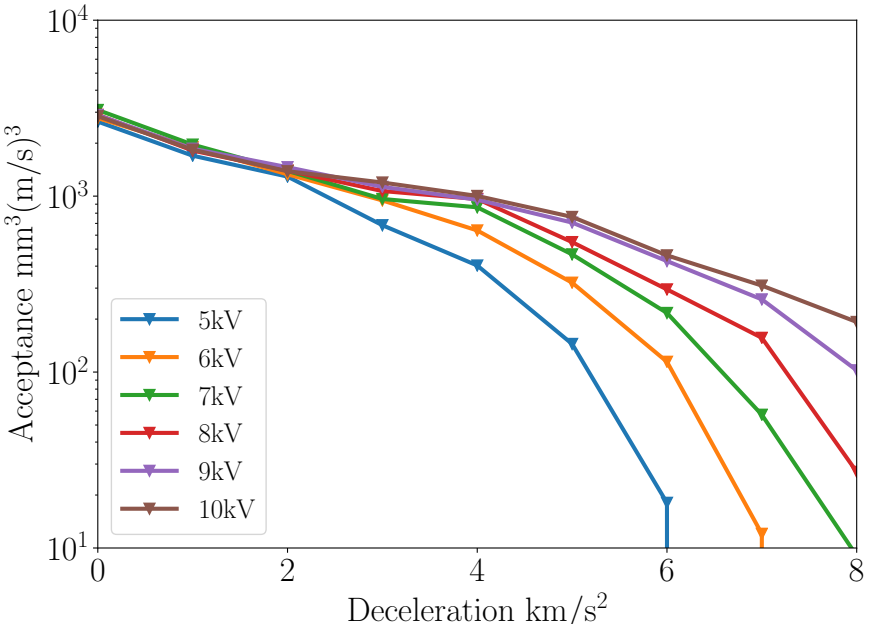

Figure 4.4: Full 3D phase-space acceptance as a function of deceleration for BaOH$|1,-1,1\rangle$ for different voltage amplitudes.

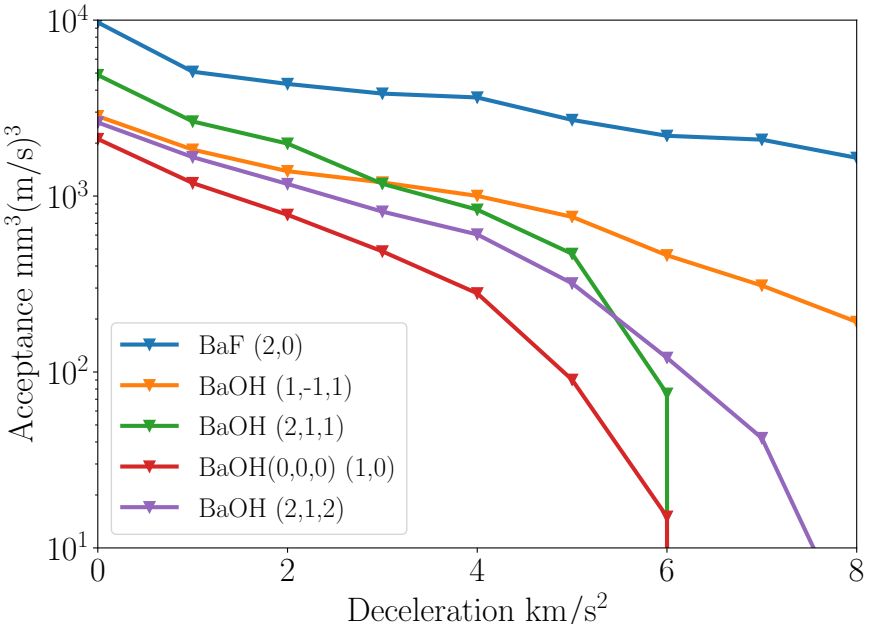

Figure 4.5: 3D phase-acceptance as a function of deceleration for BaOH$|1,-1,1\rangle$, BaOH$|2,1,1\rangle$, BaOH$|2,1,2\rangle$, BaF$|2,0\rangle$ and for the BaOH$|1,0\rangle$(in the electronic and vibrational ground state) at a voltage amplitude of 10kV.

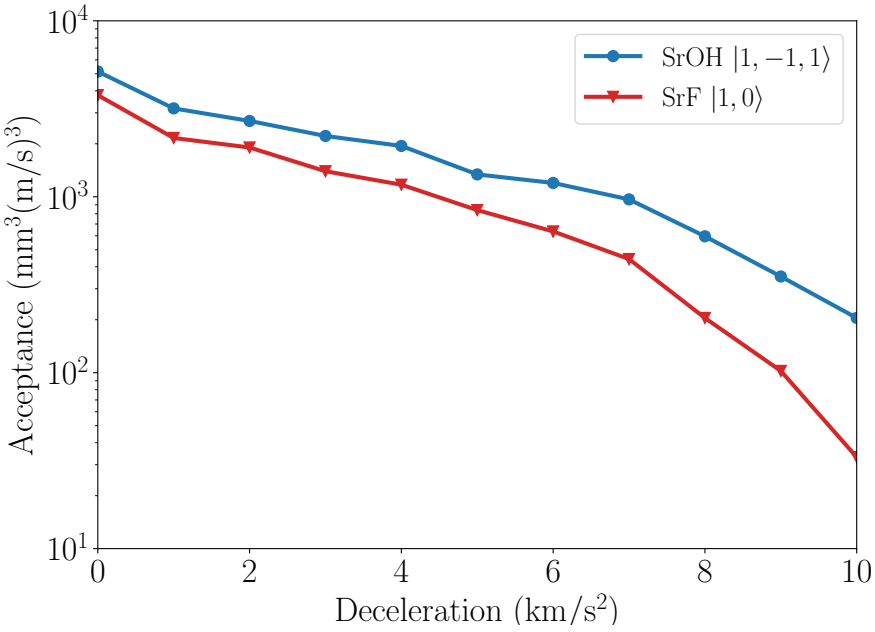

Figure 4.6: 3D phase-space acceptance as a function of deceleration for SrOH$|1,-1,1\rangle$ and SrF$|1,0\rangle$ at a voltage amplitude of 5kV.

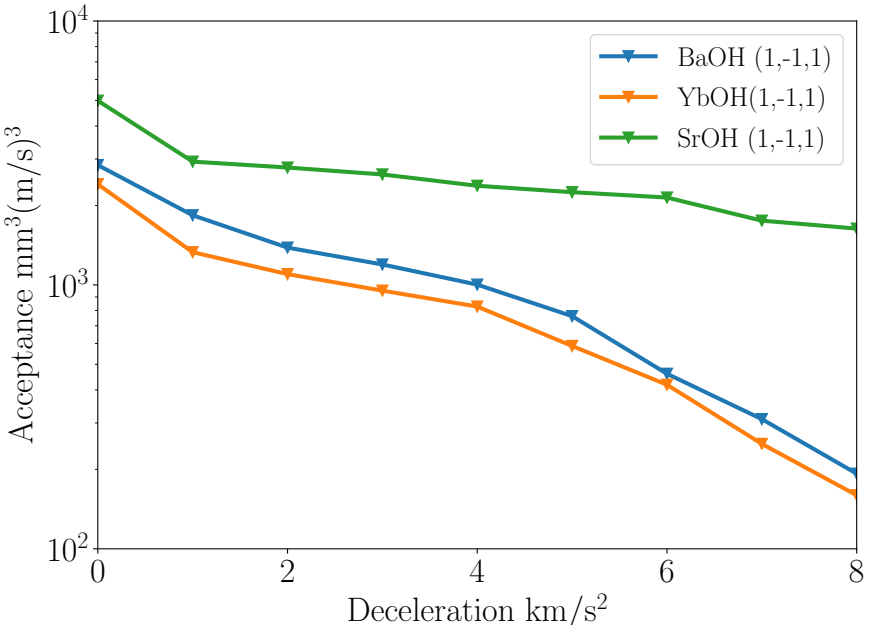

Figure 4.7: Full 3D phase-space acceptance as a function of deceleration strength for BaOH, YbOH and SrOH at a voltage amplitude of 10kV.

4.2 Conclusion

Using numerical trajectory simulations the efficiency for traveling-wave deceleration of BaOH in the first excited bending vibration was determined and compared to the isolelectronic molecule BaF. At a voltage amplitude of 10kV the 3D phase-space acceptance is approximately a factor 3 lower compared to BaF $|2,0\rangle$. Although the acceptance is lower than for BaF, the overall acceptance is still high and efficient deceleration from a cryogenic source should be possible.

What is also beneficial about BaOH is that the acceptance remains the same for voltage amplitudes larger than 7kV within the deceleration range needed to decelerate a beam from a cryogenic source. These lower voltage amplitudes are experimentally easier to make. Furthermore, BaOH has a different Stark effect than BaF which is expected to suppress nonadiabatic transitions, which has not been taken into account in the simulation.

In the end the total number of molecules at the end of the decelerator is important, which depends on many factors, such as: how many molecules can be produced in a cryogenic source, the fraction of low-field seeking states, the efficiency of a guide and the efficiency of a potential state transfer. All of which can change the total number of molecules significantly.

Traveling-wave Stark deceleration for other alkaline earth (like) hydroxides SrOH and YbOH also has been investigated. Both have promise for deceleration. In particular SrOH is promising because it has a larger acceptance than the isoelectronic SrF at a voltage amplitude of 5kV.

Chapter 5

Producing a Cryogenic Beam of BaOH

In this chapter we will discuss the production of a cryogenic beam of BaOH. The experimental work has been done at the Vrije Universiteit in Amsterdam. The first step is to build the absorption spectroscopy setup and measure the absorption of resonant laser light by BaF molecules. This is done such that absorption spectroscopy setup can be tested and a comparison to BaOH can be made. The goal of the BaF absorption measurements is not to fully characterize the beam. The settings of the source are thus not necessarily chosen for the best beam.

5.1 Setup

A good review on cryogenic sources is [66]. In this source the buffer gas is neon at 20K. BaF molecules are created by ablating a rotating barium metal target in the presence of sulfide hexafluoride (SF_6). The design of this source is similar to [67]. The neon flow into the cell is, unless stated otherwise, 15SCCM.

BaOH has never been produced in a cryogenic source, so the optimal production path is still unknown. Two different approaches are investigated: ablation of a barium target in the presence of a suitable chemical reactant or the ablation of a solid precursor target.

BaOH has been produced in ovens and supersonic sources from a reaction of barium atoms and a reactant. Three types of reactants have been used:
water [46][45][34][43][47], hydrogen peroxide [48][44][41][26][40] and methanol [42]. Methanol was also used to produce YbOH [68][14], CaOH [69][16] in supersonic and cryogenic sources. From these 3 reactants we will use methanol. Methanol has the lowest freezing point ($\approx$ 180K) and the highest vapour pressure (13kPa at 293K). This ensures that enough gas

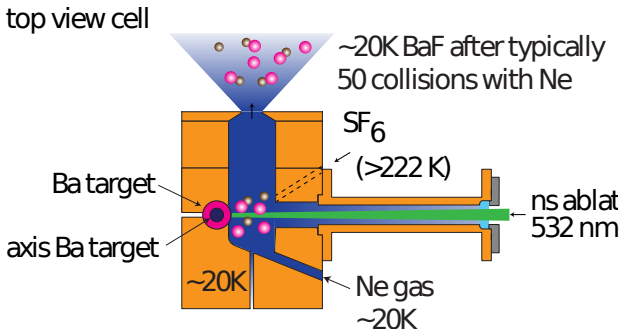

Figure 5.1: Schematic overview of the cryogenic cell [67].

phase methanol reaches the cryogenic cell. In our setup methanol enters the cell through a fill line kept at 250K. The flow of methanol is controlled with a mass flow controller which is connected to a bottle of room temperature methanol.

The other approach is the ablation of a solid precursor target. This approach has been used for other alkaline earth(like) hydroxides SrOH[15] and YbOH [70]. For BaOH a suitable precursor is barium dihydroxide $Ba(OH)_2$. The targets are made by mixing anhydrous $Ba(OH)_2$ (Alfa Aesar 12195.18) powder with a few percent Boron for stability. This mixture is subsequently pressed into a target.

We measure the absorption of atoms/molecules by sending a resonant laser through the molecular beam and measuring the decrease in power when the molecular beam passes. A schematic overview of the experimental setup used for absorption spectroscopy is given in figure 5.2. The laser light is generated by a Titanium Sapphire laser (Coherent 899). The details about this laser system can be found in [71]. This laser spans a frequency range from 780nm to 920nm. Part of the light is send through an optical fiber to a wavelength meter (Atos LM-007). All measured frequencies shown are from this device. Another part of the light is coupled into another optical fiber and send to the absorption spectroscopy setup. After the light exits the fiber it is split into 2 beams. Both beams pas a half-wave plate for light power control and a cubic polarizing beamsplitter. One beam is directly incident on one detector of a balanced photodiode (Thorlabs PDB210A/M). The other beam is send through the cryogenic source ∼5mm after the opening of the cell. After the laser beam exits the cryogenic source it passes a quarter-wave plate and is reflected back through the cryogenic source. Because the polarization of the incident linear polarized light has been rotated by 90 degrees, it is reflected by the cubic polarizing beamsplitter and incident on the other detector of the balanced photodiode. All channels of the photodiode are read out with a digital oscilloscope. The photodiode has an RF-channel which gives a voltage proportional to the difference in current between the two diodes. By using a balanced photodiode fluctuations in laserpower can be cancelled out. The typical laser power of the absorption laser probe is 5-10 µW.

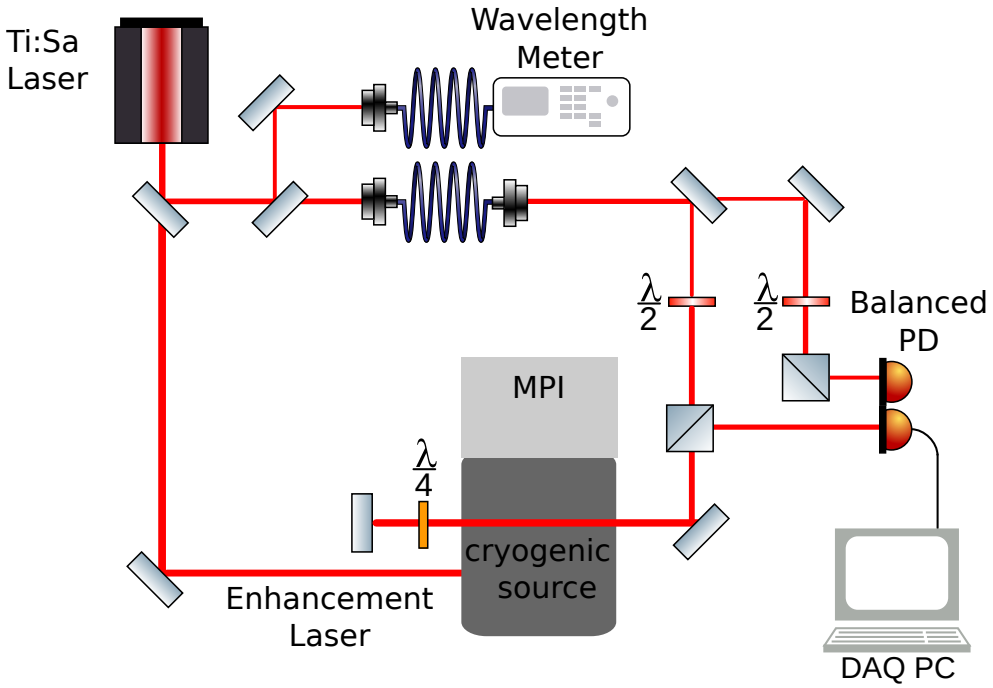

Figure 5.2: Schematic (simplified) overview of absorption setup. Only key elements are shown.

There is also a multi-photon ionization detection system present (MPI). This can be used to determine the masses of the particles in the beam. This works by ionizing the particles in the molecular beam, these particles are substantially accelerated in an electric field. From the arrival times at the detector the masses of the particles in the beam can be determined.

Another part of the laser beam is send into the cell through the ablation laser window to study the effect of exciting the barium atoms in the cell. This is also shown in figure 5.2.

5.2 Results and Discussion

5.2.1 BaF Absorption Spectroscopy

The first step is to do absorption spectroscopy on BaF. The absorption is given by Beer's law. If most of the molecules remain in the ground state, Beer's law is given by [24]:

$$\frac{I}{I_0} = e^{-\sigma l_s N_0} = e^{-\kappa(\omega) l_s} \tag{5.1}$$

$$\Rightarrow \ln \frac{I}{I_0} = -\sigma l_s N_0, \tag{5.2}$$

where I_0 is the intensity of the ingoing light, I the intensity of the outgoing light. N_0 is the density of the absorbing medium(in our case the molecules), l_s is the length the light travels through the medium and σ is the absorption cross section. $\kappa(\omega)$ is the absorption coefficient. For small absorption the following holds(since $\ln x \approx x - 1$ if x$\approx$ 1):

$$\frac{I - I_0}{I_0} = -\sigma l_s N_0 \tag{5.3}$$

In this chapter molecular transitions are labeled by spectroscopic notation as used in molecular spectra simulation program PGOPHER [50]: ${}^{\Delta N}\Delta J(J')_{a,b}$ where the change in angular momentum is given by the letter P, Q or R for a change of -1, 0, 1. The letter a represent the parity sub-level of the excited state. The letter b represent the fine structure component of the ground state.

Using known molecular spectroscopy of BaF [72], absorption was almost immediately observed on the $X^2\Sigma^+_{\frac{1}{2}}(v=0) - A^2\Pi_{\frac{3}{2}}(v=0)$ transition at 816nm. Figure 5.3 shows the peak absorption when scanning the frequency around the ${}^{Q}Q_2(4.5)$ transition. The absorption shown is the measured absorption, directly from the diode on which the absorption laser in incident, thus when the laser passes the molecular beam 2 time averaged over 10 shots. The shape of the absorption trace is determined by the longitudinal velocity distribution of the molecular beam and the length of the pulse.

Since the absorption laser crosses the molecular beam orthogonal to the beam direction, we are sensitive to the transverse velocity component of the molecular beam. Doppler broadening gives the largest contribution to the linewidth of the transition. From the integrated absorption trace as a function of frequency the Doppler width and subsequently the temperature can be determined. The integral/average of such a trace should be approximately proportional to the total molecule number with a particular velocity (for small absorption). Since Doppler broadening is the dominant broadening mechanism we can fit a Gaussian function to determine the Doppler full width half maximum(FWHM) $\Delta\nu_{Doppler}$ (similar to [73]):

$$g_D(\omega) = Ae^{-4\ln 2\frac{(\nu-\nu_0)^2}{\Delta\nu^2_{Doppler}}} \tag{5.4}$$

We fit such a function to each spin-rotation component. However, since there is also a hyperfine structure which can not be resolved because of Doppler broadening, the fitted profiles have a larger FWHM than in reality and the results from the fits below should be considered an upper limit. The translational temperature is related to $\nu_{Doppler}$ by:

$$\Delta\nu_{Doppler} = \frac{1}{\lambda}\sqrt{\frac{8k_bT\log 2}{m}} \tag{5.5}$$

Figure 5.3 shows the integrated absorption trace as a function of frequency. This is the absorption trace of the RF-channel of the photodiode. To each fine structure component

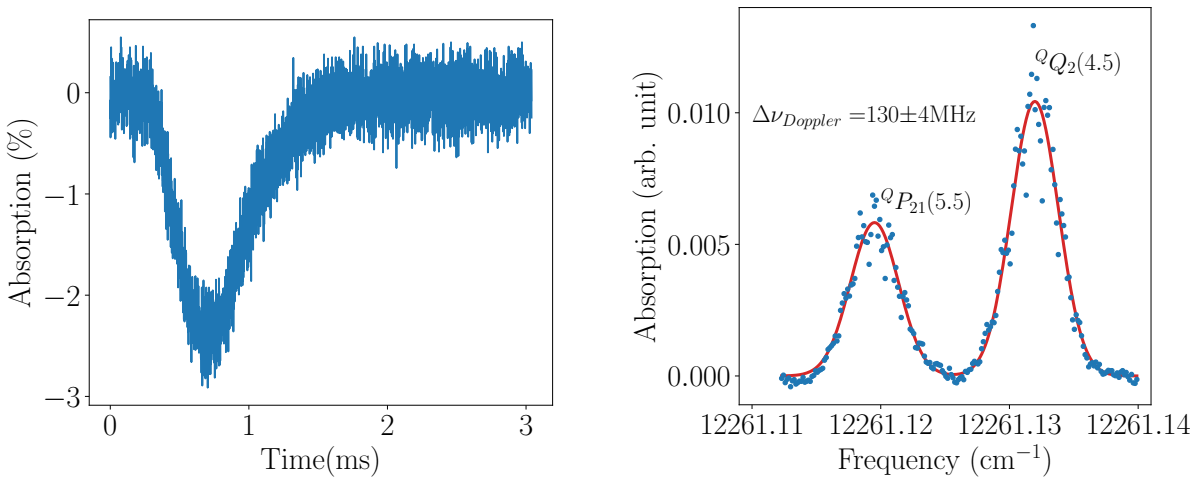

Figure 5.3: Left: absorption trace for the $^{Q}Q_2(4.5)$ transition of the $X^2\Sigma^+_{\frac{1}{2}}(v = 0) - A^2\Pi_{\frac{3}{2}}(v = 0)$ transition of BaF. Right: integrated absorption trace as a function of frequency of the $^{Q}Q_2(4.5)$ and $^{Q}P_{21}(5.5)$ $X^2\Sigma^+_{\frac{1}{2}}(v = 0) - A^2\Pi_{\frac{3}{2}}(v = 0)$ transitions of BaF. Two Doppler profiles are fitted to the data. The results of the fit to the $^{Q}Q_2(4.5)$ line are given in the figure.

the above line profile is fitted (red line). A FWHM of $\nu_{Doppler} = 130$MHz corresponds to a temperature of 38K. Around a molecular resonance a large fluctuation of signal is visible. This is caused by different ablation yields as the target rotates.

We could also observe the $X^2\Sigma^+_{\frac{1}{2}}(v = 0) - A^2\Pi_{\frac{1}{2}}(v = 0)$ transitions of BaF at 860nm. This electronic transition will be used for lasercooling. Figure 5.4 shows a number of $\Delta N = 0$ transitions.

A relevant quantity is the fraction of molecules in an excited vibrational state. For BaF this is not critical to know, but for BaOH the state most suited for an eEDM measurement and Stark deceleration is an excited bending vibration. It is therefore interesting to see if this state is populated after buffer gas cooling. BaF has a simpler vibrational structure than BaOH, but the relative population of molecules in the v = 1 state tells us qualitatively if absorption of a vibrational excited state could be measured for BaOH under the conditions of this cryogenic source.

Using known molecular spectroscopic data [74] absorption on the $X^2\Sigma^+_{\frac{1}{2}}(v = 1) - A^2\Pi_{\frac{3}{2}}(v = 1)$ was immediately observed. Figure 5.5 shows the peak absorption signal of the $^{Q}Q_2(4.5)$ transition. Figure 5.5 shows the integrated absorption as a function of frequency. Since a peak absorption of 1% can be observed there is still a sizeable fraction of molecules left in the $X^2\Sigma^+_{\frac{1}{2}}(v = 1)$ state if we compare this to the peak absorption of 2.5% of the same

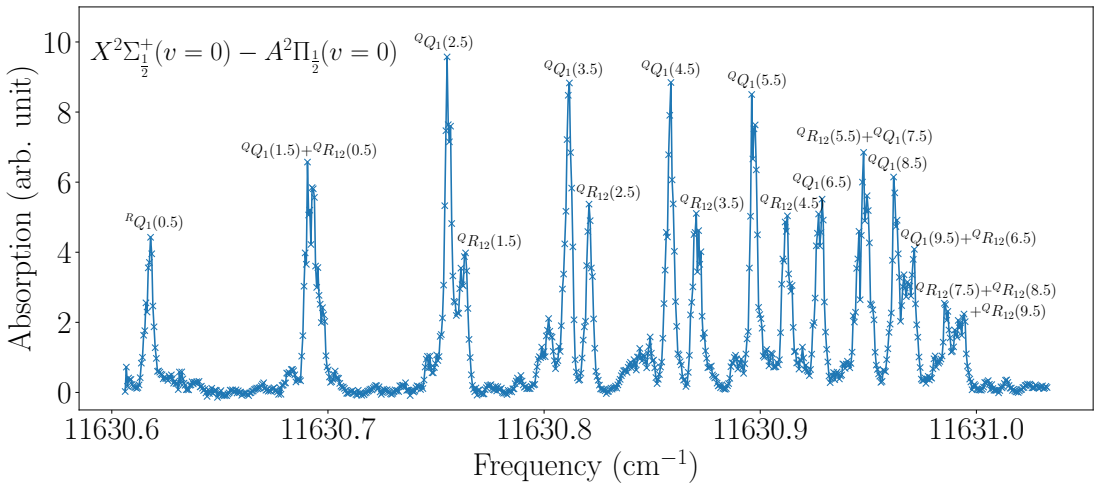

Figure 5.4: Scan of the Q-branch(ΔN = 0) of the $X^2\Sigma^+_{\frac{1}{2}} - A^2\Pi_{\frac{1}{2}}$ transition of BaF. The peaks are labeled up to J = 9.5.

transition of the vibrational ground state shown in figure 5.3. This fraction of absorption between these two vibrational states remained the same for different transitions. This result looks promising for BaOH. However, for SrOH it was observed that bending vibrations undergo rapid vibrational thermalization [73]. This could also be the case for BaOH.

Since the BaF molecules are created by ablating barium in the presence of SF_6, it is also interesting to see how many barium atoms are still left in the beam compared to barium fluoride. Figure 5.6 shows the barium peak absorption signal and integrated absorption of the $^1S_0$ - $^3P_1$ transition at 791.3 nm.

5.2.2 Estimating Number of Molecules/Atoms

The number of atoms/molecules in the beam in a particular state is given by [75]:

$$N_{mol} = \frac{A_d}{L_s}\frac{v_{beam}}{\sigma_D}\int_0^T \ln\left(\frac{P_0}{P_t}\right)dt, \tag{5.6}$$

where A_d is the cross sectional area of the beam at the distance of intersection with the absorption laser, $\frac{P_0}{P_t}$ is the ratio of incident to transmitted power and σ_D is the Doppler cross section for absorption. For a diatomic molecule the Doppler absorption cross section is [76]:

$$\sigma_D = \frac{\lambda^2}{2\pi}\frac{2J'+1}{2J+1}\frac{\gamma_p}{\gamma_{tot}}, \tag{5.7}$$

where w_0 is the frequency of the transition. J' and J are the angular momenta of the lower state and upper state respectively. γ_{tot} is the total linewidth of the transition. This

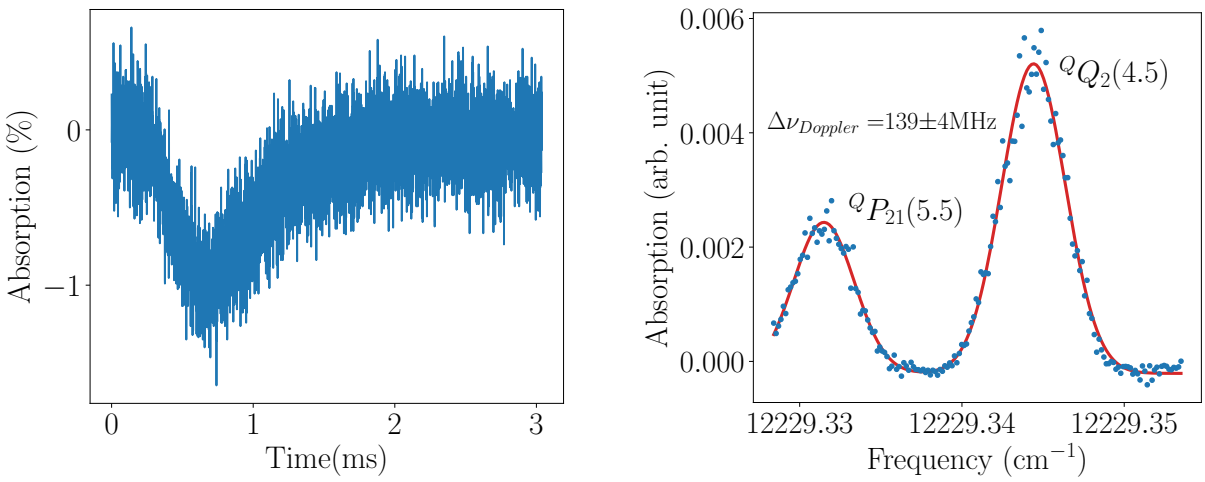

Figure 5.5: Left: Absorption trace for the $^{Q}Q_2(4.5)$ transition of the $X^2\Sigma^+_{\frac{1}{2}}(v = 1) - A^2\Pi_{\frac{3}{2}}(v = 1)$ transition of BaF. Right: Integrated absorption trace as a function of frequency of the $^{Q}Q_2(4.5)$ and $^{Q}P_{21}(5.5)$ $X^2\Sigma^+_{\frac{1}{2}}(v = 1) - A^2\Pi_{\frac{3}{2}}(v = 1)$ transitions of BaF. Two Doppler profiles are fitted to the data. The results of the fit to the $^{Q}Q_2(4.5)$ line are given in the figure.

is given by (We have assumed that Doppler broadening gives largest contribution to the linewidth and neglect any other contributions):

$$\gamma_{tot} = \frac{2\pi}{\lambda}\sqrt{\frac{8k_bT\log 2}{m}} \tag{5.8}$$

And the partial linewidth is given by:

$$\gamma_{partial} = F_{vv'}\frac{H_{e-g}}{\sum H_{e-g}}\gamma_{nat}, \tag{5.9}$$

where $F_{vv'}$ is the Franck-Condon factor of the transition, γ_{nat} is the natural linewidth of the transition and H_{e-g} is the Hönl-London factor. We will determine the population in the N = 5, J = 4.5 state from the $^{Q}Q_2(4.5)$ $X^2\Sigma^+_{\frac{1}{2}}(v = 0) - A^2\Pi_{\frac{3}{2}}(v = 0)$ transition. We chose this state because the largest absorption was observed. The lifetime is $\tau = 47.9$ns, $F_{vv'} = 0.96$ [77] [78]. The Hönl-London factor for a Q transition (J' = J) is given by[76]:

$$H_{e-g} = \frac{2J' + 1}{4} \tag{5.10}$$

And the $\sum H_{e-g}$ is given by:

$$\sum H_{e-g} = \frac{1}{2}(2J + 1) \tag{5.11}$$

Combining this gives:

$$\sigma_D = \frac{\lambda^3}{2(2\pi)^2}\sqrt{\frac{m}{8k_bT\log 2}}\frac{F_{vv'}}{\tau}\frac{H_{e-g}}{\sum H_{e-g}} \tag{5.12}$$

The Doppler fit gives us a translational temperature of T = 38K. As stated before this does not take into account the unresolved hyperfine structure. We assume that the translational degrees of freedom have completely thermalized with neon at 20K. λ = 816nm. m = 156.32u and J = J' = 4.5. This gives us the following results:

$$\sigma_D = 9.0 \times 10^{-16}\mathrm{m}^2 \tag{5.13}$$

Integrating the absorption trace gives us:

$$\int \mathrm{BaF} = 1.52 \cdot 10^{-5}s \tag{5.14}$$

Assuming that the molecular beam has a diameter of $d = 4.5$mm (the opening of the cell, a conservative estimate) and $v_{beam} = 180$m/s. This gives a surface area of $A_d = \pi(\frac{d}{2})^2$. The diameter of the laser beam is smaller than the diameter of the molecular beam: d_{laser} = 2mm. Since the laser passes the molecular beam two times this gives $L_s = 9$mm. After filling in the numbers, formula 5.6 gives the number of molecules in the N = 5 J = 4.5 state in the beam:

$$N_{mol} \approx 5 \cdot 10^9\mathrm{molecules} \tag{5.15}$$

A similar estimate can be made for for the number of barium atoms. The cross section is given by [79]:

$$\sigma_D = \frac{\lambda^2}{4}A_{12}g_D(\lambda) \tag{5.16}$$

Where $g_D(\lambda)$ is the normalized Doppler profile (formula 5.4 is not normalized). The integral of the resonant absorption trace is (given in figure 5.6):

$$\int \mathrm{Ba} = 8.7 \cdot 10^{-5}s \tag{5.17}$$

Since λ = 791.3nm, A_{12} for Ba is $2.99 \cdot 10^5$ s^{-1} [80], the cross section is:

$$\sigma_D = 5.8 \cdot 10^{-16}m^2 \tag{5.18}$$

Using the same geometrical arguments as for BaF, this gives the number of barium atoms in the beam:

$$N_{Atoms} \approx 8 \cdot 10^{10}\mathrm{atoms} \tag{5.19}$$

This calculation should be considered a rough estimate. Here we have assumed that $I_{laser} << I_{sat}$. I_{sat} (for a two level system) is given by [79]:

$$I_{sat} = \frac{\pi}{3}\frac{hc}{\lambda^3\tau} \tag{5.20}$$

Beer's law only holds if absorption is independent of laser power. The general form for the absorption coefficent is given by [79]:

$$\kappa(\omega, I) = \frac{N\sigma(\omega)}{1 + \frac{I_{laser}}{I_{sat}}} \tag{5.21}$$

Where N is the density. From this formula we see indeed that if $I_{laser} << I_{sat}$ the absorption coefficient becomes independent of laser power.

For BaF $I_{sat} \approx 0.77\text{mW/cm}^2$. We use a typical power of 10 µW and our laser beam has a radius of 1 mm. Thus, $I_{laser} = 0.32\text{mW/cm}^2$. Thus, for BaF the assumption $I_{laser} << I_{sat}$ is approximately correct (Although we probably still have to much power). For barium $I_{sat} \approx 0.030\text{mW/cm}^2$ which is a factor of ≈11 lower than I_{laser}. This has not been taken into account in equation 5.6. Thus, according to equation 5.21 the number of barium atoms is actually a factor of 12 higher. Taking this into account gives us 10^{12} barium atoms in the beam.

Assuming that the underlying hyperfine components have the same transition strength. We can estimate the number of molecules in the N = 5 state as $\approx 10^{10}$ molecules. Although this is not the N = 2 state, the state most suited for Stark deceleration, from figure 5.4 we see that transitions involving the N = 2 and N = 5 ground state levels have similar strengths. Which means that the population should be similar. 10^{10} is approximately what is needed for the BaF eEDM experiment [9]. However, the source is not optimized (coldest source, ablation power, best target). This can still change the yield by several factors.

5.2.3 Production of BaOH

The first attempt to produce BaOH in a cryogenic source was done by ablating barium in the presence of methanol. Although BaOH has been previously produced in a supersonic source with this method [42]. No clear reproducible absorption signal was observed. Since there are different molecules that can be potentially produced with the approximately same mass such as BaO, BaF(if there is still SF_6 left) or $BaCH_3$ the ion signal from the MPI detection could not be used to identify BaOH. The fact that no BaOH from a reaction of barium and methanol was observed is consistent with earlier studies [81]. Here it is stated that the main reaction product is $BaOCH_3$ and that no BaOH was observed although energetically allowed. Interestingly, since this molecule is also isoelectronic to BaF, it should be sensitive for physics beyond the standard model and have prospects for laser cooling. It would be interesting to check if this molecule is present in the beam. Unfortunately, only low resolution work is known for this molecule [82] [83].

Instead of methanol, water or hydrogen peroxide can be used. BaOH has been produced in supersonic sources and ovens with these reactants. However, the relatively high freezing points and low vapor pressures makes it more experimental challenging to introduce these

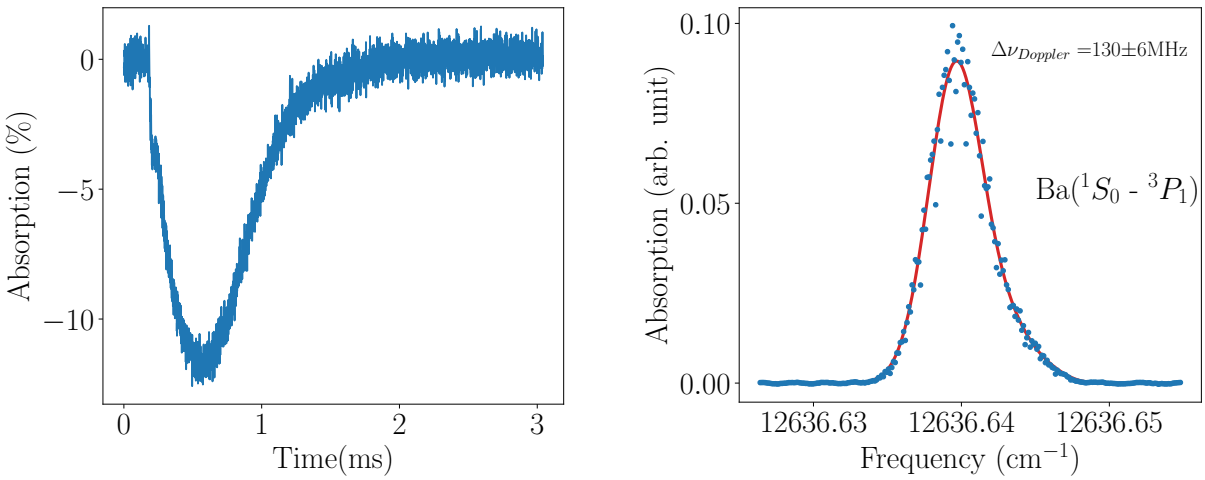

Figure 5.6: Left: Resonant absorption trace for $^1S_0$ - $^3P_1$ transition of barium. The small peak at t = ≈ 0.25 ms most likely correspond to hot barium atoms that do not thermalise with neon. Right: Integrated absorption trace as a function of frequency of the $^1S_0$ - $^1P_3$ transition of barium. Asymmetry to the right caused by isotopes of barium. Three Doppler profiles are simultaneously fitted to the data to account for the asymmetry caused by the isotopes. The results of the fit to the main profile are given in the figure.

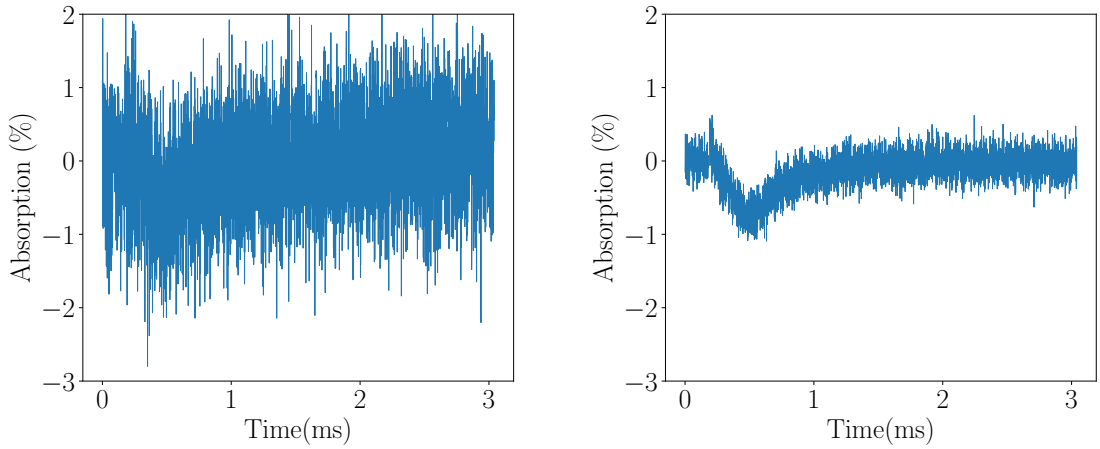

Figure 5.7: left: Observed (peak) absorption signal of BaOH (unbalanced). The peak absorption is about 0.8 %. Right: RF signal of the photodiode measured at the same time. Note the clear increase in resolution when the balanced setup is used.

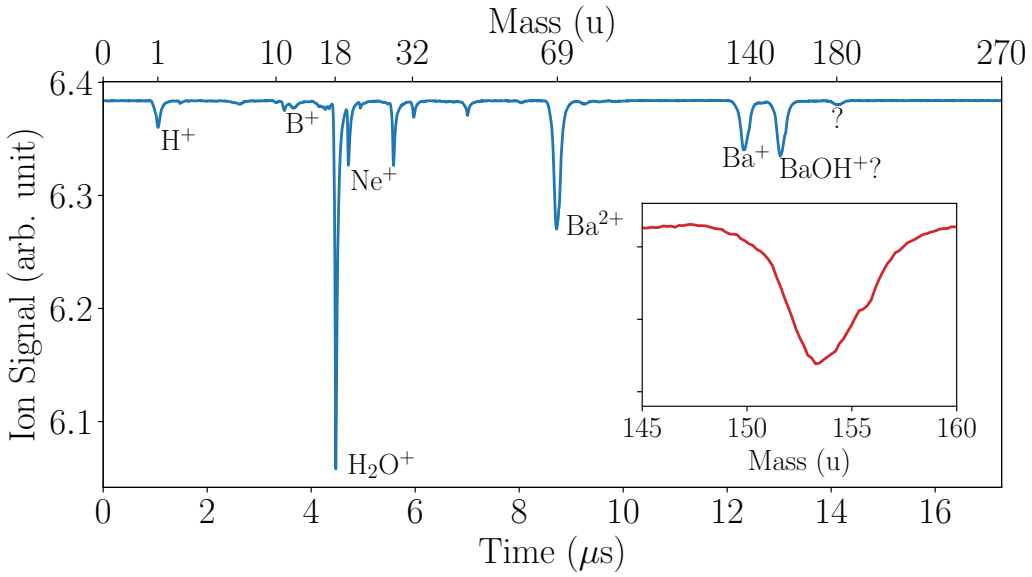

Figure 5.8: Time of flight measurement of the different ionized atoms and molecules in the molecular beam. The masses are calculated from the arrival times. The inset shows the signal around the mass of BaOH. The peak of this signal corresponds to a mass of 153.3u which is also the mass of barium oxide. However, since the mass increases quadratic with the arrival times the uncertainty in mass also increases quadratically.

reactants in the cryogenic cell.

Next an attempt was made to make BaOH by ablating $Ba(OH)_2$. Using this approach a clear absorption signal was observed around the frequency of the ${}^RQ_{21}(3.5)$ and ${}^RR_2(2.5)$ $\tilde{X}^2\Sigma^+_{\frac{1}{2}} - \tilde{A}^2\Pi_{\frac{3}{2}}$ transitions of BaOH at 831nm. This is shown in figure 5.7. Unfortunately the target degraded quickly, producing inconsistent ablation yields, so no real absorption spectroscopy could be done. The peak absorption observed was about 0.8%, approximately a factor 3 lower than for BaF. Figure 5.9 shows a frequency scan around the ${}^RQ_{21}(3.5)$ and ${}^RR_2(2.5)$ transitions of BaOH.

Figure 5.8 shows the mass spectrum of the atoms/molecules in the beam. A peak with a mass around 154u was observed. No positive identification could be made, because there are different reaction products with the same mass, such as barium oxide. It is still not clear if or how efficiently BaOH can be detected or if it dissociates by the ionization laser.

Although a $Ba(OH)_2$ target was used (not a barium metal target), there was still a large barium absorption signal measured. The resonant barium absorption trace is shown in figure 5.11. The barium peak absorption signal is similar to when we are ablating the metal target. However, the signal is noisier than when ablating a barium metal target, which is most likely caused by averaging over the inconsistent ablation yields. Furthermore, there

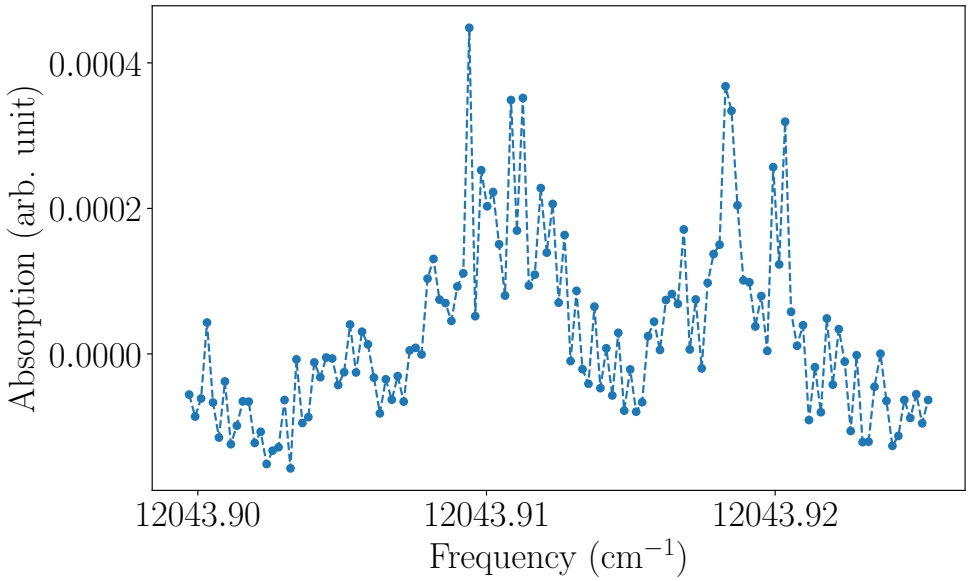

Figure 5.9: Integrated absorption as a function of frequency around the observed transition of BaOH. The two peaks most likely correspond to the two different spin-rotation components: ${}^{R}Q_{21}(3.5)$ and ${}^{R}R_{2}(2.5)$.

seems to be a very fast component in the barium absorption signal.

Upon optimization of the target it should be possible to obtain a similar yield of BaOH as for BaF. This was also previously observed for SrOH [84]. SrF_2 targets could be hardened by sintering them in an oven. This approach could also be tried for the $Ba(OH)_2$ targets. The targets were made from the anhydrous salt. However, in the production process the salt was mixed with some water. In a reaction with water the monohydrate or octahydrate $Ba(OH)_2$ might have been produced. These forms have a lower melting point than the anhydrous salt (80°C vs 300 °C), which could have led to a more rapid degradation of the target, because of the heating by the ablation laser. However, if this lower melting point is not an issue, these hydrates could be used to add more reactants into the target.

5.2.4 Exciting Barium Atoms in the Cell

Recently the yield from a cryogenic YbOH source was enhanced by a factor 10 by exciting Yb atoms in the cell into a metastable state [70]. Similar techniques have been used to enhance the production of BaOH from a Broida-type oven [43]. There, barium was excited into the ${}^{3}P_1$ state, by driving the ${}^{1}S_0$ - ${}^{3}P_1$ transition. Since this is the same transition we use to measure barium absorption, we can also study the effect of exciting the barium atoms in the cell while simultaneously monitoring the absorption to check if we are on resonance and using the ion signal to see if there is an increase in molecule production. Approximately 250mW of laser light is send co-linear with the ablation laser into the cell.

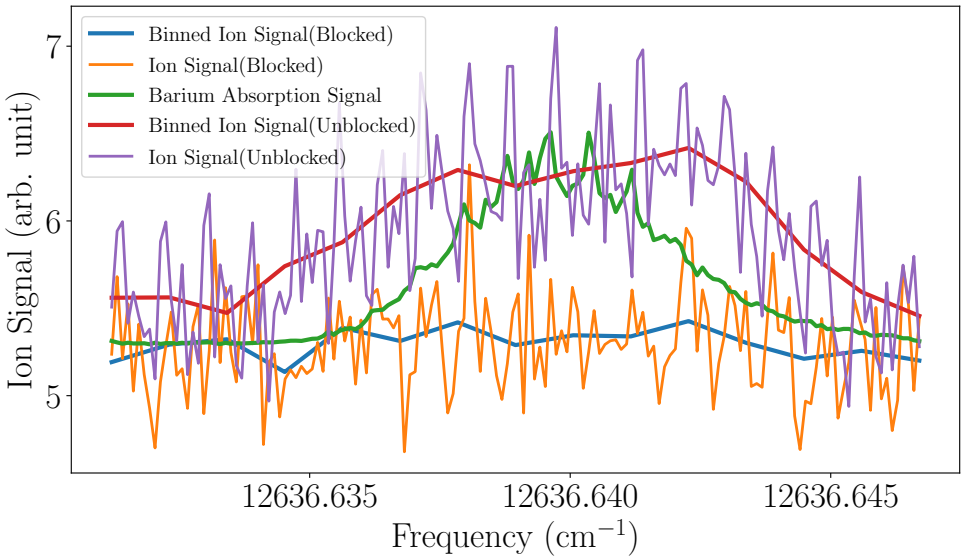

Figure 5.10: Ion signal as a function of laser frequency. When scanning the excitation laser over the barium $^1S_0$ - $^3P_1$ transition there is an increase of BaF signal. The barium absorption signal is normalized.

The $^3P_1$ state has a lifetime of 1345 ns [85].

Figure 5.10 shows the average of a number of BaF ion signal measurements as a function of excitation laser frequency with the excitation blocked and unblocked. The excitation laser was scanned over the barium resonance which is also shown in the figure. There is a clear increase of 20 % in BaF ion signal correlated to the barium atomic resonance. It is unlikely that the increase of BaF is caused by heating of the cell by the excitation laser since it is correlated to the atomic resonance. The ion signal resonance is significantly broader than the absorption signal, which could be caused by power broadening or by Doppler broadening caused by the velocity distribution at the time of ablation.

The same measurement was done with the $Ba(OH)_2$ target in place. Unfortunately, as stated before it is not clear if or how well BaOH can be detected with the ionization detection and the inconsistent yield of the target made any clear measurement from the ionization detection difficult.

When exciting the barium atoms in the cell a decrease of barium absorption signal was observed. With the barium target the absorption signal decreased by a factor 2. With the $Ba(OH)_2$ target the absorption signal disappeared completely. This is shown for BaOH in figure 5.11. It must be noted that when performing this measurement with the $Ba(OH)_2$ target the laser was better aligned into the cell. It is unlikely that all the barium reacts to form BaF/BaOH, since a large barium mass peak could still be observed from the mass resolved MPI. Most likely the barium atoms decay into the metastable $6s5d\ ^3D$ and are

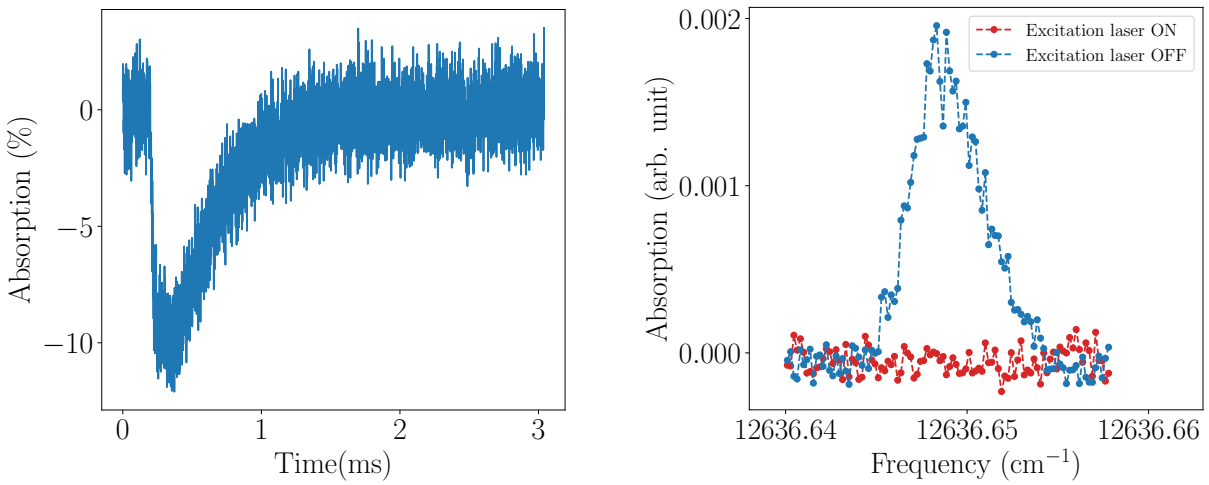

Figure 5.11: Left: barium absorption trace when ablating a $Ba(OH)_2$ target. Right: disappearance of barium intergated absorption signal when exciting the barium atoms in the cryogenic cell. Most likely the atoms are pumped into the metastable $6s5d\ ^3D$ state.

therefore out of resonance with the absorption laser [86].

The simplified reason why exciting barium (or ytterbium) atoms can enhance the production of BaOH (or YbOH) is well understood. As stated in [70] water and hydrogen peroxide are created by the ablation of $Yb(OH)_3$. It is likely that these are also created by the ablation of $Ba(OH)_2$. The reaction:

$$Ba(^1S_0) + H_2O \longrightarrow BaOH + H^+ \tag{5.22}$$

is endothermic by 12 kcal/mol [34]. Upon electronic excitation this reaction becomes exothermic. Using similar arguments it is not immediately clear why excitation of barium leads to a small increase in production of BaF. Since the reaction:

$$Ba(^1S_0) + SF_6 \longrightarrow BaF + {SF_5}^+ \tag{5.23}$$

is most likely exothermic already [87]. To see if the BaF yield can be significantly enhanced as well a more detailed study most be done into this reaction mechanism between BaF and SF_6. It is also interesting to investigate what will happen upon electronic excitation of barium when ablating a BaF_2 target, since BaF is created from a different mechanism with such a target.

Another electronic state of barium has also been used to enhance the production of BaOH [81] [47]. However, this state needs to be populated by a third level, which is out of the range of the Ti:Sa laser. It would also be interesting to see if the metastable states of barium are populated after the ablation process (If we can pump the barium atoms into

these states, then they don't seem to thermalize with neon). If these states are populated, pumping the atoms out of these metastable states could tell something about their reactivity.

Finally, according to [70] the setup used in our experiment produced the least and most inconsistent amount of enhancement. The largest enhancement was observed when the excitation laser was sent through a spectroscopy window in the cell. Unfortunately, such a window is not present in our cell, but might be worth adding to a future cell.

5.3 Conclusion

As a first step toward producing BaOH an absorption setup was build and absorption by BaF molecules has been measured. Absorption on both the $X^2\Sigma^+_{\frac{1}{2}} - A^2\Pi_{\frac{1}{2}}$ and $X^2\Sigma^+_{\frac{1}{2}} - A^2\Pi_{\frac{3}{2}}$ transitions of BaF and $^1S_0$ - $^3P_1$ transition of barium could be measured. About 10^{10} BaF molecules in the $X^2\Sigma_{\frac{1}{2}}(v = 0)$ N = 5 rotational level and 10^{12} barium atoms in the $^1S_0$ ground state were measured in the beam. A significant fraction of the molecules was in the $X^2\Sigma_{\frac{1}{2}}(v = 1)$ state, which shows qualitatively that the first excited bending vibration of BaOH might be populated after buffer gas cooling.

The first attempt to produce BaOH in a cryogenic source was done by ablating barium in the presence of methanol. Unfortunately, no BaOH absorption signal was observed although this method was previously used in a supersonic source. The second attempt was done by ablating the solid precursor $Ba(OH)_2$. Using this approach absorption on the $\tilde{X}^2\Sigma^+_{\frac{1}{2}} - \tilde{A}^2\Pi_{\frac{3}{2}}$ transition of BaOH was measured and a cryogenic beam of BaOH has been made. Although this was a different target, there was still a large barium absorption signal measured. Upon optimization of the target a similar molecular yield as observed for BaF should be possible.

The effect of exciting the barium atoms in the cryogenic cell was also studied. Upon driving the $^1S_0$ - $^3P_1$ transition of barium an increase of 20% in BaF ion signal was measured. A more detailed investigating should be done to see if this can be increased. For BaOH no clear ion signal could be measured, however this enhancement should work as it has been used for BaOH in the past.

Chapter 6

Summary

The electron EDM is an important probe for physics beyond the standard model. Currently, the best limits on the eEDM are placed with diatomic molecules. However, it was recently shown that polyatomic molecules offer several benefits. In this thesis it was investigated if the triatomic molecule BaOH can be made in a cryogenic source and simulated if this molecule can be decelerated in a traveling-wave Stark decelerator.

By calculating the Stark effect for different vibrational states it was found that the electronic and vibrational ground state is not attractive for Stark deceleration, because of the small molecular dipole moment. However, the first excited bending vibration has a different Stark effect and efficient Stark deceleration should be possible in the first two rotational levels of this state. This state also has the advantage that there are large zero-field splittings between trapped and non-trapped states, which is expected to suppress nonadiabatic transitions.

The next step was to perform numerical trajectory simulations of the deceleration process for this molecule. The simulated 3D phase-space acceptance at a voltage amplitude of 10kV is similar to SrF at 5kV, which was successfully decelerated. However, the 3D phase-space acceptance is a factor 3 lower than for the isoelectronic BaF molecule, which means that approximately a factor 3 less molecules can be decelerated. It should be noted that the simulation does not take into account effects such as nonadiabatic transitions, which are expected to be suppressed for BaOH. Other alkaline earth (like) hydroxides such as YbOH and SrOH also have promise for Stark deceleration. In particular SrOH, for which the 3D phase-space acceptance is higher than for the isoelectronic SrF.

Finally, an attempt was done to make BaOH in a cryogenic source. First, the absorption setup was build and absorption was measured on BaF, to test the setup and such that a comparison to BaOH can be made. Absorption on the $X^2\Sigma_{\frac{1}{2}} - A^2\Pi_{\frac{1}{2}}$ and $X^2\Sigma_{\frac{1}{2}} - A^2\Pi_{\frac{3}{2}}$ transitions was immediately observed. It is also found that a large fraction of molecules are in the first excited vibrational state. There was also a large barium absorption signal measured. The first attempt to make BaOH was done by ablating barium in the presence

of methanol, but no absorption signal was observed. Next, it was tried to make BaOH by ablating a pressed $Ba(OH)_2$ target. Using this method an absorption signal was observed. Unfortunately, the target degraded quickly producing inconsistent ablation yields. Upon optimization of the target similar yields as for BaF should be possible. The effect of exciting the barium atoms into a metastable state was also investigated. This was recently done for YbOH molecules and increased the number of molecules from the source by a factor 10. For BaF an increase in ion signal of 20% was measured. This means that there are 20% more molecules produced. A more detailed investigation should be done if this production can be increased further. This was also tried for BaOH, but no clear increase in ion signal was observed. However, this method has been used for BaOH in the past and similar enhancements as for YbOH are thus expected.

It was demonstrated that the triatomic molecule BaOH can be made in a cryogenic source and simulations show that this molecule has promise for traveling-wave Stark deceleration. This combination allows to decelerate a large number of BaOH molecules with similar efficiency as the isoelectronic BaF molecule. However, the real advantage of BaOH over diatomic molecules, such as BaF, is the combination of lasercooling with full polarization and internal co-magnetometer states. In the appendix an estimate for the Franck-Condon factors is given. This is only an estimate, but the Franck-Condon factors seem reasonable diagonal and comparable to YbOH, which was recently laser cooled. However, if BaOH can be efficiently laser cooled and/or if this is experimentally feasible cannot be said yet and is still an open question.

Acknowledgements

First, I would like to thank my supervisor Steven Hoekstra. Steven, you gave me a lot of freedom during my research, which I enjoyed, but you always had time to answer my questions and you always gave good suggestions in which direction to continue my project. Good luck in the search for the eEDM!

Rick Bethlem and Maarten Mooij, thank you for allowing me to do part of my master project at the VU in Amsterdam. It was very nice working with you both and I learned a lot about experimental physics (and proper Dutch scientific language).

I would also like to thank Anastasia Borschevsky for being my second examiner.

Ginny Marshall, thank you for teaching me about lasers during the summer. Leo Huisman, thank you for producing the $Ba(OH)_2$ targets.

Finally, I would like to thank Mark Buisman and Hidde Makaske for many discussions and for many afternoon table-tennis matches.

Appendix A

Franck-Condon Factors for BaOH

One of the most important benefits of these polyatomic molecules is that laser cooling can be combined with full polarization and internal co-magnetometer states. Laser cooling has not been treated in this thesis, but is vital in the consideration of BaOH for an eEDM experiment. Laser cooling requires scattering of many photons. Molecules can be lost to vibrational states. The probability for decay to vibrational states are given by the Franck-Condon factors. To be able to laser cool this molecule the Franck-Condon factors should be sufficiently diagonal, such that a large number of photons can be scattered with only a limited number of repump lasers.

Here we will give an approximation of the Frack-Condon factors for BaOH. The calculation will be done in the harmonic oscillator approximation. For a diatomic molecule such as BaF this calculation (using an harmonic approximation) would be relatively easy, since there is only one vibrational mode. In a triatomic molecule there are 4 modes. Here we will use the Sharp and Rosenstock matrix approach [88] for calculating for Franck-Condon factors. The exact same approach as [84][89] has been used. This method has been used for SrOH [84] and YbOH [13] to estimate Franck-Condon factors and showed good agreement with experimental observations [84] [90]. Both molecules have been laser cooled in 1D [15] [14].

The input parameters for the calculation of the Franck-Condon factors are the vibrational frequencies and the equilibrium bond lengths for each of the electronic states. We will consider the $\tilde{X}$, $\tilde{A}$ and $\tilde{B}$ electronic states. Table A.1 gives the molecular constants used for each electronic state.

Figure A.1 shows the Franck-Condon factors for BaOH between $\tilde{A}$ state and $\tilde{X}$ state and figure A.2 shows the Franck-Condon factors for BaOH between $\tilde{B}$ state and $\tilde{X}$ state. These results give us an approximate idea for the Franck-Condon factors for BaOH. These results are somewhat consistent with a recent ab-initio study [91] which predicts more diagonal Franck-Condon factors. The results here are similar to the Franck-Condon factors of YbOH [13].

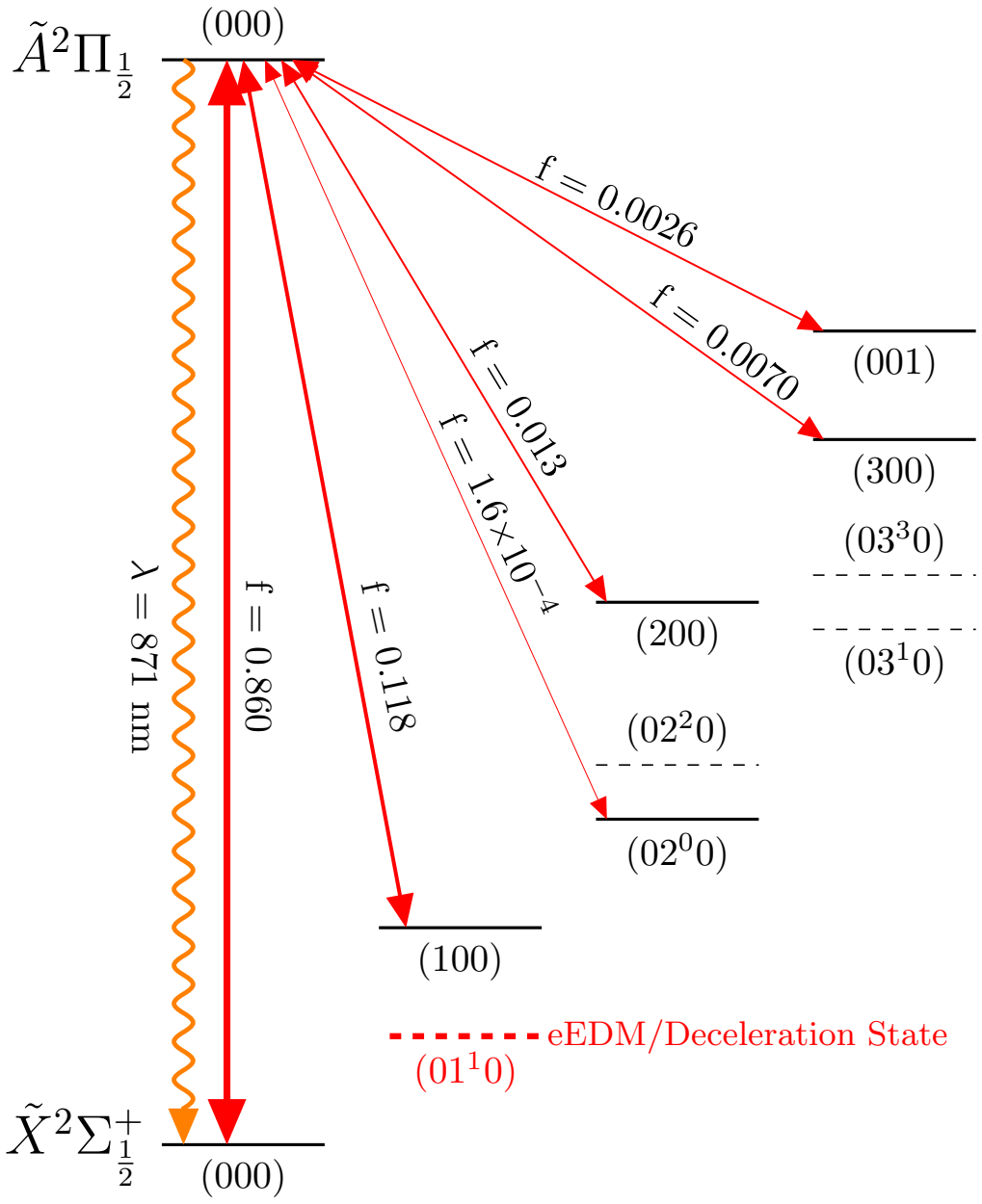

Figure A.1: Franck-Condon factors between electronic $\tilde{A}$ and $\tilde{X}$ state. In harmonic oscillator approximation.

	$\tilde{X}$	$\tilde{A}$	$\tilde{B}$
ω_1	492.4 cm^{-1}[43]	461.3 cm^{-1}[43]	458 cm^{-1}[34]
ω_2	341.6 cm^{-1}[43]	352 cm^{-1}[43]	352 cm^{-1}
ω_3	3888.1 cm^{-1}[45]	3888.1 cm^{-1}[45]	3888.1 cm^{-1}[45]
r_{e-Ba-O}	2.200 $\dot{A}$ [26]	2.237$\dot{A}$[41]	2.231 $\dot{A}$[34]
r_{e-O-H}	0.927 $\dot{A}$[26]	0.927 $\dot{A}$	0.923 $\dot{A}$ [34]

Table A.1: Molecular constants used in Franck-Condon calculation. ω_i are the vibrational constants. ω_1 denotes the Ba-O stretching mode, ω_2 denotes the bending mode and ω_3 denotes the he O-H stretching mode. r_e are the equilibrium bond lengths. The bending vibration of the $\tilde{B}$ is taken to be the same as the $\tilde{A}$ state. Bond length r_{e-O-H} of the $\tilde{A}$ state is taken to be the same as the $\tilde{X}$ state. Small variation of these parameter does not change the Franck-Condon factors much.

Interestingly, the $\tilde{B}$ state seems more diagonal than the $\tilde{A}$ state, which is not the case for BaF [77]. This would make it possible to laser cool on one of these transitions and use the other transition to pump the molecules back to increase the scattering rate [13]. In principle decays with $\Delta l \neq 0$ are forbidden in the Born-Oppenheimer approximation [29]. However, these decays can become allowed and have been observed for BaOH [34]. This can lead to additional loss channels, which will need to be addressed.

Since these Franck-Condon factors are comparable to YbOH, which has been Sisyphus laser cooled in 1D, this indicates that this might be possible for BaOH. However, just as in BaF there is also a lower lying $\tilde{A}'\Delta$ state [43] with a complicated vibrational structure [44], which can cause additional losses during laser cooling.

In [9] it is stated that decays to the $A'\Delta$ state from the $A\Pi$ state are suppressed, because of the small energy splitting of approximately 900cm$^-$1 [77]. Note that this energy splitting between the $\tilde{A}\Pi$ and $\tilde{A}'\Delta$ in BaOH is smaller, this splitting is approximately 450cm^{-1} [44].

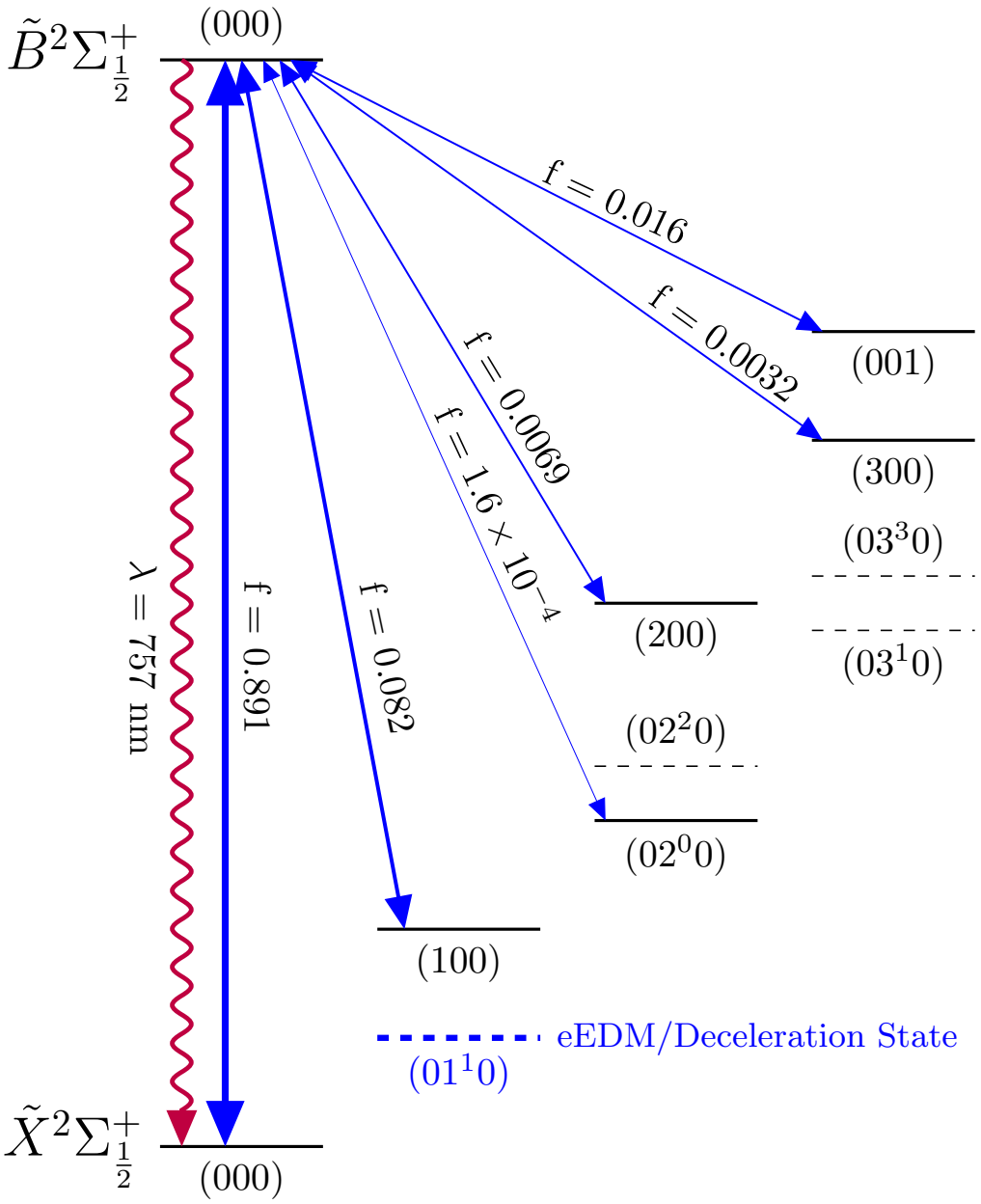

Figure A.2: Franck-Condon factors between electronic $\tilde{B}$ and $\tilde{X}$ state. In harmonic oscillator approximation.

Appendix B

Stark Effect for SrOH and YbOH and Zeeman Effect for BaOH

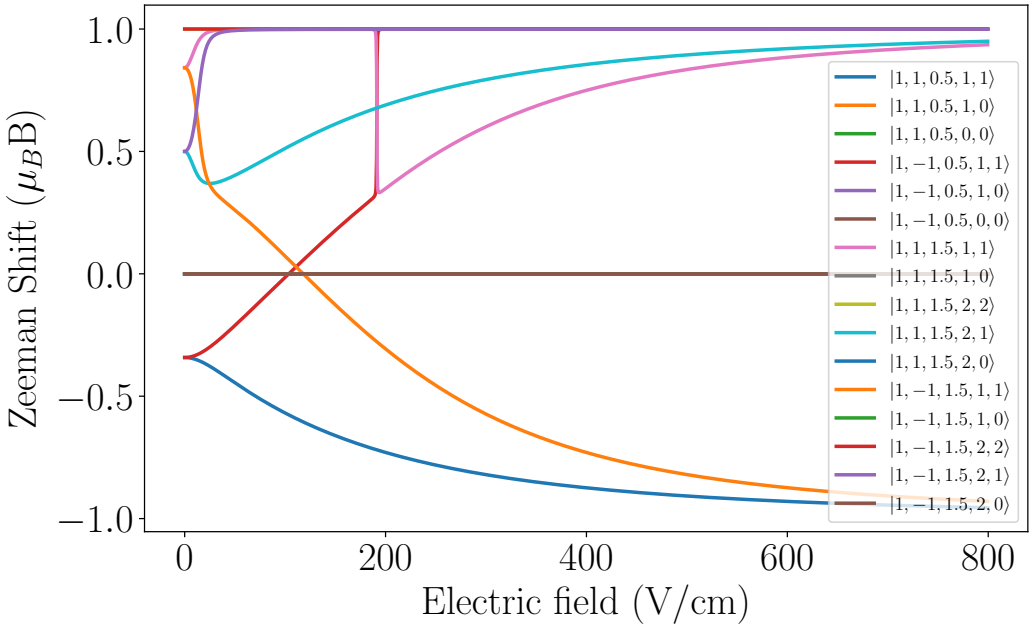

Figure B.1: Zeeman effect energy shift of BaOH in the first excited bending vibration as a function of electric field. The approach from [13] has been used: The expectation value of the Zeeman operator is calculated at every electric field point.

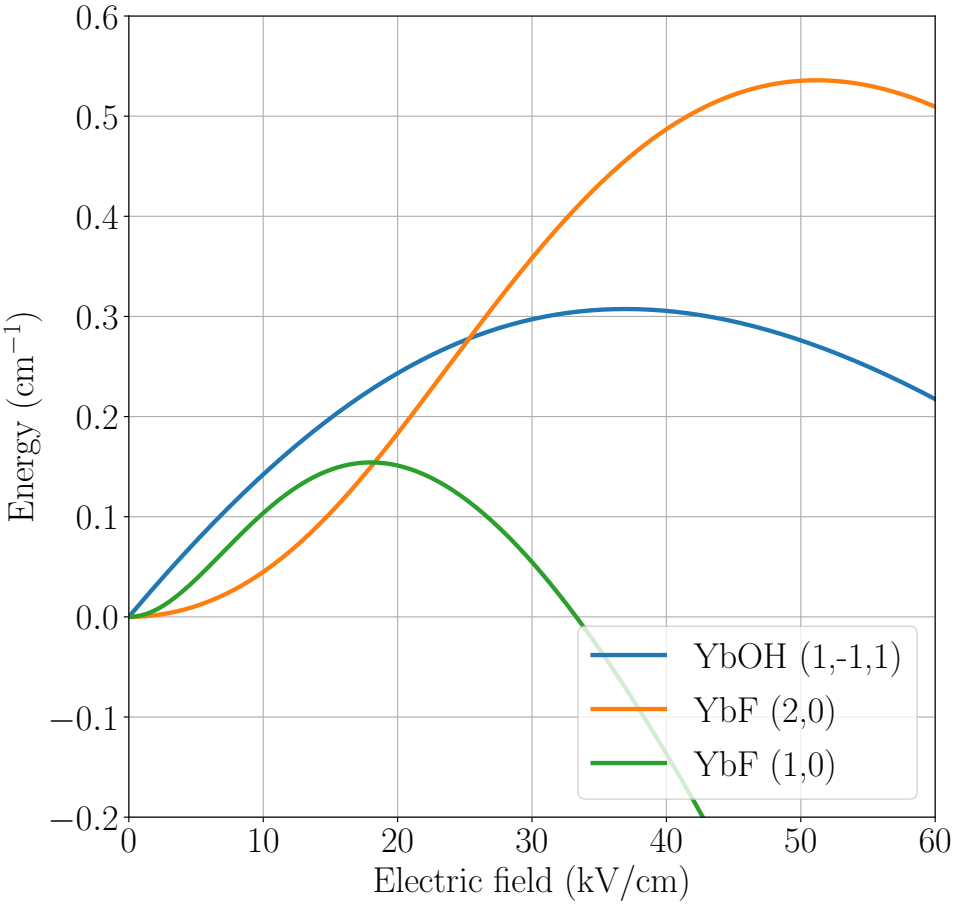

Figure B.2: Comparison of the Stark effect of YbF in the electronic and vibrational ground state and YbOH in the bending mode

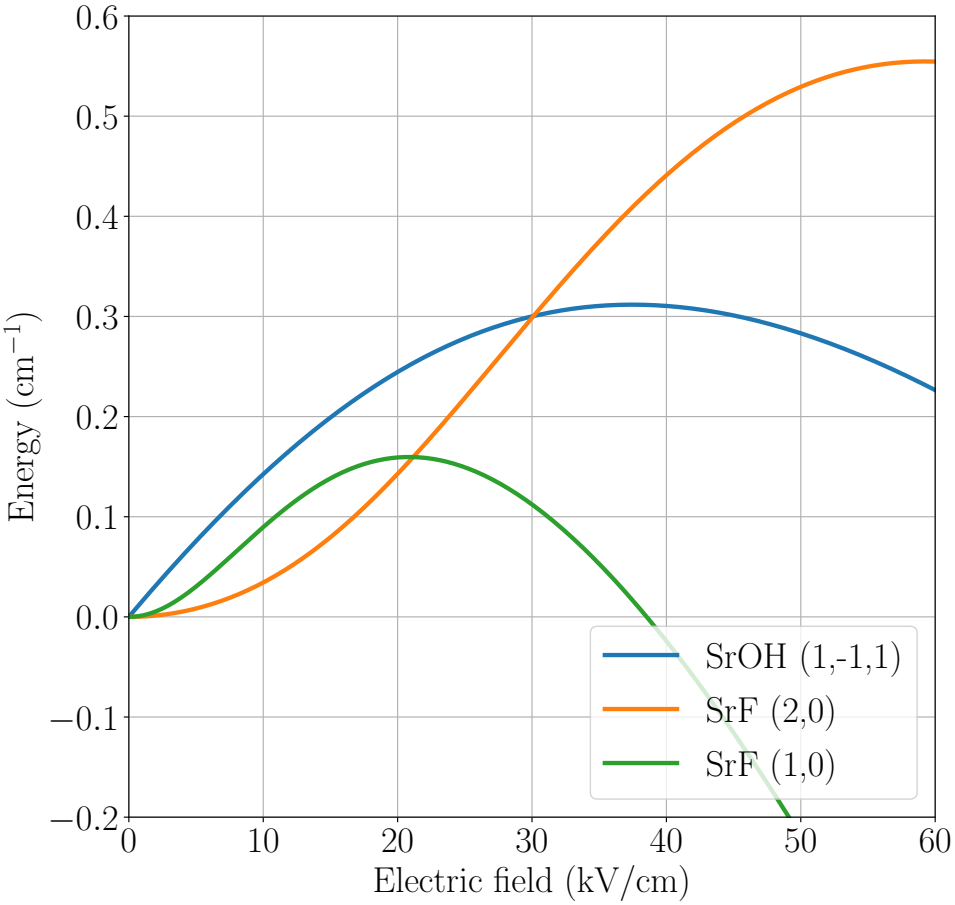

Figure B.3: Comparison of the Stark effect of SrF in the electronic and vibrational ground state and SrOH in the bending mode.

Appendix C

Traveling-Wave Stark Deceleration of BaF, YbOH, SrOH for Different Voltage Amplitudes

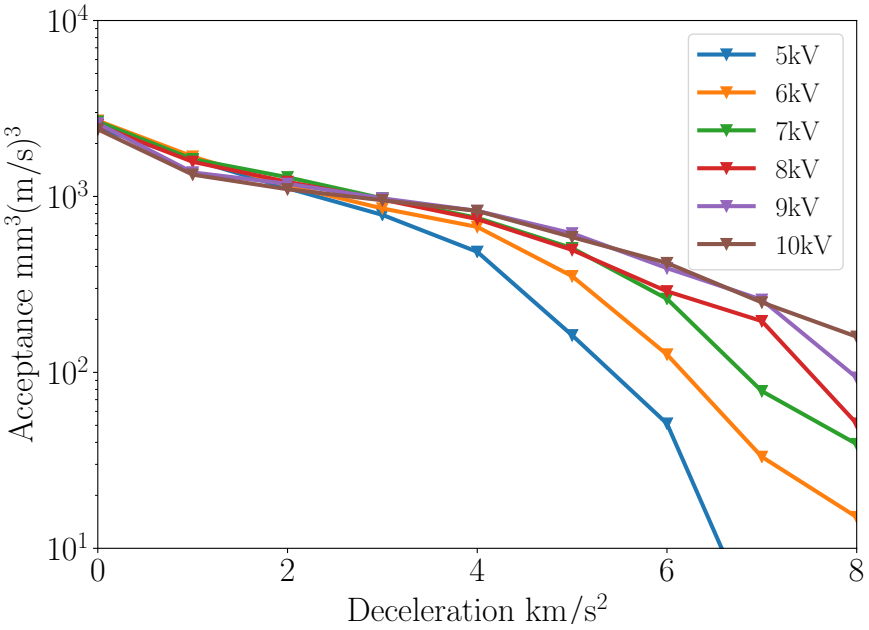

Figure C.1: YbOH 3D phase-space acceptance as a function of deceleration for different voltage amplitudes.

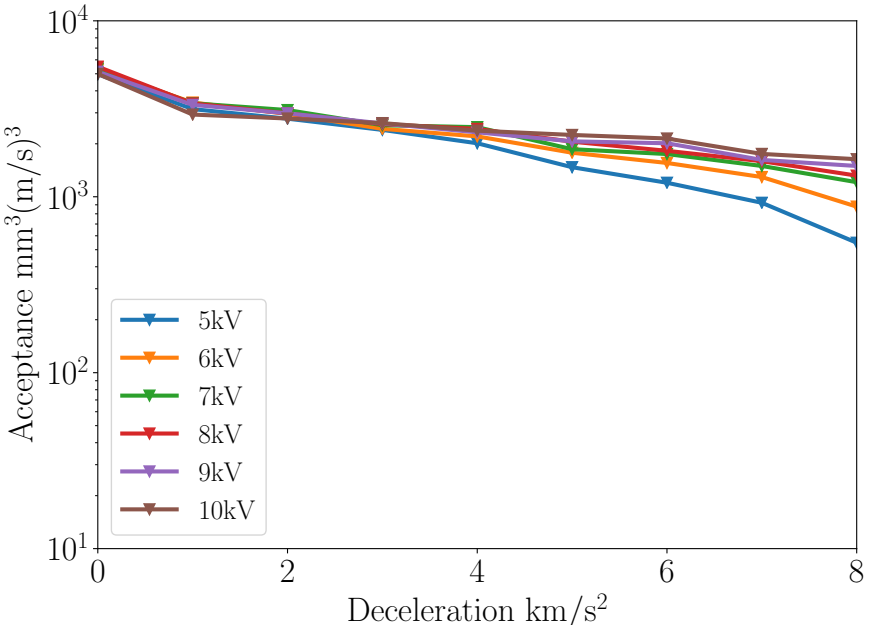

Figure C.2: SrOH 3D phase-space acceptance as a function of deceleration for different voltage amplitudes.

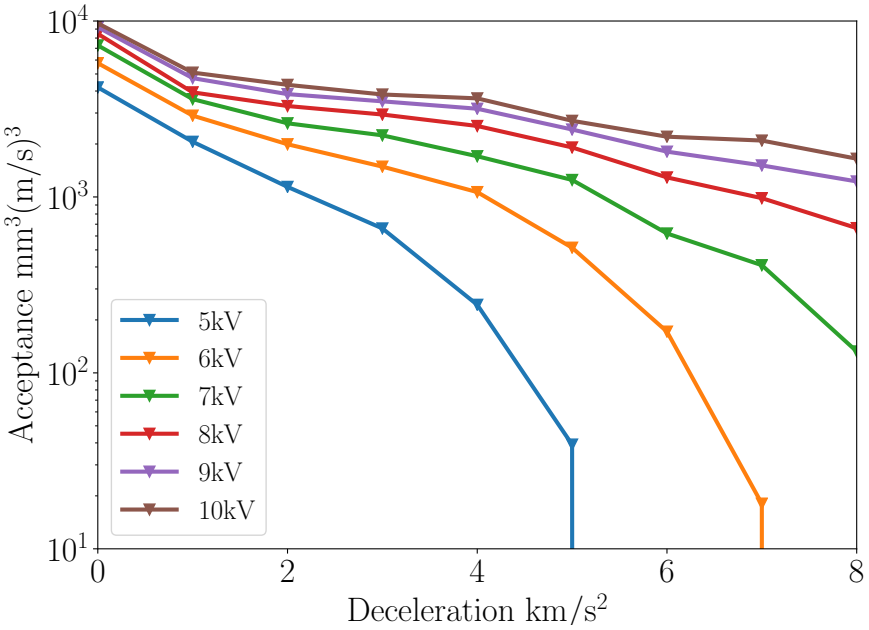

Figure C.3: BaF $|2,0\rangle$ 3D phase-space acceptance as a function of deceleration for different voltage amplitudes.

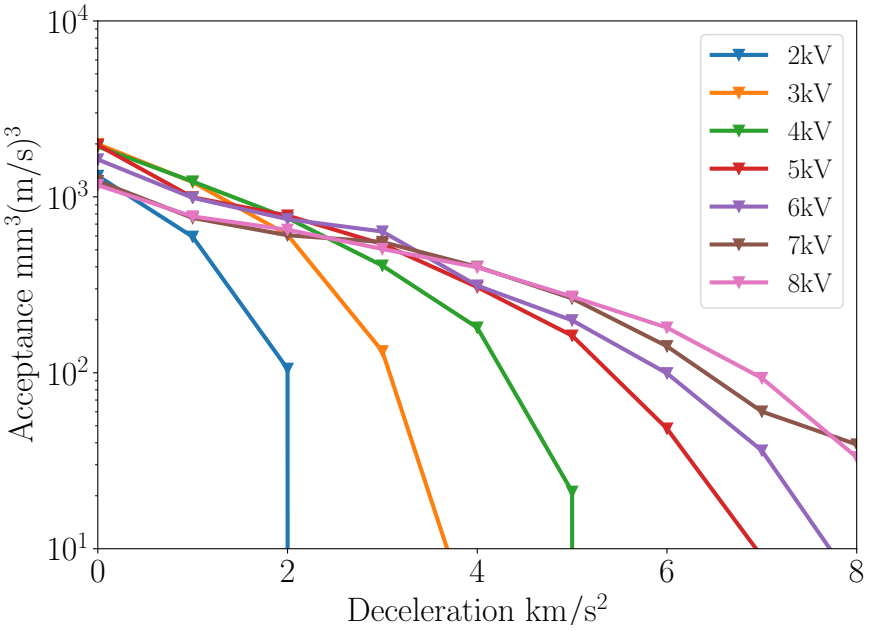

Figure C.4: BaF $|1,0\rangle$ 3D phase-space acceptance as a function of deceleration for different voltage amplitudes.

Bibliography

[1] E. S. Shuman, J. F. Barry, and D. Demille. Laser cooling of a diatomic molecule. *Nature*, 467(7317):820–823, 2010.

[2] Hendrick L. Bethlem, Giel Berden, and Gerard Meijer. Decelerating Neutral Dipolar Molecules. *Phys. Rev. Lett.*, 83:1558–1561, Aug 1999.

[3] D. DeMille. Quantum Computation with Trapped Polar Molecules. *Phys. Rev. Lett.*, 88:067901, Jan 2002.

[4] NL-eEDM website. https://www.rug.nl/research/vsi/newtopics/eedm.

[5] P. G. H. Sandars. Measurability of the Proton Electric Dipole Moment. *Phys. Rev. Lett.*, 19:1396–1398, Dec 1967.

[6] B. Lee Roberts, (Firm) World Scientific, and William J. Marciano. *Lepton Dipole Moments*. Number v. 20 in Advanced Series on Directions in High Energy Physics. World Scientific, 2010.

[7] ACME Colaboration. Improved limit on the electric dipole moment of the electron. *Nature*, 562(7727):355–360, 2018.

[8] J. J. Hudson, D. M. Kara, I. J. Smallman, B. E. Sauer, M. R. Tarbutt, and E. A. Hinds. Improved measurement of the shape of the electron. *Nature*, 473(7348):493–496, 2011.

[9] Parul Aggarwal, Hendrick Bethlem, Anastasia Borschevsky, Malika Denis, Kevin Esajas, Pi Haase, Yongliang Hao, Steven Hoekstra, Klaus Jungmann, Thomas Meijknecht, Maarten Mooij, Rob Timmermans, Wim Ubachs, Lorenz Willmann, and Artem Zapara. Measuring the electric dipole moment of the electron in BaF. *The European Physical Journal D*, 72, 11 2018.

[10] William B. Cairncross, Daniel N. Gresh, Matt Grau, Kevin C. Cossel, Tanya S. Roussy, Yiqi Ni, Yan Zhou, Jun Ye, and Eric A. Cornell. Precision Measurement of the Electron's Electric Dipole Moment Using Trapped Molecular Ions. *Phys. Rev. Lett.*, 119:153001, Oct 2017.

[11] Mohit Verma, Andrew M. Jayich, and Amar C. Vutha. Electric dipole moment searches using polar molecule clock states, 2019.

[12] D M Kara, I J Smallman, J J Hudson, B E Sauer, M R Tarbutt, and E A Hinds. Measurement of the electron's electric dipole moment using YbF molecules: methods and data analysis. *New Journal of Physics*, 14(10):103051, oct 2012.

[13] Ivan Kozyryev and Nicholas R. Hutzler. Precision Measurement of Time-Reversal Symmetry Violation with Laser-Cooled Polyatomic Molecules. *Phys. Rev. Lett.*, 119(13):133002, 2017.

[14] Benjamin L. Augenbraun, Zack D. Lasner, Alexander Frenett, Hiromitsu Sawaoka, Calder Miller, Timothy C. Steimle, and John M. Doyle. Laser-cooled polyatomic molecules for improved electron electric dipole moment searches, 2019.

[15] Ivan Kozyryev, Louis Baum, Kyle Matsuda, Benjamin L. Augenbraun, Loic Anderegg, Alexander P. Sedlack, and John M. Doyle. Sisyphus Laser Cooling of a Polyatomic Molecule. *Phys. Rev. Lett.*, 118:173201, Apr 2017.

[16] Louis Baum, Nathaniel B. Vilas, Christian Hallas, Benjamin L. Augenbraun, Shivam Raval, Debayan Mitra, and John M. Doyle. 1d magneto-optical trap of polyatomic molecules, 2020.

[17] Benjamin L. Augenbraun, John M. Doyle, Tanya Zelevinsky, and Ivan Kozyryev. Molecular asymmetry and optical cycling: Laser cooling asymmetric top molecules, 2020.

[18] Phelan Yu, Lawrence W Cheuk, Ivan Kozyryev, and John M Doyle. A scalable quantum computing platform using symmetric-top molecules. *New Journal of Physics*, 21(9):093049, sep 2019.

[19] Lucie D Augustovičová and John L Bohn. Ultracold collisions of polyatomic molecules: CaOH. *New Journal of Physics*, 21(10):103022, oct 2019.

[20] Malika Denis, Pi A. B. Haase, Rob G. E. Timmermans, Ephraim Eliav, Nicholas R. Hutzler, and Anastasia Borschevsky. Enhancement factor for the electric dipole moment of the electron in the BaOH and YbOH molecules. *Phys. Rev. A*, 99:042512, Apr 2019.

[21] V. S. Prasannaa, N. Shitara, A. Sakurai, M. Abe, and B. P. Das. Enhanced sensitivity of the electron electric dipole moment from YbOH: The role of theory. *Phys. Rev. A*, 99:062502, Jun 2019.

[22] W. Demtroder. *Molecular physics: an introduction to theoretical principles and experimental methods*. Wiley-VCH, 2005.

[23] Peter W. Atkins and Julio De Paula. *Physical chemistry*. Freeman, 2010.

[24] Peter F. Bernath. *Spectra of atoms and molecules*. Oxford University Press, 2005.

[25] David W. Ball and Tomas Baer. *Physical chemistry*. Wadsworth Cengage Learning, 2015. page number 507, chapter 14.12.

[26] M.A. Anderson, M.D. Allen, W.L. Barcaly, and L.M. Ziurys. The millimeter and sub-millimeter spectrum of the BaOH radical. *Chemical Physics Letters*, 205(4):415 – 422, 1993.

[27] G. Herzberg. l-Type Doubling in Linear Polyatomic Molecules. *Rev. Mod. Phys.*, 14:219–223, Apr 1942.

[28] Harald H. Nielsen and Wave H. Shaffer. A Note Concerning l-Type Doubling in Linear Polyatomic Molecules. *The Journal of Chemical Physics*, 11(3):140–144, 1943.

[29] Gerhard Herzberg. *Electronic spectra and electronic structure of polyatomic molecules*. Krieger Publishing Company, 1991.

[30] Paul I. Presunka and John A. Coxon. Laser spectroscopy of the $\tilde{A}^2\Pi - \tilde{X}^2\Sigma^+$ transition of SrOH: Deperturbation analysis of K-resonance in the v2=1 level of the $\tilde{A}^2\Pi$ state. *The Journal of Chemical Physics*, 101(1):201–222, 1994.

[31] Jon T. Hougen. Rotational Energy Levels of a Linear Triatomic Molecule in a $^2\pi$ Electronic State. *The Journal of Chemical Physics*, 36(2):519–534, 1962.

[32] E. Riedle. E. Hirota: High-Resolution Spectroscopy of Transient Molecules, Springer-Verlag, Berlin, Heidelberg, New York, Tokyo 1985. 233 Seiten, Preis: DM 125,—. *Berichte der Bunsengesellschaft für physikalische Chemie*, 90(11):1099–1099, 1986.

[33] Mingguang Li and John A. Coxon. High-resolution analysis of the fundamental bending vibrations in the $\tilde{A}^2\Pi$ and $\tilde{X}^2\Sigma^+$ states of CaOH and CaOD: Deperturbation of Renner–Teller, spin–orbit and K-type resonance interactions. *The Journal of Chemical Physics*, 102(7):2663–2674, 1995.

[34] S. Kinsey-Nielsen, C. R. Brazier, and P. F. Bernath. Rotational analysis of the $\tilde{B}^2\Sigma^+ - \tilde{X}^2\Sigma^+$ transition of BaOH and BaOD. *The Journal of Chemical Physics*, 84(2):698–708, 1986.

[35] David J. Griffiths and Darrell F. Schroeter. *Introduction to quantum mechanics*. Cambridge University Press, 2018.

[36] Roman V. Krems. *Molecules in electromagnetic fields: from ultracold physics to controlled chemistry*. Wiley, 2019.

[37] Nicholas Richard Hutzler. *A New Limit on the Electron Electric Dipole Moment: Beam Production, Data Interpretation, and Systematics*. PhD thesis, Harvard U., Phys. Dept., 2014.

[38] Samuel A. Meek, Maxwell F. Parsons, Georg Heyne, Viktor Platschkowski, Henrik Haak, Gerard Meijer, and Andreas Osterwalder. A traveling wave decelerator for neutral polar molecules. *Review of Scientific Instruments*, 82(9):093108, 2011.

[39] Joost Elbert van den Berg. *Traveling-wave Stark deceleration of SrF molecules*. PhD thesis, University of Groningen, 2015.

[40] D. A. Fletcher, M. A. Anderson, W. L. Barclay, and L. M. Ziurys. Millimeter-wave spectroscopy of vibrationally excited ground state alkaline-earth hydroxide radicals. *The Journal of Chemical Physics*, 102(11):4334–4339, 1995.

[41] J.D. Tandy, J.-G. Wang, and P.F. Bernath. High-resolution laser spectroscopy of BaOH and BaOD: Anomalous spin-orbit coupling in the $\tilde{A}^2\Pi$ state. *Journal of Molecular Spectroscopy*, 255(1):63 – 67, 2009.

[42] Sarah E. Frey and Timothy C. Steimle. Optical Stark spectroscopy of the $\tilde{A}\Pi(0,0,0)$-$\tilde{X}^2\Sigma^+(0,0,0)$ system of barium monohydroxide, BaOH. *Chemical Physics Letters*, 512(1):21 – 24, 2011.

[43] W.T.M.L Fernando, M Douay, and P.F Bernath. Vibrational analysis of the $\tilde{A}^2\Pi - \tilde{X}^2\Sigma^+$ and $\tilde{A}^2\Delta - \tilde{X}^2\Sigma^+$ transitions of BaOH and BaOD. *Journal of Molecular Spectroscopy*, 144(2):344 – 351, 1990.

[44] J.D. Tandy, J.-G. Wang, J. Liévin, and P.F. Bernath. Investigating the electronic states of BaOH by V-type double resonance spectroscopy and ab initio calculations: Further evidence of perturbation from the $\tilde{A}\Delta$ state. *Journal of Molecular Spectroscopy*, 270(1):44 – 50, 2011.

[45] Maximiliano Rossa, Iván Cabanillas-Vidosa, Gustavo A. Pino, and Juan C. Ferrero. New determination of the adiabatic ionization potential of the BaOH radical from laser photoionization-molecular beam experiments and ab initio calculations. *The Journal of Chemical Physics*, 136(6):064303, 2012.

[46] S.J. Pooley, M.S. Beardah, and A.M. Ellis. Electronic spectroscopy of the $\tilde{C} - \tilde{X}$ and $\tilde{D} - \tilde{X}$ transitions of BaOH1Dedicated to Professor Neville Jonathan to mark his retirement1. *Journal of Electron Spectroscopy and Related Phenomena*, 97(1):77 – 88, 1998.

[47] T Gustavsson, C Alcaraz, J Berlande, J Cuvellier, J.-M Mestdagh, P Meynadier, P de Pujo, O Sublemontier, and J.-P Visticot. On the perturbations in the (000-000) band of the BaOH $\tilde{B}^2\Sigma^+ - \tilde{X}^2\Sigma^+$ transition. *Journal of Molecular Spectroscopy*, 145(1):210 – 221, 1991.

[48] J.-G. Wang, J.D. Tandy, and P.F. Bernath. High-resolution laser excitation spectroscopy of the$\tilde{A}\Pi(000)$-$\tilde{X}\Sigma^+(000)$ transition of BaOH. *Journal of Molecular Spectroscopy*, 252(1):31 – 36, 2008.

[49] Yuan-Pin Chang, Frank Filsinger, Boris G. Sartakov, and Jochen Küpper. CMIstark: Python package for the Stark-effect calculation and symmetry classification of linear, symmetric and asymmetric top wavefunctions in dc electric fields. *Computer Physics Communications*, 185(1):339 – 349, 2014.

[50] Colin M. Western. PGOPHER: A program for simulating rotational, vibrational and electronic spectra. *Journal of Quantitative Spectroscopy and Radiative Transfer*, 186:221 – 242, 2017. Satellite Remote Sensing and Spectroscopy: Joint ACE-Odin Meeting, October 2015.

[51] A C Vutha, W C Campbell, Y V Gurevich, N R Hutzler, M Parsons, D Patterson, E Petrik, B Spaun, J M Doyle, G Gabrielse, and D DeMille. Search for the electric dipole moment of the electron with thorium monoxide. *Journal of Physics B: Atomic, Molecular and Optical Physics*, 44(7):079803, mar 2011.

[52] S. Bickman, P. Hamilton, Y. Jiang, and D. DeMille. Preparation and detection of states with simultaneous spin alignment and selectable molecular orientation in pbo. *Phys. Rev. A*, 80:023418, Aug 2009.

[53] William B. Cairncross, Daniel N. Gresh, Matt Grau, Kevin C. Cossel, Tanya S. Roussy, Yiqi Ni, Yan Zhou, Jun Ye, and Eric A. Cornell. Precision measurement of the electron's electric dipole moment using trapped molecular ions. *Phys. Rev. Lett.*, 119:153001, Oct 2017.

[54] Jonathan James Hudson. *Measuring the electric dipole moment of the electron with YbF molecules*. PhD thesis, University of Sussex, 2001.

[55] Artem Zapara. *Dynamics of molecular beams in a traveling-wave Stark decelerator*. PhD thesis, University of Groningen, 2019.

[56] Samuel A. Meek, Gabriele Santambrogio, Boris G. Sartakov, Horst Conrad, and Gerard Meijer. Suppression of nonadiabatic losses of molecules from chip-based microtraps. *Phys. Rev. A*, 83:033413, Mar 2011.

[57] Moritz Kirste, Boris G. Sartakov, Melanie Schnell, and Gerard Meijer. Nonadiabatic transitions in electrostatically trapped ammonia molecules. *Phys. Rev. A*, 79:051401, May 2009.

[58] T. E. Wall, S. K. Tokunaga, E. A. Hinds, and M. R. Tarbutt. Nonadiabatic transitions in a Stark decelerator. *Phys. Rev. A*, 81:033414, Mar 2010.

[59] Jeroen Muller. Electric fields and molecule motion in a traveling-wave Stark decelerator(Bachelor's Thesis, University of Groningen, 2017).

[60] Mark Buisman. Non-adiabatic losses in a traveling-wave Stark decelerator(Bachelor's Thesis, University of Groningen, 2017).

[61] Arthur G. Maki. Microwave spectra of molecules of astrophysical interest vi. carbonyl sulfide and hydrogen cyanide. *Journal of Physical and Chemical Reference Data*, 3(1):221–244, 1974.

[62] J.E. van den Berg, S.C. Mathavan, C. Meinema, J. Nauta, T.H. Nijbroek, K. Jungmann, H.L. Bethlem, and S. Hoekstra. Traveling-wave deceleration of SrF molecules. *Journal of Molecular Spectroscopy*, 300:22 – 25, 2014. Spectroscopic Tests of Fundamental Physics.

[63] N. E. Bulleid, R. J. Hendricks, E. A. Hinds, Samuel A. Meek, Gerard Meijer, Andreas Osterwalder, and M. R. Tarbutt. Traveling-wave deceleration of heavy polar molecules in low-field-seeking states. *Phys. Rev. A*, 86:021404, Aug 2012.

[64] Timothy C. Steimle, Colan Linton, Ephriem Tadesse Mengesha, Xilin Bai, and Anh T. Le. Field-free, Stark, and Zeeman spectroscopy of the $\tilde{A}\ ^2\Pi_{1/2} - \tilde{X}\ ^2\Sigma^+$ transition of ytterbium monohydroxide. *Phys. Rev. A*, 100:052509, Nov 2019.

[65] T. C. Steimle, D. A. Fletcher, K. Y. Jung, and C. T. Scurlock. A supersonic molecular beam optical Stark study of CaOH and SrOH. *The Journal of Chemical Physics*, 96(4):2556–2564, 1992.

[66] Nicholas R. Hutzler, Hsin-I Lu, and John M. Doyle. The Buffer Gas Beam: An Intense, Cold, and Slow Source for Atoms and Molecules. *Chemical Reviews*, 112(9):4803–4827, Sep 2012.

[67] S. Truppe, M. Hambach, S. M. Skoff, N. E. Bulleid, J. S. Bumby, R. J. Hendricks, E. A. Hinds, B. E. Sauer, and M. R. Tarbutt. A buffer gas beam source for short, intense and slow molecular pulses. *Journal of Modern Optics*, 65(5-6):648–656, 2018.

[68] Sanjay Nakhate, Timothy C. Steimle, Nickolas H. Pilgram, and Nicholas R. Hutzler. The pure rotational spectrum of YbOH. *Chemical Physics Letters*, 715:105 – 108, 2019.

[69] Ivan Kozyryev, Timothy C Steimle, Phelan Yu, Duc-Trung Nguyen, and John M Doyle. Determination of CaOH and CaOCH3 vibrational branching ratios for direct laser cooling and trapping. *New Journal of Physics*, 21(5):052002, may 2019.

[70] Arian Jadbabaie, Nickolas H. Pilgram, Jacek Klos, Svetlana Kotochigova, and Nicholas R. Hutzler. Enhanced Yield from a Cryogenic Buffer Gas Beam Source via Excited State Chemistry, 2019.

[71] Paul Hofland. Towards absorption spectroscopy on a buffer gas cooled beam of BaF molecules(Master Thesis, UvA, 2019).

[72] Timothy C. Steimle, Sarah Frey, Anh Le, David DeMille, David. A. Rahmlow, and Colan Linton. Molecular-beam optical Stark and Zeeman study of the $A\ ^2\Pi$–$X\ ^2\Sigma^+$ (0,0) band system of BaF. *Phys. Rev. A*, 84:012508, Jul 2011.

[73] Ivan Kozyryev, Louis Baum, Kyle Matsuda, Peter Olson, Boerge Hemmerling, and John M Doyle. Collisional relaxation of vibrational states of SrOH with he at 2 k. *New Journal of Physics*, 17(4):045003, apr 2015.

[74] R.F. Barrow, A. Bernard, C. Effantin, J. D'Incan, G. Fabre, A. El Hachimi, R. Stringat, and J. Vergès. The metastable A' $^2\Delta$ state of BaF. *Chemical Physics Letters*, 147(6):535 – 537, 1988.

[75] J. F. Barry, E. S. Shuman, and D. DeMille. A bright, slow cryogenic molecular beam source for free radicals. *Phys. Chem.*, 13:18936–18947, 2011.

[76] David Rahmlow. *Towards a measurement of parity nonconservation in diatomic molecules*. PhD thesis, Yale University, 2010.

[77] Yongliang Hao, Lukáš F. Pašteka, Lucas Visscher, Parul Aggarwal, Hendrick L. Bethlem, Alexander Boeschoten, Anastasia Borschevsky, Malika Denis, Kevin Esajas, Steven Hoekstra, Klaus Jungmann, Virginia R. Marshall, Thomas B. Meijknecht, Maarten C. Mooij, Rob G. E. Timmermans, Anno Touwen, Wim Ubachs, Lorenz Willmann, Yanning Yin, and Artem Zapara. High accuracy theoretical investigations of CaF, SrF, and BaF and implications for laser-cooling. *The Journal of Chemical Physics*, 151(3):034302, 2019.

[78] P. Aggarwal, V. R. Marshall, H. L. Bethlem, A. Boeschoten, A. Borschevsky, M. Denis, K. Esajas, Y. Hao, S. Hoekstra, K. Jungmann, T. B. Meijknecht, M. C. Mooij, R. G. E. Timmermans, A. Touwen, W. Ubachs, S. M. Vermeulen, L. Willmann, Y. Yin, and A. Zapara. Lifetime measurements of the $A\ ^2\Pi_{1/2}$ and $A\ ^2\Pi_{3/2}$ states in BaF. *Phys. Rev. A*, 100:052503, Nov 2019.

[79] Christopher Foot. *Atomic physics*. Oxford Univ. Press, 2011.

[80] J. Brust and A. C. Gallagher. Excitation transfer in barium by collisions with noble gases. *Phys. Rev. A*, 52:2120–2131, Sep 1995.

[81] H. Floyd Davis, Arthur G. Suits, Yuan T. Lee, Christian Alcaraz, and Jean-Michel Mestdagh. State specific reactions of Ba(1S0) and Ba(1D2) with water and methanol. *The Journal of Chemical Physics*, 98(12):9595–9609, 1993.

[82] C. R. Brazier, L. C. Ellingboe, S. Kinsey-Nielsen, and P. F. Bernath. Laser spectroscopy of alkaline earth monoalkoxide free radicals. *Journal of the American Chemical Society*, 108(9):2126–2132, 1986. PMID: 22175549.

[83] R.F. Wormsbecher and R.D. Suenram. Laser spectroscopy and chemiluminescence from the monomethoxides of Ca, Sr, and Ba. *Journal of Molecular Spectroscopy*, 95(2):391 – 404, 1982.

[84] Ivan Kozyryev. *Laser Cooling and Inelastic Collisions of the Polyatomic Radical SrOH*. PhD thesis, Harvard University, 2017.

[85] N. D. Scielzo, J. R. Guest, E. C. Schulte, I. Ahmad, K. Bailey, D. L. Bowers, R. J. Holt, Z.-T. Lu, T. P. O'Connor, and D. H. Potterveld. Measurement of the lifetimes of the lowest $^3P_1$ state of neutral Ba and Ra. *Phys. Rev. A*, 73:010501, Jan 2006.

[86] U. Dammalapati, S. De, K. Jungmann, and L. Willmann. Isotope shifts of 6s5d^{3}D-6s6p^{1}P$_1$ transitions in neutral barium. *The European Physical Journal D*, 53(1):1–8, May 2009.

[87] E. Verdasco, V. Rabanos, and A. Ureña. Reaction Dynamics of Translational and Electronic Excitation In Ca + SF6 Collisions. *Laser Chemistry*, 10, 01 1989.

[88] T. E. Sharp and H. M. Rosenstock. Franck—Condon Factors for Polyatomic Molecules. *The Journal of Chemical Physics*, 41(11):3453–3463, 1964.

[89] M. D. Oberlander. *Laser Excited Fluorescence Studies of Reactions of Group 2 Metals with Oxygen Containing Molecules and of Heavy Group 15 Clusters with Fluorine: Reactivities, Product State Distributions and Spectroscopy of the Bismuth Monofluoride $A\Sigma^+ - X\Sigma^+$ Transition.* PhD thesis, THE OHIO STATE UNIVERSITY., 1995.

[90] Nguyen. *Optical Spectroscopy of Heavy Element Containing Molecules In Support of Fundamental Physics.* PhD thesis, Arizona State University.

[91] Maxim V. Ivanov, Felix H. Bangerter, and Anna I. Krylov. Towards a rational design of laser-coolable molecules: insights from equation-of-motion coupled-cluster calculations. *Physical Chemistry Chemical Physics*, 21(35):19447–19457, 2019.